

MEASUREMENT OF INCLUSIVE MUON PAIR PRODUCTION
BY 225-GEV/c π^+ , π^- , AND PROTON BEAMS
WITH A LARGE ACCEPTANCE SPECTROMETER

by

James G. Branson

A DISSERTATION
PRESENTED TO THE
FACULTY OF PRINCETON UNIVERSITY
IN CANDIDACY FOR THE DEGREE
OF DOCTOR OF PHILOSOPHY

RECOMMENDED FOR ACCEPTANCE BY THE
DEPARTMENT OF
PHYSICS

May, 1977

PLEASE NOTE:

This dissertation was printed
by computer and has very light
and indistinct print in places.
Best available copy. Filmed as
received.

UNIVERSITY MICROFILMS.

TABLE OF CONTENTS

	Page
ABSTRACT	1
CHAPTER I. INTRODUCTION	
A. The Discovery of New Particles	2
B. Continuum Muon Pairs	8
C. The Experiment	11
CHAPTER II. APPARATUS	
A. Overview	13
B. The Beam Line	15
C. Beam Cerenkov Counters	17
D. The Veto Counters	18
E. The Beam Defining Counters	19
F. The Interaction Counter T ₅	20
G. The Multiwire Proportional Chambers	21
H. The Spark Chambers	22
I. The Chicago Cyclotron Magnet	24
J. The P Hodoscope	25
K. The J Hodoscope	26
L. The Trigger and Fast Electronics	27
M. Data Aquisition	29
CHAPTER III. EVENT RECONSTRUCTION	
A. The Upstream Track Finder	31
B. Downstream Track Finder	32
C. The P Counter Requirement	34
D. Linking	35
E. Momentum Calculation	36
F. Reconstruction Efficiency	36
G. Data Handling	38

CHAPTER IV. ANALYSIS

A. χ^2 Fit to Upstream Slopes	40
B. Normalization and Beam Particle Identification	42
C. The J Trigger	47
D. Backgrounds	48
E. The Monte Carlo Program	49
F. Secondary Production	58

CHAPTER V. RESULTS

A. Mass, x_F and P Distributions	60
B. General Trends of the Data	63
C. J Production	64
D. Additional Muons in Association with the J	67
E. ψ' Production	71
F. The Drell-Yan Model	72

REFERENCES

ACKNOWLEDGEMENTS

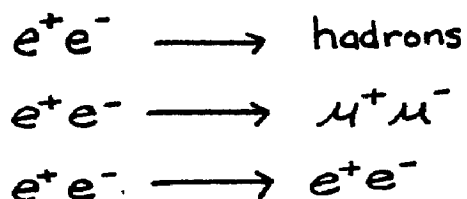
ABSTRACT

Inclusive muon pair production by 225 GeV/c π^+ , π^- and proton beams incident upon carbon and tin targets was measured over a large range of kinematic variables ($2m_\mu < m_{\mu\mu} < 10\text{GeV}/c^2$, $0 < x_\mu < 1$, $p_\perp < 4\text{ GeV}/c$ and $|\cos\theta^*| < .8$). The value of the invariant cross section $E \frac{d^4\sigma}{dm dx_\mu d^2p_\perp}$ is presented as a function of these variables. The vector mesons ρ , ω , ϕ , J and ψ' appear in the data along with apparently nonresonant μ -pairs. By looking for additional muons accompanying $J \rightarrow \mu^+\mu^-$ events, a 1.0 percent upper limit on production of pairs of charmed particles in association with the J is obtained. Aspects of the continuum muon pair data are compared to Drell-Yan model calculations. The ratio of μ -pairs produced by π^+ beam particles to μ -pairs produced by π^- beam particles supports electromagnetic production at high mass.

CHAPTER I. Introduction

A. The Discovery of New Particles

Late in 1974, the discovery of a narrow resonance of mass $3.1 \text{ GeV}/c^2$ was announced simultaneously by the MIT-BNL¹ collaboration working at the Brookhaven National Laboratory Alternating Gradient Synchrotron and by the SLAC-LBL collaboration² working at SPEAR, the electron positron colliding beams facility at the Stanford Linear Accelerator Center. The MIT-BNL group made the discovery by observing electron positron pairs in a two arm spectrometer using $30 \text{ GeV}/c^2$ protons incident on Be. They found a strong peak at $3.1 \text{ GeV}/c^2$ with a width consistent with zero. The SLAC-LBL group found a sharp peak in the cross sections



They observed a width less than or equal to $1.3 \text{ MeV}/c^2$. Each group gave a name to the new particle. The MIT-BNL group labeled it J while the SLAC-LBL group called it ψ .

Although opinions varied at the time as to what this new particle was, there was agreement that a massive particle which was so narrow meant that some kind of new physics was being discovered. A few months later, a

Fermilab experiment^{3,4} reported J production from photon and neutron interactions with Be. From the t (momentum transfer squared) distribution of the photon induced production, the authors concluded that the J was produced diffractively off the Be nucleus. The ratio of J signal to continuum in the neutron induced data, compared to that found at SPEAR, indicated that the J was produced via the strong interaction, supporting the conclusion that the J was a vector meson.

Even though the J had an unusually long lifetime, it fit in well with some theories of the weak interaction. Prior to its discovery, all known strongly interacting particles were thought to be composed of three types ("flavors") of spin $1/2$ point particles called "quarks" which were bound together by spin one particles called "gluons". The following table lists quark properties.

QUARK QUANTUM NUMBERS

Flavor	u	d	s	c
Spin	1/2	1/2	1/2	1/2
Charge	2/3	-1/3	-1/3	2/3
Baryon Number	1/3	1/3	1/3	1/3
Isospin	1/2	1/2	0	0
Strangeness	0	0	-1	0
Charm	0	0	0	1

In the usual model, quarks have an additional unbroken SU(3) degree of freedom called "color". Each of the flavors of quarks can come in any of three colors while the gluons form a color octet.

The existence of a fourth quark flavor was predicted by weak interaction gauge theories which were attractive because they offered a way to unify the weak and electromagnetic interactions. These theories had the problem that they predicted the existence of weak neutral currents, which had not been observed. Although neutral currents which did not change strangeness were later observed in neutrino scattering experiments, experimental upper limits on strangeness changing neutral currents were below the level predicted by the theories. These limits are

derived from measurements of $K_L \rightarrow \mu^+ \mu^-$ and from the $K_L - K_S$ mass difference.

An elegant way of suppressing strangeness changing neutral currents in the theory was to add the fourth quark flavor. This new quark was labeled c and carried a new quantum number called "charm". With this addition many massive long lived particles were predicted⁵, including particles that carry the charm quantum number as well as a family of $c\bar{c}$ mesons with a spectrum similar to that of positronium. The J is thought to be a $1^- c\bar{c}$ bound state. It is analogous to the ψ meson which is predominantly $s\bar{s}$ and for this reason the J is sometimes referred to as the ψ_c . Some of the charmed particles have now been found at SPEAR^{6,7} and at Fermilab⁸.

Assuming then that the J is a bound state of a charmed quark and a charmed antiquark, authors have proposed several production mechanisms. Siverson and Goldman^{9,10} examined production in the multiperipheral model and concluded that mechanisms of the type shown in figure 1-1b should account for about 80 percent of the J 's produced. The quark line diagram shown in the figure satisfies an empirical rule first proposed by Okubo¹¹, Zweig¹² and Iizuka¹³. In the Zweig-Iizuka formulation, the rule states that any disconnected quark line diagrams (figure 1-1a) are

PLEASE NOTE:

Thesis is tightly bound.
Some print lost in spine.
Filmed in the best
possible way.

UNIVERSITY MICROFILMS.

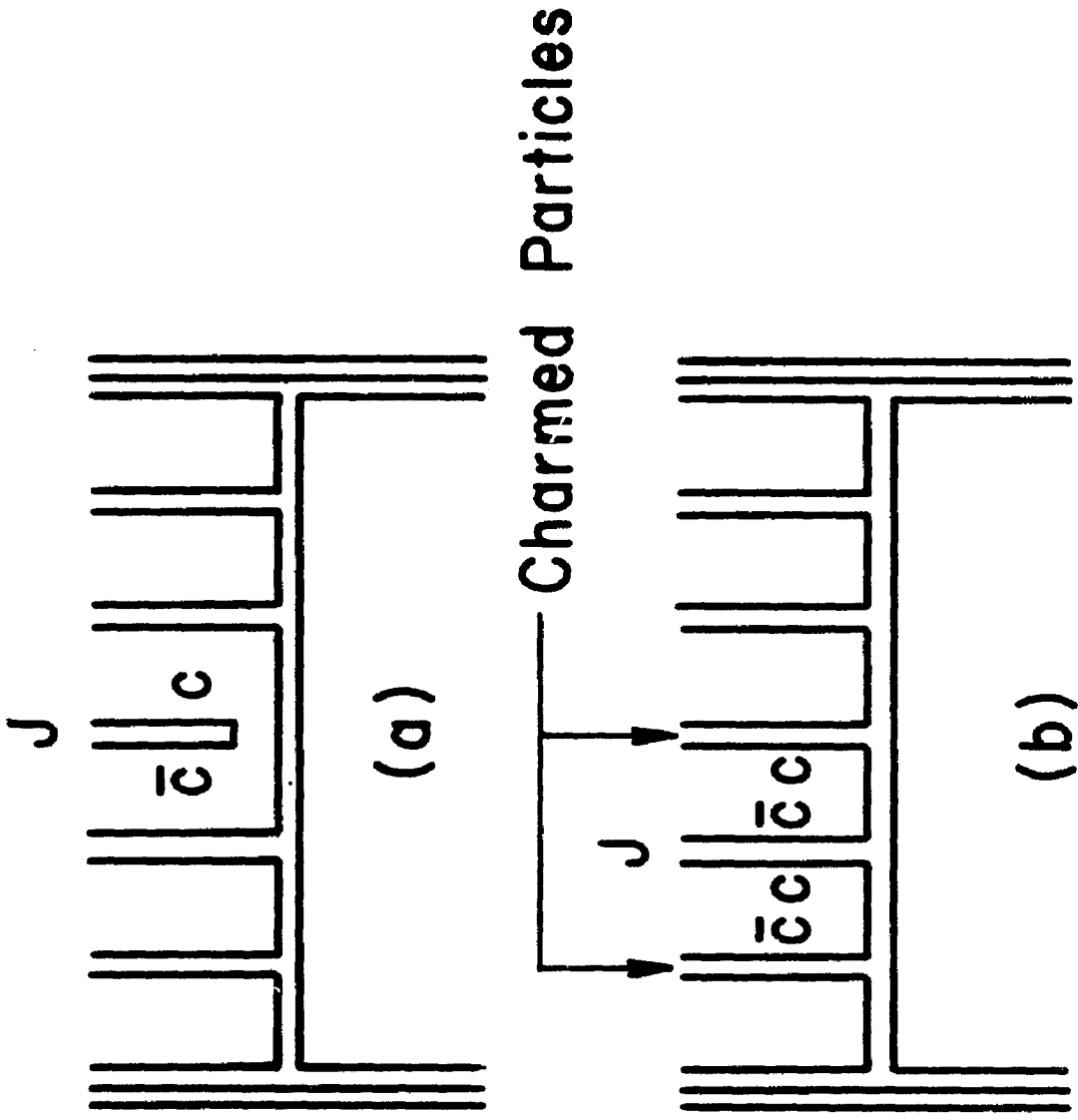


FIGURE 1-1, TWO QUARK-LINE DIAGRAMS FOR J PRODUCTION. (A) THIS DIAGRAM IS NOT ALLOWED BY THE OZI RULE BECAUSE THERE IS A DISCONNECTED QUARK-LINE. (B) THIS IS AN OZI ALLOWED DIAGRAM. A PAIR OF CHARMED PARTICLES IS PRODUCED IN ASSOCIATION WITH THE J ALLOWING ALL QUARK-LINES TO BE CONNECTED.

suppressed. The allowed mechanisms of J production then require a pair of charmed particles in association with it. OZI forbidden production of J's (figure 1-1a) and of higher mass charmonium states which decay to the J, were said to account for the other 20 percent. The OZI rule was originally introduced to account for the small cross sections for production of $s\bar{s}$ mesons and for their decay to nonstrange hadrons, $\psi \rightarrow \rho\pi$ and $f'(1514) \rightarrow \pi\pi$. It is also thought to play a large role in giving the J its narrow width¹⁴, suppressing J decay to hadrons by more than a factor of 1000. Although the OZI rule is vital in explaining the narrow width of the J, its basis in theory is not well understood. It is not universally agreed that the OZI rule implies that charmed particles should be produced in association with J's.

Einhorn and Ellis¹⁵ considered J production by several mechanisms. They claimed that quark-antiquark annihilation and release of charm-anticharm pairs from the sea in ordinary hadrons gave cross sections too small to account for the data. They also considered J production and η_c production by the gluons present in hadrons. Quantum number considerations require that the J can only be produced directly via a three gluon process (figure 1-2a); however, the even charge conjugation ($C = +1$) charmonium states can

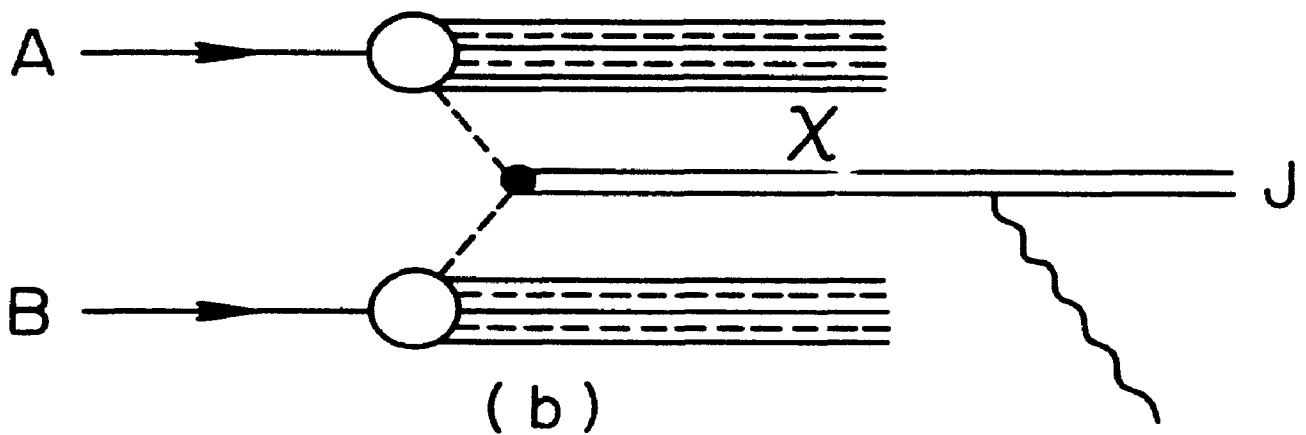
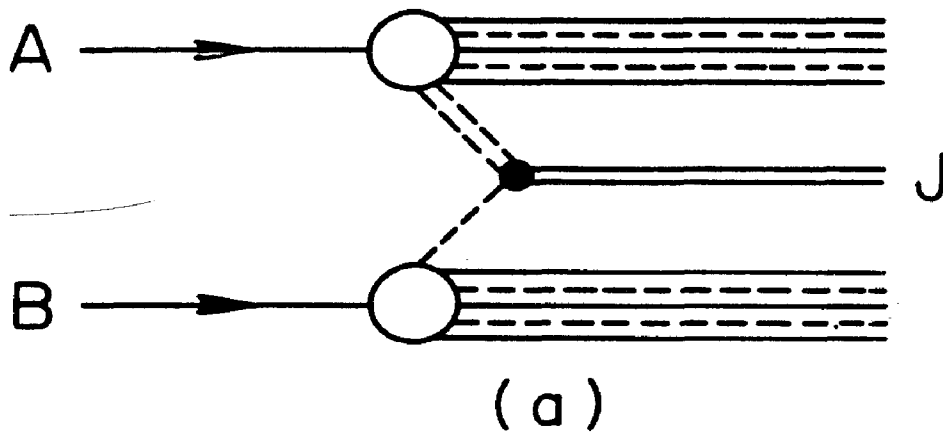


FIGURE 1-2. TWO DIAGRAMS OF J PRODUCTION BY GLUONS. (A) THE J IS PRODUCED DIRECTLY IN THIS DIAGRAM BY A THREE GLUON MECHANISM. (B) AN EVEN CHARGE CONJUGATION $C\bar{C}$ STATE (χ) IS PRODUCED BY TWO GLUONS IN THIS DIAGRAM. THE χ SUBSEQUENTLY DECAYS TO THE J BY EMITTING A PHOTON.

be produced by a two gluon method, shown in figure 1-2b, which is favored over the three gluon production. Carlson and Suaya¹⁶ proposed that the dominant mode of J production was two gluon production of the $C = +1$ states followed by photon emission to the J. Then assuming that the gluon x distribution is the same as that of the quarks, they were able to calculate (following the same line Einhorn and Ellis had used for the η_c) the total J production cross section as a function of s and also $d\sigma/dx_F$. Here x is the fraction of a particle's momentum that is carried by a given constituent parton and s is the total center of mass energy squared ($s = (p_1 + p_2)^2$). The scaling variable x_F is defined to be the momentum along the beam direction of an outgoing particle divided by the maximum possible momentum that particle could carry consistent with quantum number conservation ($x_F \approx 2p_{||}/\sqrt{s}$).

Soon after the discovery of the J, another large narrow resonance at $3.7 \text{ GeV}/c^2$ was found at SPEAR¹⁷ and was named ψ' . This is now understood to be a radial excitation of the $c\bar{c} 1^-$ bound state.

Production of the ψ' should be very similar to that of the J because it is a radial excitation. One major difference is that the states of even charge conjugation which can be produced by the two gluon process have masses

lower than that of the ψ' . Any that may lie above it are likely to have masses large enough to also lie above the threshold to decay strongly to two charmed particles. If this is the case, the branching ratio to the ψ' would be small.

B. Continuum Muon Pairs

To investigate the structure of hadrons as bound states of partons (quarks and gluons), it is useful to perform experiments in which the partons can be treated in the impulse approximation. Under this approximation a parton is thought of as instantaneously free during an interaction that transfers a large amount of energy to it from a projectile. This greatly simplifies the kinematics involved.

Examples of experiments that probe the parton nature of hadrons using the impulse approximation are: deep inelastic lepton scattering, electron-positron annihilation to hadrons, and massive lepton pair production in hadron-hadron collisions. Much information has been obtained about quark distributions in nucleons from deep inelastic lepton scattering. From e^+e^- annihilation, knowledge of the number of quark flavors and of the quark charges has been gained.

In 1970, Drell and Yan¹⁸ stated that production of nonresonant massive lepton pairs is dominated by

quark-antiquark annihilation into a timelike photon which then decays to the lepton pair. They found that the impulse approximation is valid for quarks with momenta much greater than 1 GeV/c in the center of mass of the collision. The Drell-Yan model has been discussed by many authors^{19,20,21} because it predicts a simple relation between massive lepton pair production cross sections and hadron structure functions.

$$\frac{d^2\sigma}{dQ^2 dx_F} = \frac{4\pi\alpha^2}{3Q^4} \left\{ \sum_i \frac{e_i^2}{x_A + x_B} \left[x_A f_L^A(x_A) x_B f_L^B(x_B) + x_A f_{\bar{L}}^A(x_A) x_B f_L^B(x_B) \right] \right\}$$

Here Q^2 is the 4-momentum transfer squared ($Q^2 = m^2 > 0$), the sum is over quark flavors, e_i is the quark charge, $x_A = \frac{1}{2} (x_F + \sqrt{x_F^2 + 4Q^2/s})$, $x_B = \frac{1}{2} (-x_F + \sqrt{x_F^2 + 4Q^2/s})$, and $f_i^A(x_A)$ is the probability of finding a quark of flavor i carrying a fraction x_A of the momentum of hadron A. The f 's are simply related to structure functions measured in electron and neutrino scattering from protons.

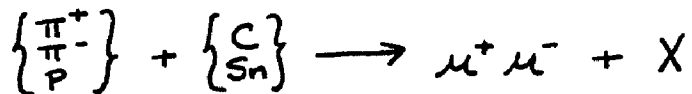
Dominance of the Drell-Yan mechanism in production of massive lepton pairs is a basic prediction of the quark model. Experiments measuring massive lepton pair production can test this model and, if it is correct, they can measure hadron structure functions where they have not yet been determined, for small x in the proton and for all x in

pions. One particularly good test of the Drell-Yan model is the measurement of the high mass lepton pair production cross section for π^+ incident on an isoscalar nuclear target compared to that for π^- . At large mass, the virtual quark-antiquark pairs within hadrons should make only a small contribution to lepton pair production. Then, in order to have quark-antiquark annihilation, the antiquark must come from the pion because there are no valence antiquarks in nucleons. Since the antiquark in the π^- (\bar{u}) has twice the charge of the antiquark in the π^+ (\bar{d}), the cross section for π^- induced lepton pairs should be four times that for π^+ . Because the target is isoscalar, π^- induced production via the strong interaction must be equal to π^+ induced production.

The earliest experiment to detect high mass lepton pairs was performed by Christenson²² et al. who measured muon pairs in the mass range 1.0 to 6.5 GeV/c². Because of poor resolution (about 11 percent at 3 GeV/c²), they believed the dimuons measured were nonresonant even though the J made a substantial contribution to the spectrum in the three GeV/c² region. Their results were larger than the predicted Drell-Yan production cross sections. This was probably due to unrecognized resonance production.

C. The Experiment

This thesis is based upon a large acceptance, high resolution experiment which measured inclusive muon pair production at $\sqrt{s} = 21 \text{ GeV}/c^2$ (over a large range of kinematic variables) by π^+ , π^- and protons incident on carbon and tin targets. Some results from a test run at $\sqrt{s} = 17 \text{ GeV}/c^2$ will also be reported.



The acceptance of the apparatus was large for

$$2m_\mu < m_{\mu\mu} < 12 \text{ GeV}/c^2$$

$$0 < x_F < 1$$

$$P_\perp < 4 \text{ GeV}/c$$

$$\text{and } |\cos \theta^*| < 0.8$$

where θ^* is defined in figure 1-3. This thesis will deal mainly with the μ -pairs with masses greater than about one GeV/c^2 . Using these data, J production, ψ' production and production of high mass non-resonant muon pairs can be studied. In addition, due to the large acceptance of the apparatus, "unusual" events with more than two muons can be observed. This is especially interesting in light of the prediction that the J 's should be produced in association with charmed particles.

The thesis of G. G. Henry (University of Chicago) is based upon the same experiment and will include important

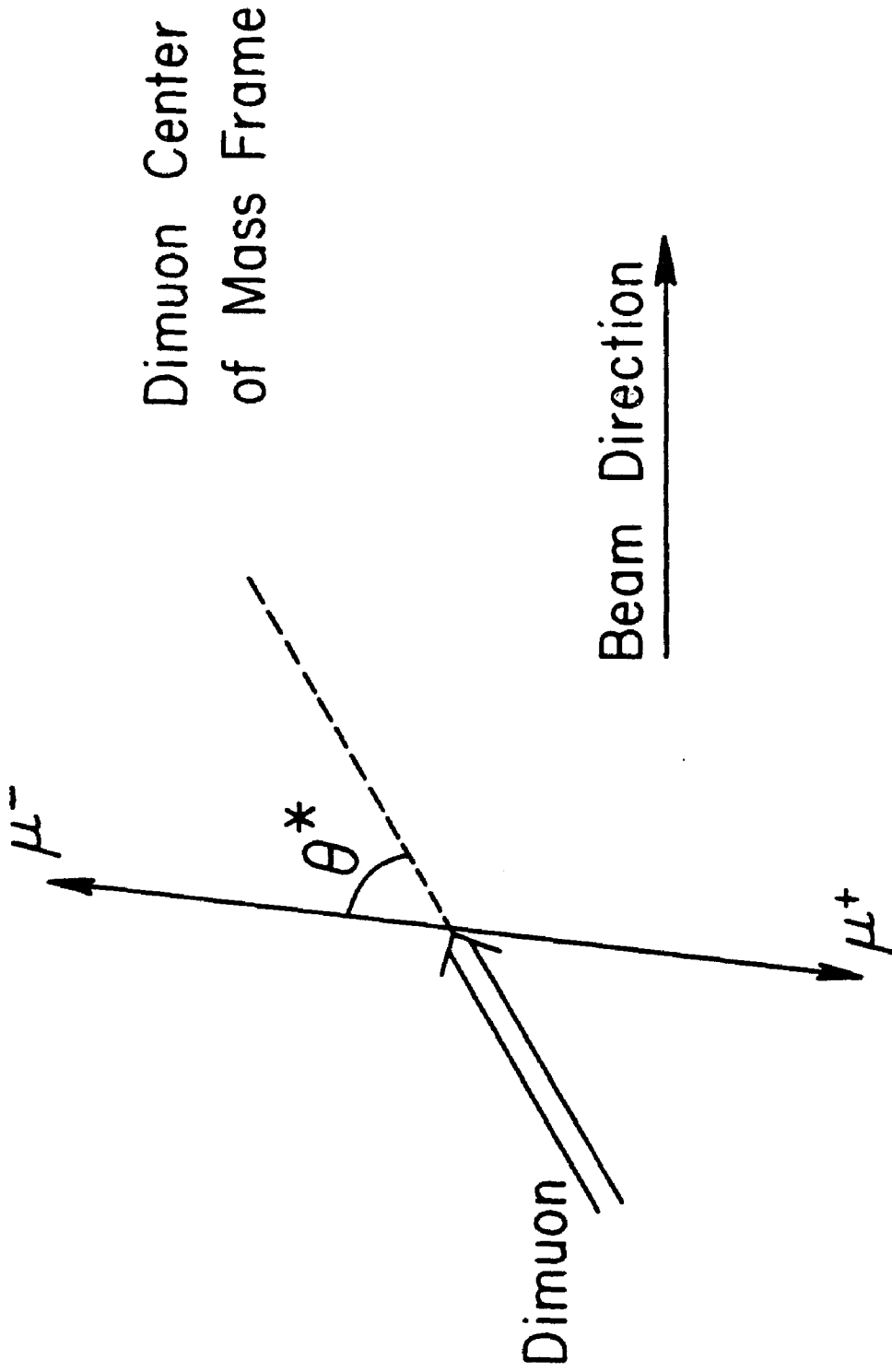


FIGURE 1-3. θ^* IS DEFINED AS THE ANGLE BETWEEN THE μ^- AND THE DIMUON DIRECTION IN THE FRAME IN WHICH THE DIMUON IS AT REST.

results not reported here. Principally these are high resolution measurements of differential cross sections for production of ρ, ω, φ and low mass nonresonant μ -pairs. The muon pair contribution to the anomalous yield of single direct muons will be calculated from these measurements over a large range of single muon x_F and transverse momentum. The data from additional detector elements will be used to obtain better resolution and to reject background.

CHAPTER II. APPARATUS

A. Overview

The experiment was performed at the Fermi National Accelerator Laboratory in Batavia Illinois. Figure 2-1 displays the layout of the accelerator and beam lines. In each machine pulse, about 1.5×10^{13} protons were accelerated to an energy of 400 GeV in the main ring of the accelerator, then extracted and divided among the beam lines. The extraction method which is relevant to our beam is the "slow spill" in which protons are extracted uniformly over a period of about 0.8 seconds. Our experiment utilized the Chicago Cyclotron Spectrometer facility, which is in the neutrino area and is labeled "muon spectrometer" in the figure. This spectrometer is served by a beam of secondary particles produced when the primary proton beam strikes the neutrino area target.

Figure 2-2 is a diagram of the apparatus in the muon laboratory. A right handed coordinate system was defined, the origin of which was at the center of the spectrometer magnet. The z axis was along the beam direction; the y axis was vertical; the x axis was directed toward beam left.

In the beam line enclosures upstream of the laboratory were three threshold beam Cerenkov counters, two beam defining counters (T_1 and T_2) and three pairs of veto jaws

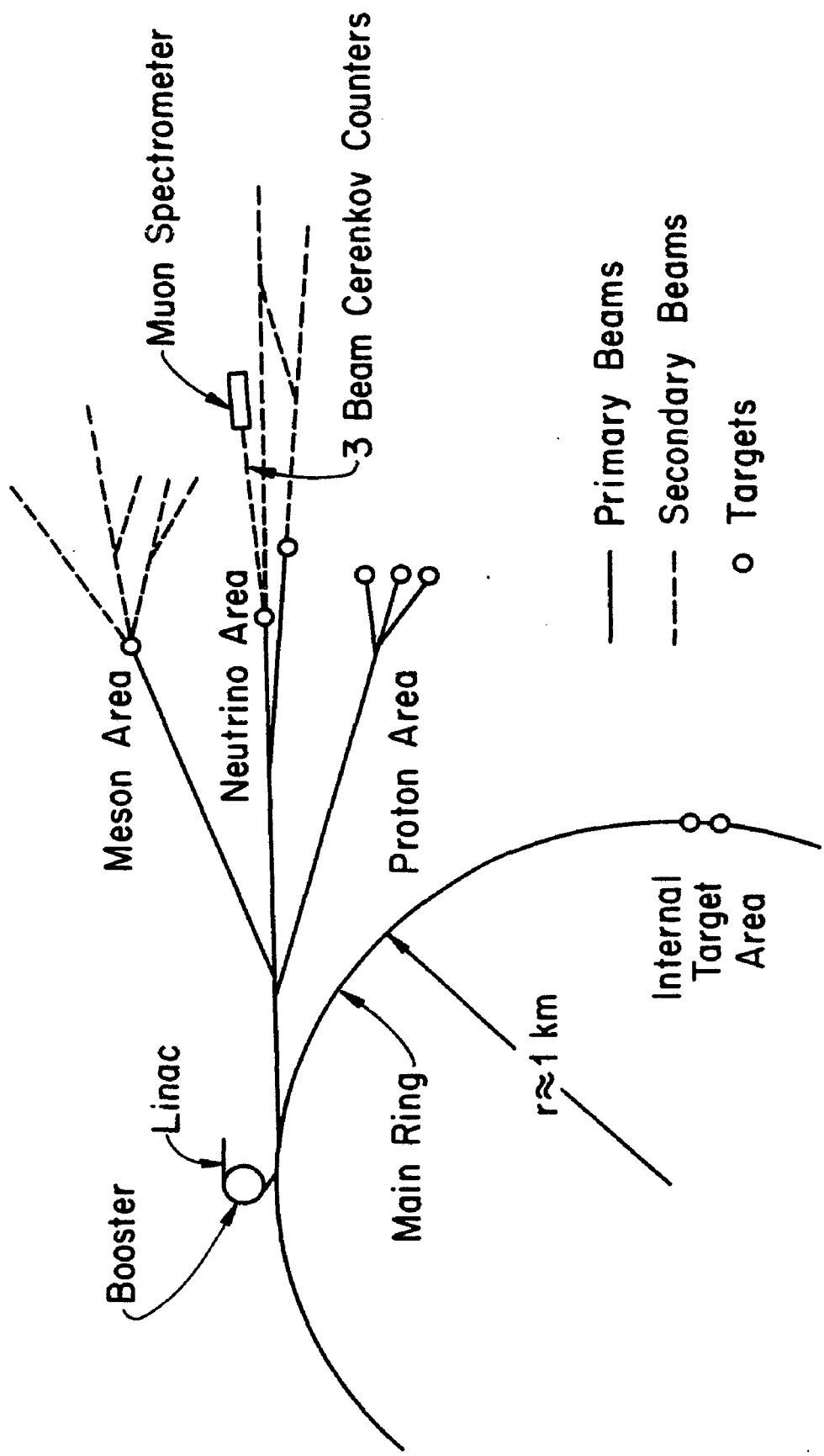


FIGURE 2-1. THE ACCELERATOR AND BEAM LINE LAYOUT AT THE FERMI NATIONAL ACCELERATOR LABORATORY. OUR EXPERIMENT WAS PERFORMED IN THE BUILDING LABELED MUON SPECTROMETER.

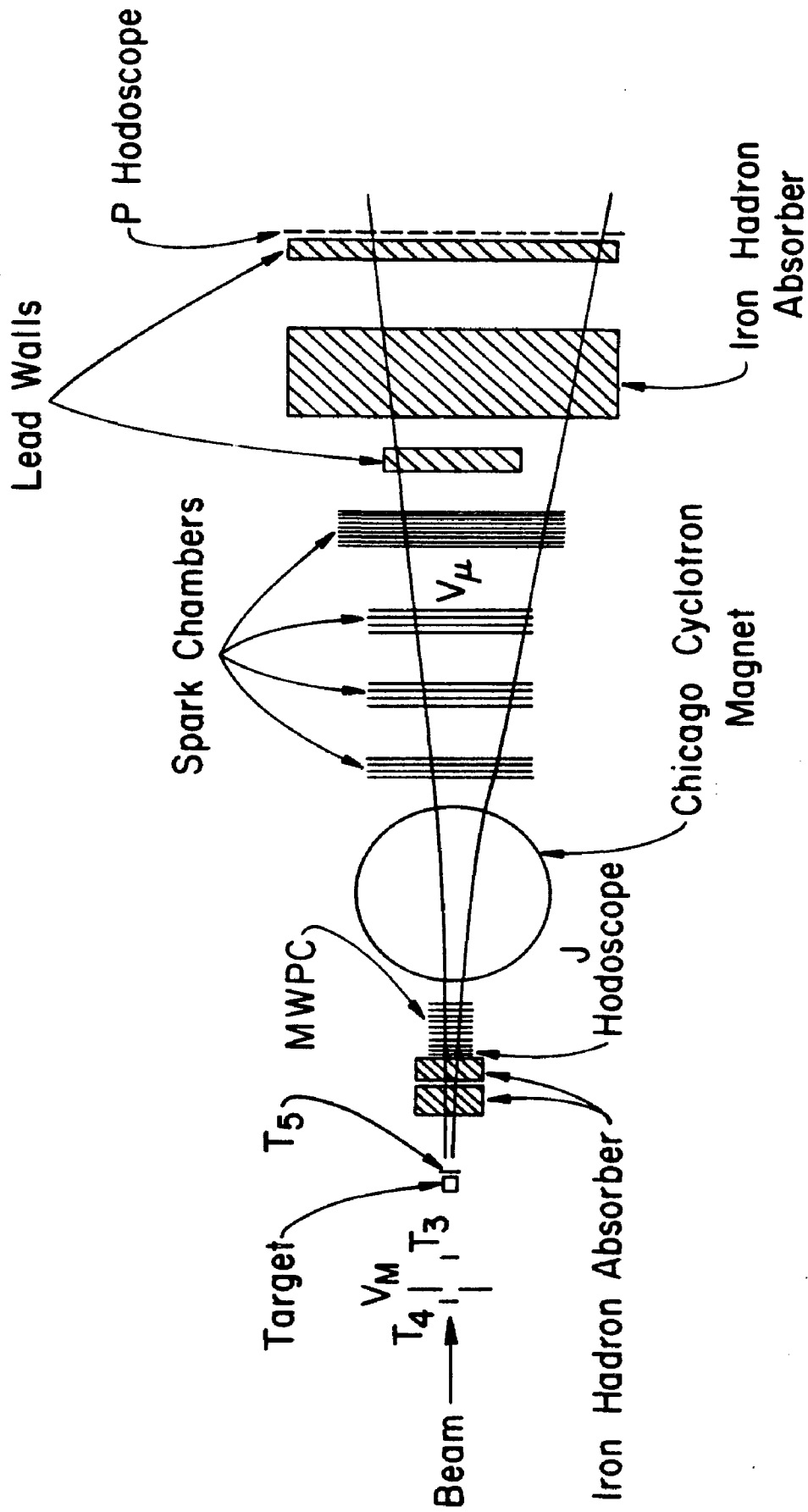


FIGURE 2-2. DIAGRAM OF APPARATUS IN THE MUON LABORATORY.

(V_{jaw}) which surrounded the beam.

The first element inside the muon lab was a beam defining counter (T_4). It was followed immediately by an array of counters (V_M) that was used to veto muons outside of the beam. Final beam definition was done upstream of the target by the counter (T_3). Immediately downstream of the target was a counter (T_5) used to determine whether an interaction took place within the target. A 2.2 meter thick block of iron 1.4 meters downstream of the target, absorbed hadrons before a significant fraction of them decayed. Next were eight planes of multiwire proportional chambers (MWPC) followed by the Chicago Cyclotron Magnet (CCM) and twenty planes of spark chambers. A three inch by three inch counter (V_{μ}) used to veto beam muons was placed just after the first 12 spark chamber planes. Following the spark chambers was a lead wall, which was left by the previous users of the spectrometer. Further downstream was a 2.5 meter thick wall, which improved our hadron rejection. Finally, the muon identifying hodoscope (P hodoscope) was just downstream of a lead wall that reduced hits in the hodoscope from electromagnetic showers accompanying single muons.

A large part of the apparatus was assembled by Fermilab experiment 98, a Chicago-Harvard-Illinois-Oxford

collaboration (henceforth referred to as E-98), which used the detector to measure deep inelastic muon scattering. Because E-98 was scheduled to run after we took data, many constraints were placed upon our reconfiguration of the apparatus.

B. The Beam Line

Primary protons, usually with a momentum of 400 GeV/c (300 GeV/c for 10 percent of the run), were incident upon a twelve inch (one interaction length) thick aluminum target. Particles produced in this target, at 0.8 milliradians, with momentum within two percent of 222 GeV/c, were accepted by our secondary beam line.

Figure 2-3 is a diagram of the beam line. Because of the long distance (about 1500 feet) from the primary target to the first focusing magnets in the secondary beam line, the yield of particles in the muon lab per primary proton was very small. During normal positive beam running conditions, the yield was 5.0×10^{-7} particles per primary proton. For negative beam running, the yield was 6×10^{-8} particles per primary proton. Because the path length from the primary target to the muon lab was long, around 4 percent of the pions and 27 percent of the kaons decayed. This caused muon contamination in the beam at a low level (about 0.2 percent for positive beam) and a muon "halo"

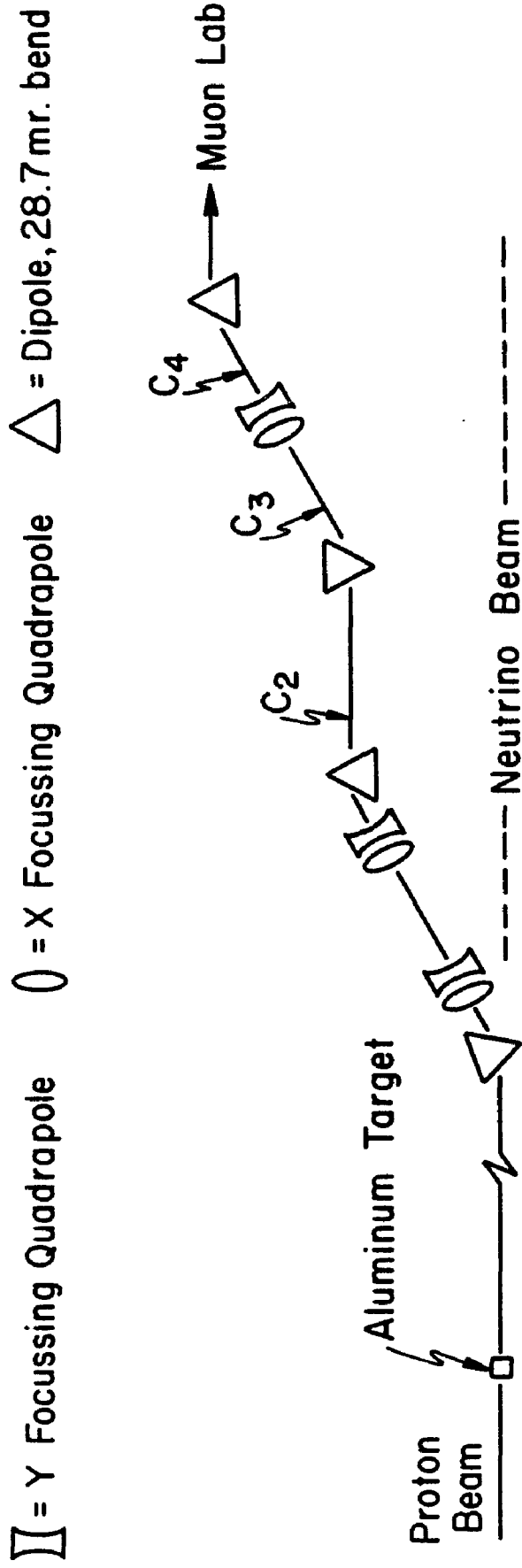


FIGURE 2-3. DIAGRAM OF THE BEAM LINE.

around the beam. The total halo was about six percent of the beam rate for the positive beam. These halo muons are most intense near the beam, but are spread over the transverse extent of the detector.

Due to the radio frequency acceleration in the main ring, the extracted protons were not uniformly distributed in time. They were grouped in "RF buckets" that were less than two nanoseconds in duration and about twenty nanoseconds apart. Because the usual running intensity was 3×10^6 particles per pulse (for negative beam, 5×10^5 particles per pulse), only seven percent of the RF buckets contained more than one particle.

We studied the beam composition at 222 GeV/c using the threshold Cerenkov counters discussed in the next section. The results, shown below, are a combination of this study and a measurement made by Aubert²³ et al. at 300 GeV/c in the same beam line.

BEAM COMPOSITION

positive beam	protons	.84
	π^+	.138
	K^+	.022
negative beam	π^-	.965
	K^-	.03
	\bar{p}	.005

C. Beam Cerenkov Counters

Three threshold Cerenkov counters were used to identify beam particles. They were located in enclosures 102, 103 and 104 and are labeled C_2 , C_3 and C_4 in figure 2-3. The beam pipes upstream of the counters contained helium at less than atmospheric pressure. The helium was used as a radiator of Cerenkov light which was focussed by a parabolic mirror on an ECA C3100CM photomultiplier tube as shown in figure 2-4. A quartz window was used to separate the tube from the partially evacuated counter to match the phototube's efficiency in the UV. The counters C_2 and C_4 were built for our experiment, while C_3 had been used for the studies of Aubert et. al. The design of C_3 was very similar to that of C_2 and C_4 . The major difference was that the C_3 mirror was only 10 inches in diameter.

The mirror orientation was adjusted after the counters were in position by placing a light bulb at the far end of

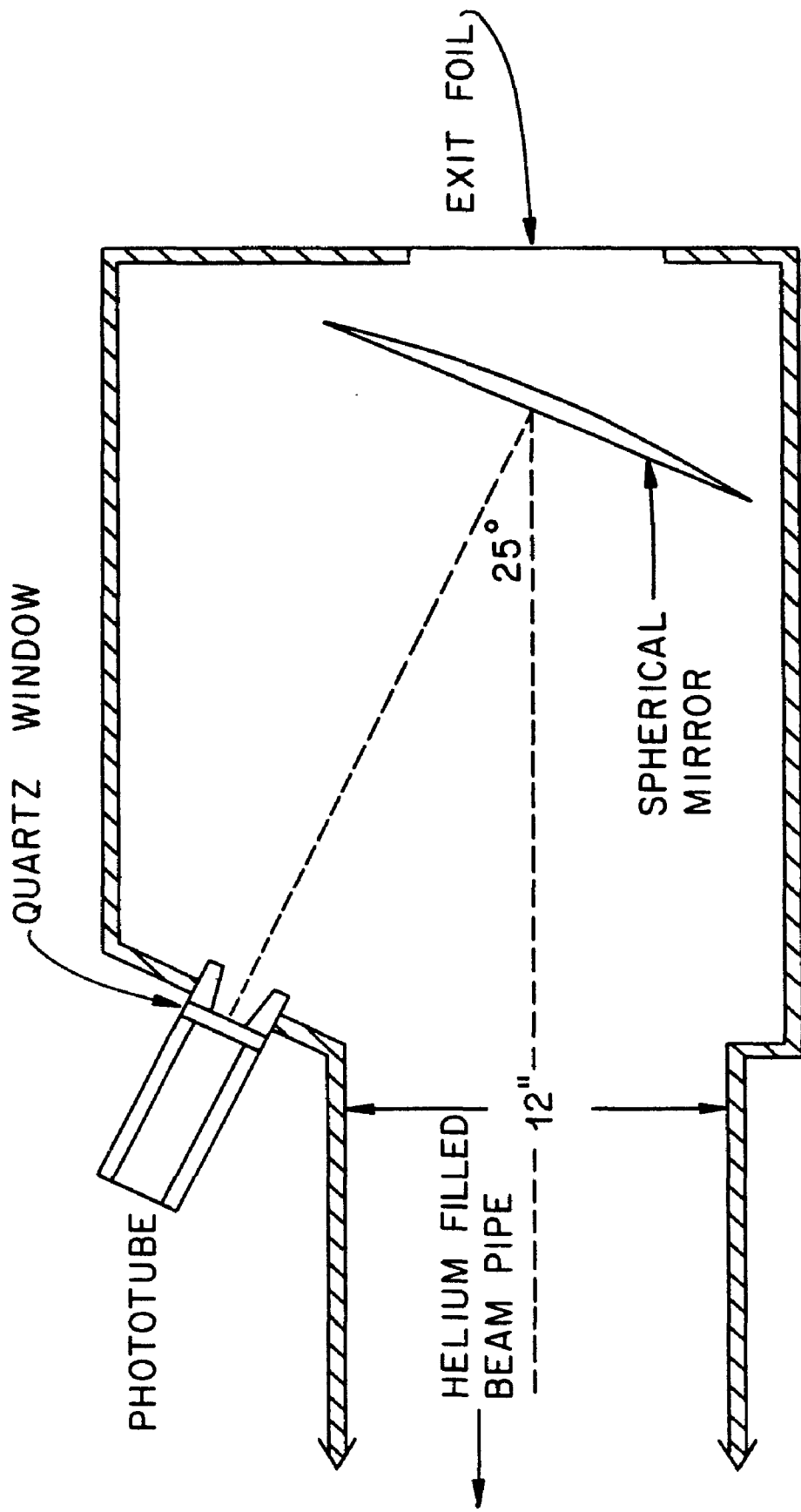


FIGURE 2-4. SIMPLIFIED DRAWING OF A BEAM CERENKOV COUNTER. LIGHT EMITTED BY THE GASEOUS HELIUM RADIATOR IS FOCUSED ON THE PHOTOCATHODE OF AN RCA 3100M PHOTOMULTIPLIER TUBE BY THE ALUMINIZED SURFACE OF A SPHERICAL LUCITE MIRROR. BEAM PARTICLES PASS THROUGH THE 1/8 INCH THICK MIRROR AND A TUNGSTEN EXIT FOIL.

the beam pipe upstream of the counter and viewing its image at the photocathode position.

For positive beam running the Cerenkov counters were set to be efficient on pions and kaons but not on protons. A sample pressure curve is shown in figure 2-5. For negative running, the Cerenkov information was not used in the analysis. By comparing the photomultiplier output for single photoelectron noise to that from a beam pion, the average number of photoelectrons generated by a beam pion was determined to be about 15. The efficiencies and accidental probabilities of the Cerenkov counters are discussed in chapter IV, section B.

D. The Veto Counters

Several counters were used to veto false triggers caused by muon contamination in the beam and the halo surrounding it. First, at the downstream end of each of the three dipoles in enclosure 104, the beam passed through a four inch diameter hole in a jaw counter, composed of two scintillators with semicircular pieces removed from their ends. A halo particle hitting any of these six scintillators produced a pulse V_{jaw} to inhibit the trigger logic.

Similarly, halo particles in the muon laboratory were detected by a three foot high, six feet wide hodoscope V_M ,

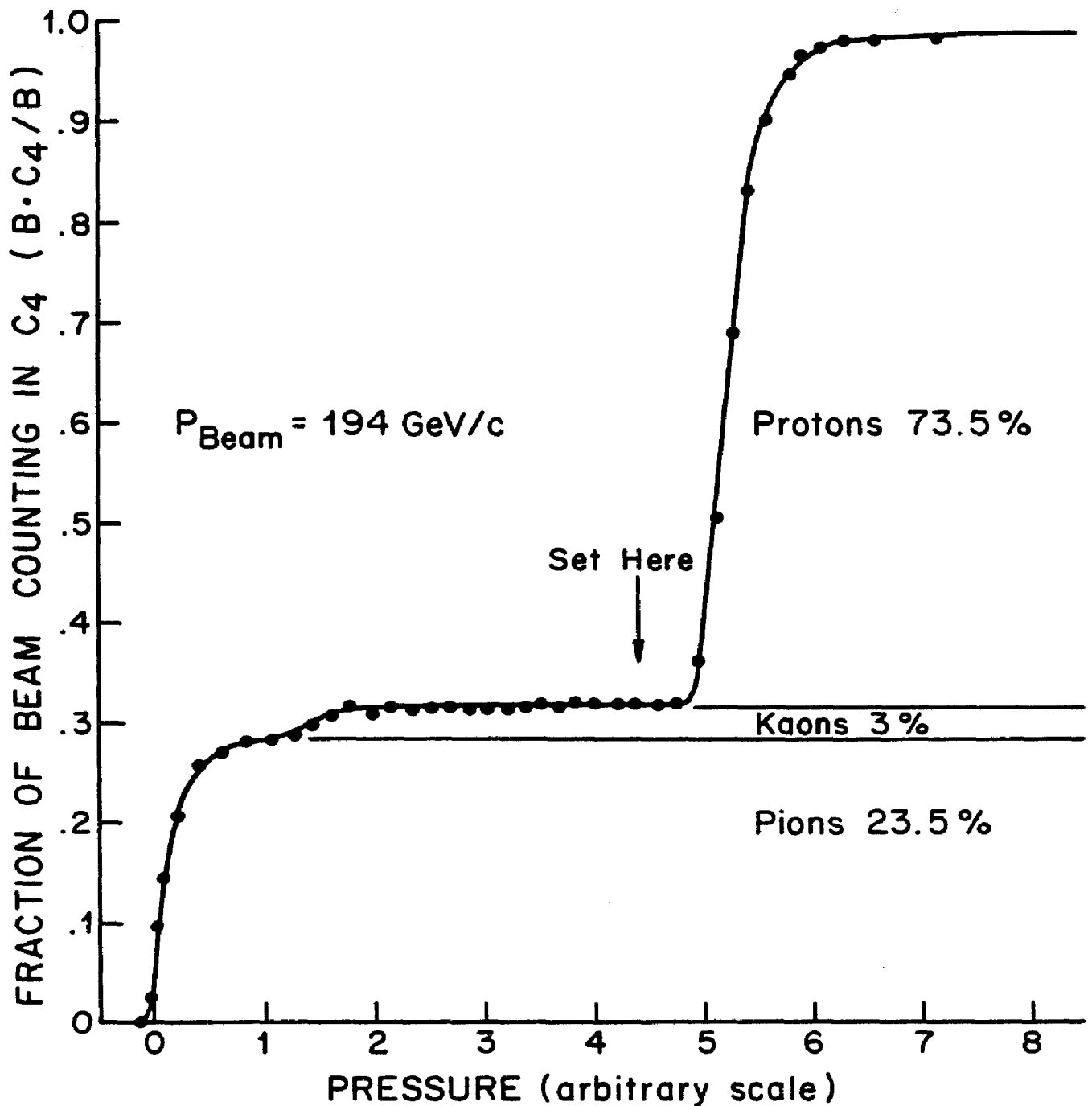


FIGURE 2-5. PRESSURE CURVE FOR C_4 . AS THE HELIUM PRESSURE IN THE BEAM PIPE IS INCREASED, THE INDEX OF REFRACTION IS INCREASED AND HEAVIER PARTICLES BEGIN TO CAUSE CERENKOV RADIATION. AS SEEN IN THE FIGURE, A VERY GOOD SEPARATION OF PIONS AND PROTONS WAS POSSIBLE. KAONS WERE COUNTED AS PIONS UNDER NORMAL RUNNING CONDITIONS.

consisting of eight 18 inch square counters, slightly overlapped to avoid inefficiencies. A two inch square hole was left for the beam. This hodoscope was positioned sufficiently far upstream of the target (9 feet) to insure that "backsplash" particles from an interaction in the target arrived at V_M too late to veto a trigger from that interaction.

The two inch hole in V_M was covered by a three inch by three inch counter (T_4). Triggers were vetoed if the pulse height from T_4 was greater than about 1.5 times that expected from one minimum ionizing particle. To remove beam buckets with more than one particle, a similar pulse height requirement was made on T_3 , a one and one-half inch by one and one-half inch beam defining counter (see next section). Finally, muons in the beam were vetoed by V_μ , a three inch square scintillator centered on the deflected beam line at a distance eight meters downstream of the center of the CCM. Because the CCM polarity was never reversed, V_μ had to be repositioned each time the beam polarity was changed.

2. The Beam Defining Counters

Four scintillation counters were used to define the incoming beam. The first counter (T_1) was located in the upstream end of enclosure 104 and was three inches by three inches in size. A two inch by two inch counter (T_2) was

placed in downstream 104. Another three inch by three inch counter (T_4), which was around three meters upstream of the target, was required in the beam definition, although its main purpose was to veto beam particles accompanied by halo muons (see previous section). The final beam defining counter (T_3) was 1.5 inches by 1.5 inches in size and 1.76 meters upstream of the target. The target was positioned 9.91 meters upstream of the magnet's center.

F. The Interaction Counter (T_5)

A 2 1/2 inch by 2 1/2 inch counter (T_5), placed five inches downstream of the target, was used to determine whether an interaction had occurred there. The primary trigger required that the pulse height in T_5 be greater than or equal to two times minimum ionizing. In this way, interactions which occurred in the shield would not cause triggers. To assure that this trigger requirement did not cause a significant inefficiency, a prescaled trigger not requiring T_5 was used. By latching T_5 and recording its pulse height on an ADC, an efficiency could be calculated for each ADC channel (figure 2-6). This efficiency along with the pulse height distribution for good events with $0.65 \text{ GeV}/c^2 < m < 1.0 \text{ GeV}/c^2$ is shown in figure 2-6. Using these data, we calculate a one percent inefficiency due to

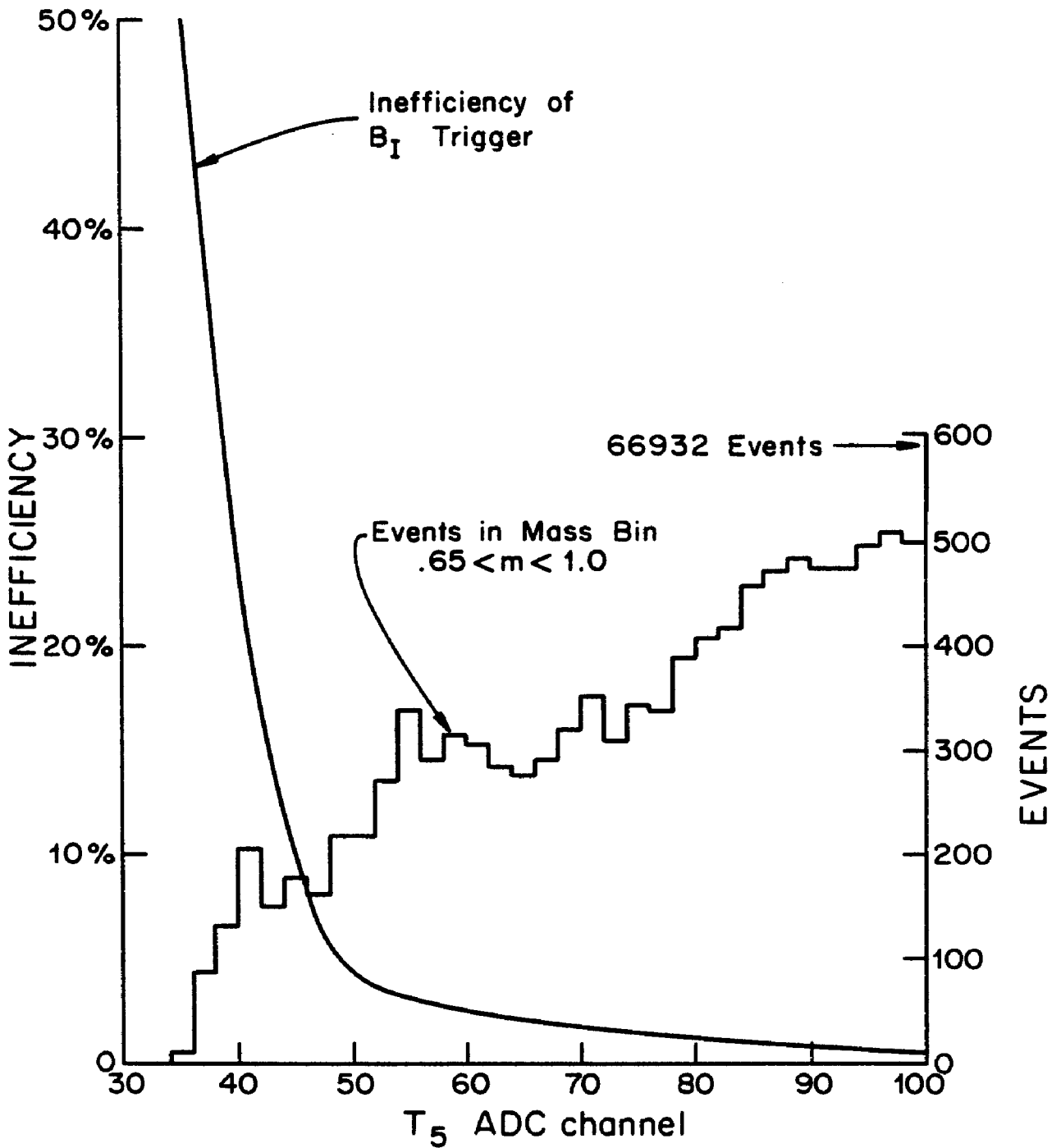


FIGURE 2-6. THE INEFFICIENCY OF THE B₁ TRIGGER IS PLOTTED ALONG WITH THE NUMBER OF EVENTS IN THE MASS BIN $0.65 < m < 1.0$ AS A FUNCTION OF T₅ ADC CHANNEL. THERE ARE 66932 EVENTS ABOVE CHANNEL 100. THE OVERALL B₁ TRIGGER INEFFICIENCY IS CALCULATED FROM THESE DATA TO BE 1%.

G. The Multiwire Proportional Chambers

Eight planes of multiwire proportional chambers one meter by one meter in active area were located just downstream of the first hadron absorber. They were used to measure the direction cosines of each muon before it entered the field of the CCM. These chambers were built by the E-98 collaboration at the Enrico Fermi Institute and are described in detail in reference 24. Four planes measured the x coordinate and four planes measured the y coordinate. The wire spacing in these MWPC'S was 1.5 mm and the theoretical chamber resolution (0.43 mm) was consistent with χ^2 distributions from the track finding program. Typical chamber efficiencies, computed from muon tracks in good events, are shown in the following table. The effects of the rather large inefficiencies in these chambers are discussed in chapter III, section F.

<u>Plane Type</u>	<u>Z Position</u>	<u>Efficiency</u>
y	4.74	.83
x	4.56	.90
y	4.21	.93
x	4.03	.89
y	3.69	.93
x	3.51	.89
y	3.17	.86
x	2.99	.72

H. The Spark Chambers

Twenty planes of spark chambers, built by the E-98 collaboration, were used to measure trajectories of each muon downstream of the CCM. The first twelve of these planes, two meters in height by four meters in width, were built at the University of Chicago. The last eight planes, two meters by six meters, were constructed at Harvard University. On all of the planes the wires were spaced 1/20 inch apart and during normal operation the measured spark chamber resolution was about 0.5 mm. Of the twenty planes, nine had vertical wires and the remaining eleven had wires at an angle of $\pm \arctan(1/8)$ to the vertical. The following table summarizes the plane positioning.

Type	<u>Distance from Magnet Center (meters)</u>
Two by Four Meter Planes	
u	3.88
x	3.89
x	4.00
v	4.01
u	4.88
x	4.89
x	5.00
v	5.01
u	5.91
x	5.92
x	6.03
v	6.04
Two by Six Meter Planes	
u	8.69
x	8.70
u	8.86
x	8.87
v	9.02
u	9.04
x	9.19
v	9.20

The spark chamber efficiencies are discussed in chapter III,

section B.

The readout of the two by four meter chambers was designed to operate in the fringe field of the CCM. Each chamber wire was the input to one bit in a shift register. After the RF noise from the spark chamber pulse had subsided, the data were shifted along through the readout system and bits were interrogated one at a time by a "scanner". The details of these chambers, their readout, and their pulsing system, are described in reference 25.

The two by six meter chambers were read out by conventional magnetostrictive wands. Their details along with their pulsing system and readout are described in reference 26.

All of the chambers were operated with essentially the same system as described in the references. One important exception is that the polarity of the central D. C. clearing fields on the two by four meter chambers was reversed. This caused the memory time of these chambers to decrease from about ten microseconds to one microsecond.

I. The Chicago Cyclotron Magnet

The magnet used in the spectrometer was that from the 300 MeV University of Chicago synchro-cyclotron. The field had an effective diameter of 5.18 meters and the gap between the pole tips was widened to 1.29 meters for use at

Fermilab. This gave the magnet an aperture slightly larger than the acceptance in the vertical direction and much larger than the horizontal acceptance of the rest of the detector.

The magnetic field was approximated as a hard edged cylinder with $B=6.984$ kilogauss inside a radius of 2.59 meters and $E=0$ outside. We determined these numbers by computer tracking of particles through the magnet using field maps obtained from E-98. The field at the center of the magnet was measured by us with an NMR probe.

J. The P Hodoscope

The P hodoscope was a key element in the dimuon trigger (see section I of this chapter), and was used, in the reconstruction (chapter III section C), to assure that the tracks downstream of the magnet were due to muons in time with the trigger. Figure 2-7 is a diagram showing the positions and sizes of the P hodoscope counters. The asymmetries of the arrangement were necessary because of the position of the E-98 fast electronics. There were 53 counters in all, each four feet long. The counter widths varied, being smallest near the beam and larger away from the beam. This arrangement reduced the acceptance lost by requiring two nonadjacent counters in the trigger. The counters were overlapped slightly and were no more than $3/4$

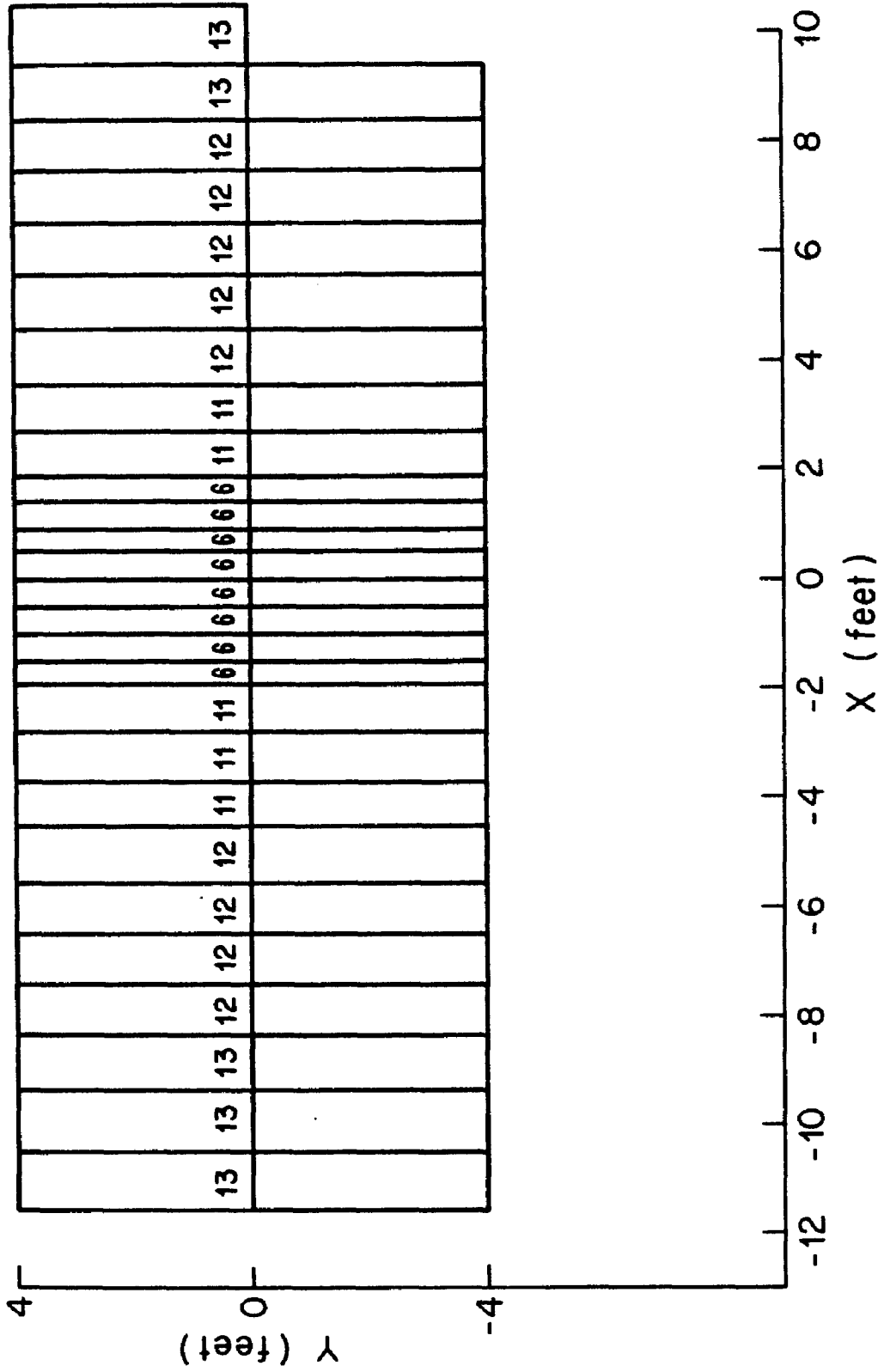


FIGURE 2-7. VIEW OF P HODSCOPE FACING UPSTREAM. THE X AND Y SCALES ARE SHOWN IN FEET AND THE COUNTER WIDTHS ARE GIVEN IN INCHES.

inches downstream of an eight inch thick lead wall that absorbed electromagnetic showers which accompanied muons. Because of lead's short radiation length, only showers which were produced near to the hodoscope could have an effect. These showers were unlikely to have spread out enough to hit more than two adjacent counters.

The scintillator used was Pilot Y in either 1/2 inch or 1/4 inch thickness. Light was collected from each counter through an adiabatic lucite light pipe and detected by an RCA 8575 photomultiplier tube. Phototube signals were discriminated and latched. We measured the counter efficiencies by triggering on muons near the point where light collection was worst. Phototube voltages were set to be 100 volts above the efficiency plateau.

K. The J Hodoscope

The J hodoscope was employed to reduce the trigger rate of the experiment so that higher beam intensity could be used (see section L of this chapter). It imposed a minimum μ -pair opening angle requirement in the trigger. When the J hodoscope cut was used, beam intensity was not limited by the trigger rate. This requirement drastically reduced the acceptance for μ -pairs with masses less than $500 \text{ MeV}/c^2$ and for μ -pairs coming from the hadron absorber, while leaving the acceptance essentially unchanged for masses greater than

1 GeV/c². Figure 2-8 is a diagram of the J hodoscope showing the arrangement and sizes of counters. The hodoscope consisted of eleven counters measuring the x-position of a hit and nine counters measuring the y-position.

One-fourth inch thick Pilot Y was used as scintillator. Since most counters were narrow, only simple light pipes were needed. These had a 90 degrees bend so that the FCA 8575 photomultiplier tubes could be easily shielded from the fringe field of the Chicago Cyclotron Magnet. The shielding was provided by iron pipes spaced about one-fourth inch outside μ -metal shields which covered the phototube.

Using a muon beam, we set the voltages of the photomultiplier tubes so that the output signals were four times the 100 millivolt discriminator thresholds. Counter and latch efficiencies were checked using tracks in the one by one meter MWPC's.

L. The Trigger and Fast Electronics

Using the counters described in previous sections of this chapter, we developed a system of electronics to trigger efficiently on muon pairs produced in the target by a beam particle. Stated simply, the trigger requirements were: one and only one beam particle incident upon the target, two or more particles leaving the target, and two or

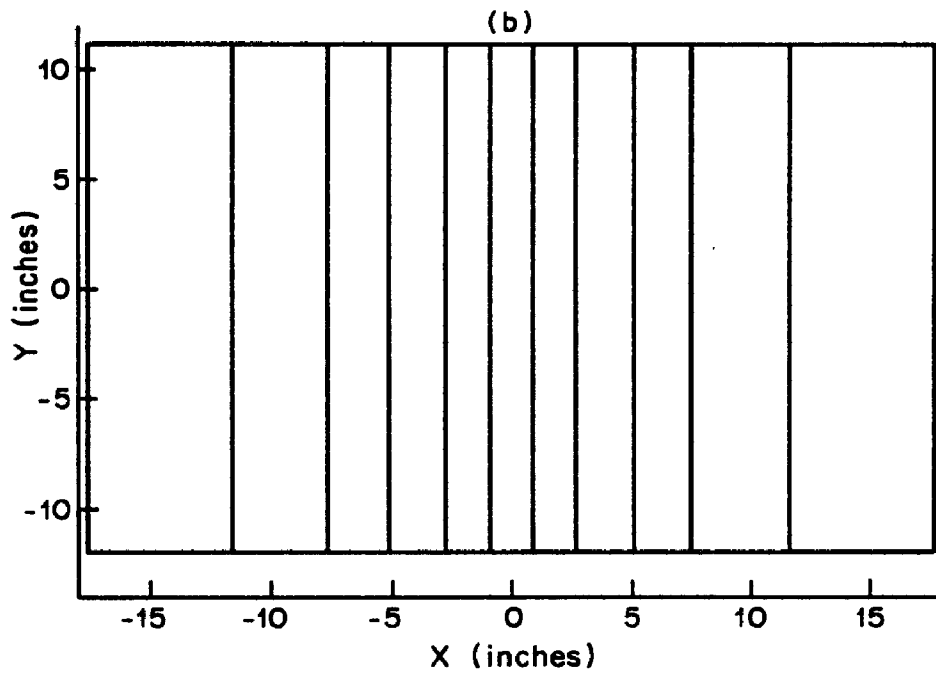
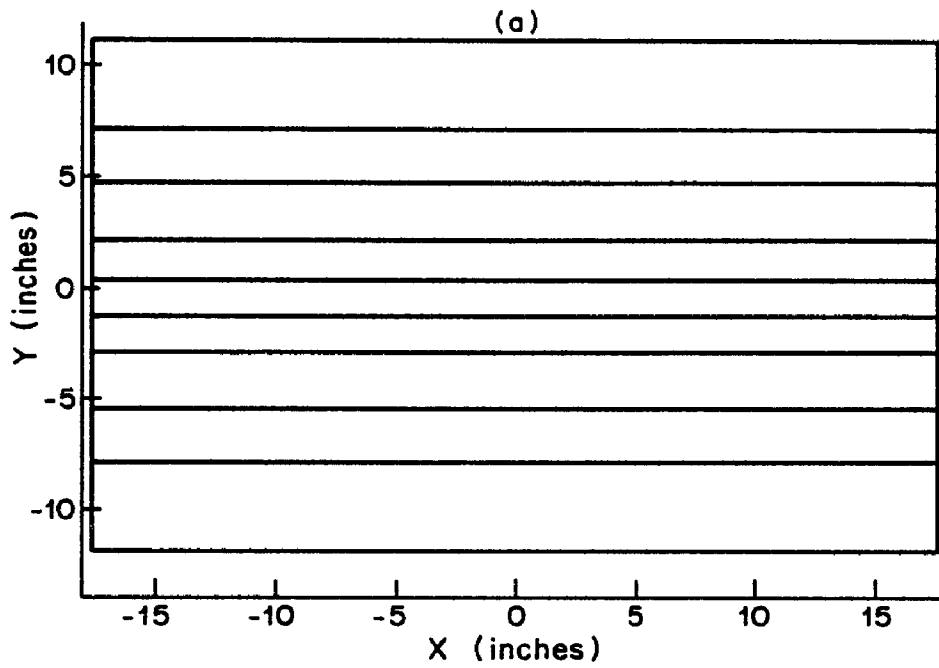


FIGURE 2-8. VIEW OF J HODOSCOPE FACING UPSTREAM. THE Y PLANE IS SHOWN IN (A) AND THE X PLANE IS SHOWN IN (B). SCALES ARE IN INCHES.

more muons with enough energy to reach the F hodoscope. For some of the running, a minimum μ -pair opening angle upstream of the magnet was also required.

Figure 2-9 is a diagram of the trigger electronics. Some intermediate logic levels are shown which I will define here.

$$B'' = T_1 * T_2 * T_3 * T_4$$

$$B' = T_1 * T_2 * T_3 * T_4 * (B'') \text{ delayed one RF bucket}$$

$$V = V_M + V_\mu + V_{\text{jaw}} + (T_3)_{\geq 2} + (T_4)_{\geq 2}$$

$$E = B' * V$$

$$B_I = B' * V * (T_5)_{\geq 2}$$

P = two nonadjacent P hodoscope counters

J = two nonadjacent J counters in either x or y

J' = one or more J hodoscope counter in x and in y

To generate P, the discriminator output signals from all of the P hodoscope counters were summed and the sum was discriminated at two levels (sum ≥ 2 counters and sum ≥ 3 counters). The discriminated counter signals were inputs to a veto circuit which returned a veto output if any two adjacent counters were hit. A coincidence between any two of the three signals, sum ≥ 2 , sum ≥ 3 , and V_{adjacent} were required to give P. A similar procedure was followed for

Logic Diagram of Trigger Electronics

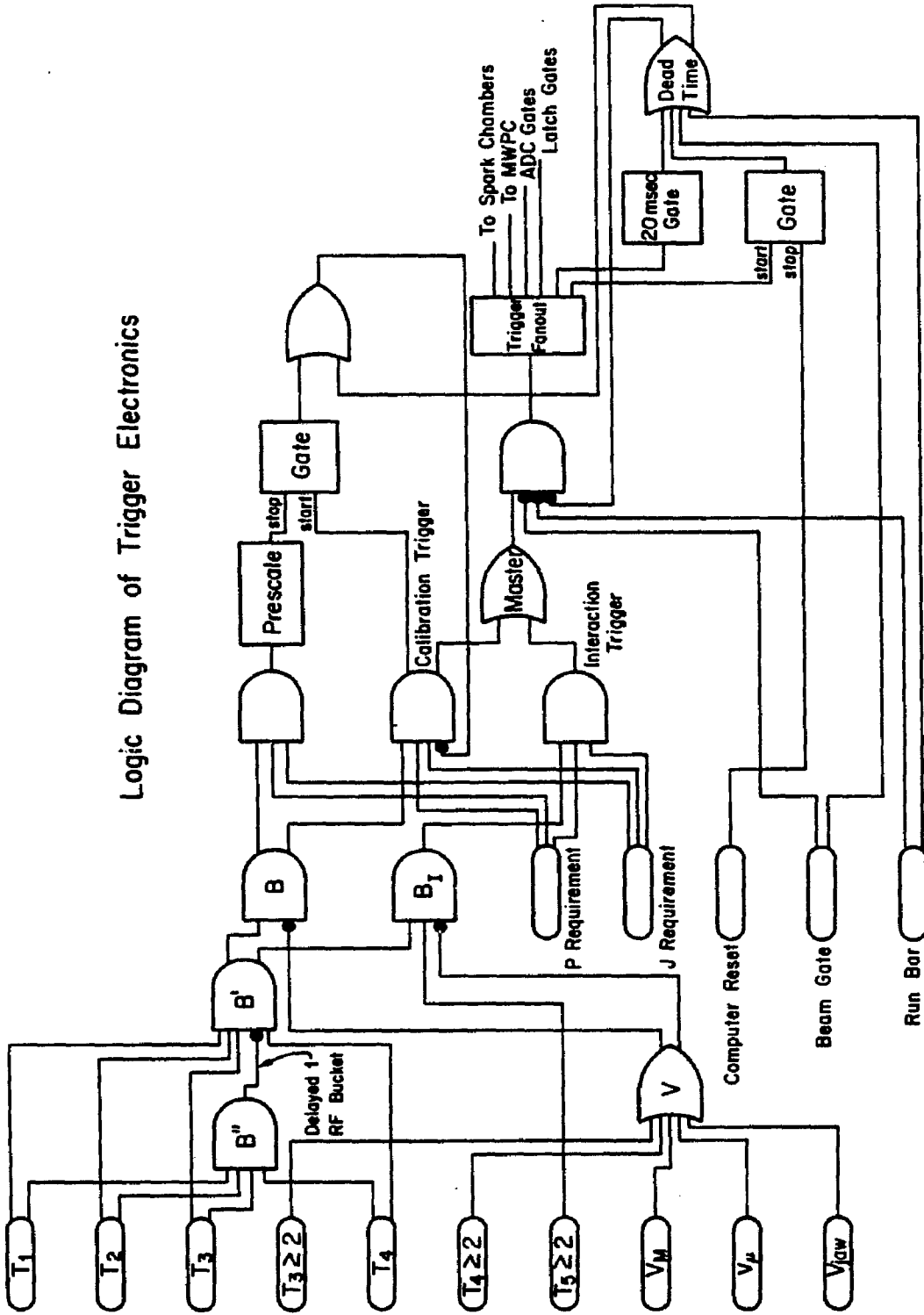


FIGURE 2-9

each of the J hodoscope planes and the results were CPed to give the J signal.

When we ran with a high intensity beam, two types of triggers were simultaneously taken. They were $B_I * P * J$ and $(B * P * J)$ prescaled. During low intensity running, the two triggers used were $B_I * P * J'$ and $(B * P * J')$ prescaled. The prescaled triggers were taken mainly to be used to check elements of the detector and to tune up analysis techniques.

After each trigger, a "lead time" of around 20 milliseconds was imposed so that all the data could be transferred to the computer and to allow spark chambers to recover from having been pulsed. During this time no triggers were accepted and scalars were gated off.

Many coincidences besides those discussed above were generated and scaled using CAMAC scalars during the live time of the detector. These were used to normalize the data to the incident flux of particles and to monitor detector performance. The pulse heights of counters T_3 , T_4 , T_5 , C_2 , C_3 , and C_4 were recorded using CAMAC ADC 's.

M. Data Acquisition

All detector information was transferred to a SIGMA III on-line computer via CAMAC. The computer received the data from CAMAC and wrote it in essentially the same form on

magnetic tape. The data were written in 600 word (16 bits/word) records. Each event was composed of one or more records, depending on the number of hits in the spark chambers and proportional chambers.

The Sigma III also performed other tasks to check detector operation. It monitored scaler ratios, chamber efficiencies, chamber readout errors, Cerenkov counter efficiencies, and trigger errors. A large number of data displays were available using a CRT. These included chamber and hodoscope multiplicity distributions, counter pulse height distributions, raw data printout, and many event displays either showing an overall picture of an event or emphasizing one part of the detector.

CHAPTER III. Event Reconstruction

The objective of the reconstruction program was to find muon tracks in the spectrometer. In the MWPC's upstream of the magnet, tracks (groups of hits in chambers which fit to a straight line) were found in the x view and the y view separately. Tracks were found in three space in the spark chambers downstream of the magnet. A muon track was then a track in the spark chambers which linked to an x-track and a y-track in the MWPC's upstream of the magnet and which pointed to a hit in the F hodoscope.

A. The Upstream Track Finder

The track finding started in the 8 planes of proportional chambers upstream of the CCM (see chapter II section G). There were four x-planes and four y-planes so the tracks could only be found in each view separately.

To find three or four point tracks, in x for example, all pairs of hits in two planes were used to get an initial line and extra hits were looked for in a 10 millimeter road about the initial line. This was done for two pairs of chambers so that any three point track would be found. A straight line was then fit to the three or four hits. If the probability that this was a good track, as computed from the track χ^2

$$\chi^2 = \sum_i \left(\frac{d x_i}{0.43 \text{ mm}} \right)^2$$

and the number of degrees of freedom, was less than 2 percent, the track was rejected. If a four point track was rejected, each of the four points was dropped in turn to see if there was a three point track satisfying the probability requirement. If two good tracks had two or more points in common, the track having the higher χ^2 was dropped.

All the hits that were not used on a three or four point tracks were used as input to the two point track finder. This track finder made tracks out of all pairs of hits that could have been produced by a muon coming from the target.

In general there were more than just two x-tracks and two y-tracks found upstream. The good upstream tracks were picked out by requiring them to link through the magnet to a downstream track. The additional tracks were mainly two point tracks formed from uncorrelated hits in the MWEC's.

B. Downstream Track Finder

The next step in the reconstruction was to find tracks downstream of the magnet where there were 20 planes of spark chambers (see chapter II section H). With this large redundancy we were able to withstand sizable inefficiencies in some of the chambers. The inefficiencies that occurred made it impossible to start the track search in a specific subset of the chambers, because trying all pairs of chambers

led to a very large number of combinations. therefore we used a more sophisticated method involving the impact parameters of the upstream x-tracks.

Searched for first were x-tracks in the nine planes which measured x. This was done by projecting the x sparks in all the chambers onto a plane of constant z, which was near the average of the downstream chamber positions. Since in a cylindrically symmetric magnetic field the ingoing and outgoing impact parameters of a particle are equal, an upstream x-track could be used to do the projection. Given the impact parameter and a point on the track, the track is determined. After the sparks were projected, a cluster of sparks all falling within a narrow window in x (about 3 mm) was searched for. If a cluster of at least three sparks was found, a search was made in the tilted (u and v) planes.

Every x plane had a tilted plane very near to it in z. In fact the tilted planes were the other side of the chamber gap. For each x spark found in the prior search, the program calculated y positions using each spark in the corresponding tilted plane. A y value calculated from an x spark and an uncorrelated spark in a tilted plane could usually be rejected for being outside the y limits of the chamber because the tilted wires were at only a small angle to the x wires. Each good y value was projected onto the

same z plane using the assumption that the track pointed back to the target. A search was then done for a cluster of y-values within a somewhat wider y window (12.5 mm). The extra width was necessary because the resolution in y in the spark chambers is 8 times worse than in x. If at least three y-values were within the window then the sparks in the tilted planes that generated the y-values and the corresponding x sparks were used as input to a routine which fit a straight line to the spark positions.

After the first fit was made, all sparks within 19 mm of the line were refit. Then all sparks within 4 mm of the new line were fit again. If there were at least three x sparks and three u or v sparks left and if they had a large enough lever arm (62 cm) to define the track adequately, the track was added to the list of downstream tracks and the search for clusters of projected x sparks was resumed. The program made a search using each upstream x-track to project the sparks.

C. The F Counter Requirement

When the track finding was complete, the next task was to determine which downstream tracks were due to muons. This was done by looking for a hit in the P hodoscope (see chapter II section J) that could have been produced by a muon with the trajectory of the downstream track. Since the

angles upstream of the magnet were small compared to the angles of low momentum tracks downstream of the magnet, the momentum was inversely proportional to the position far downstream of the magnet. The x position of the track at the P hodoscope could therefore be used as an indication of the momentum. To allow for multiple scattering, the counters were given an extra width and height of one-third of the x intercept at the P hodoscope or 40 cm whichever was greater. Any track that was within this distance of a hit counter was considered to be a muon track.

D. Linking

The muon tracks downstream of the magnet were then linked to upstream tracks in both x and y. To link in x it was required that the impact parameters of the upstream and downstream tracks be within 25 mm of each other. Figure 3-1 shows a distribution of impact parameter differences.

In y both the intercept at the center of the magnet and the slope could be checked because the vertical bending of the magnet was negligible. A cut was made on the overall error. Distributions of the y intercept difference and y slope difference between upstream and downstream tracks are shown in figures 3-2 and 3-3. The quantity $\left(\frac{\Delta y}{25\text{mm}}\right)^2 + \left(\frac{\Delta y'}{.005}\right)^2$ was required to be less than 25.0 for an acceptable y link.

If there was a linking ambiguity it was resolved by

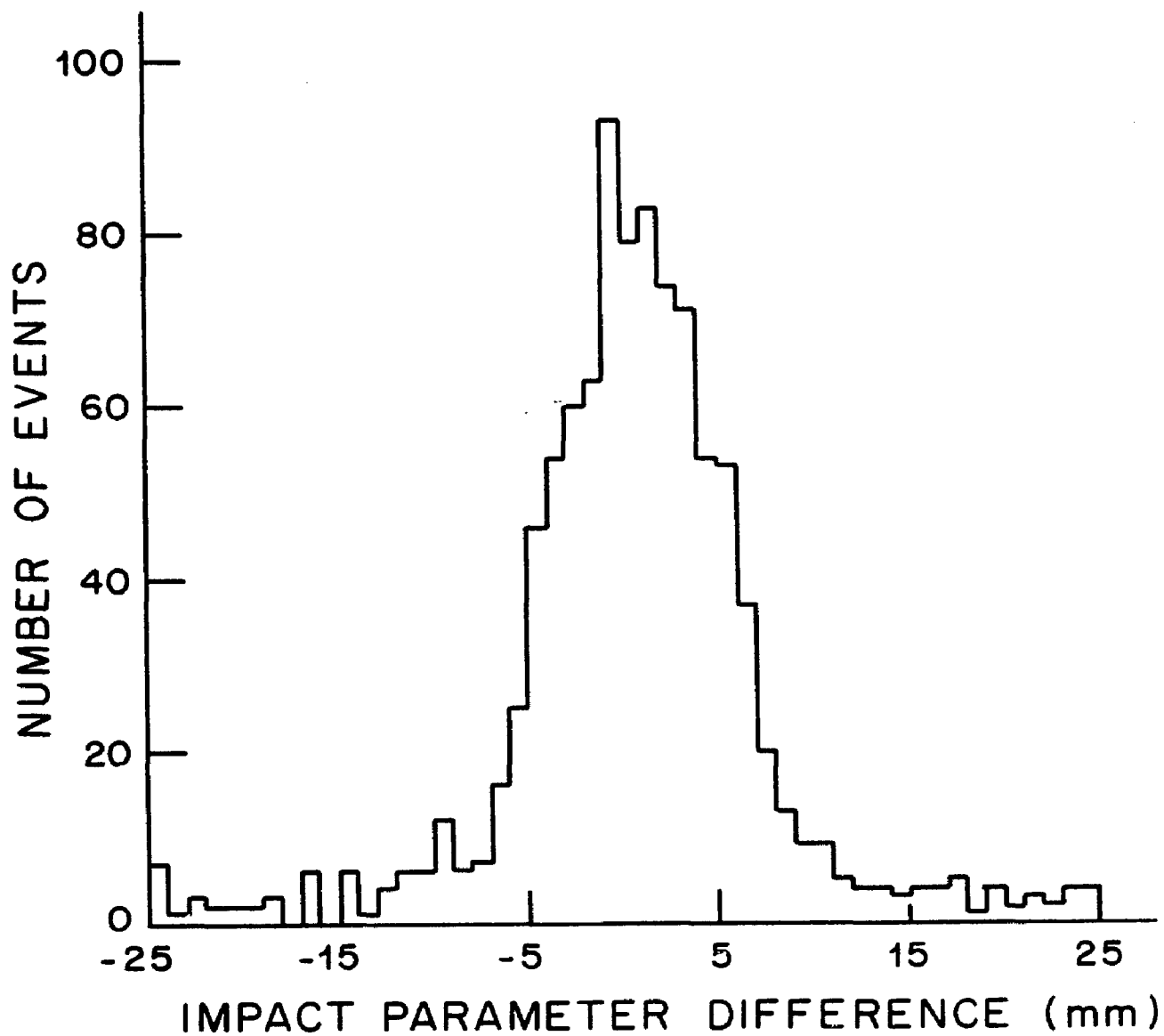


FIGURE 3-1. HISTOGRAM OF EVENTS VERSUS THE DIFFERENCE BETWEEN THE IMPACT PARAMETER OF AN UPSTREAM X TRACK AND THE IMPACT PARAMETER OF A DOWNSTREAM TRACK ($B_{US} - B_{DS}$). THE CUT APPLIED TO THE DATA WAS AT ± 25 MM.

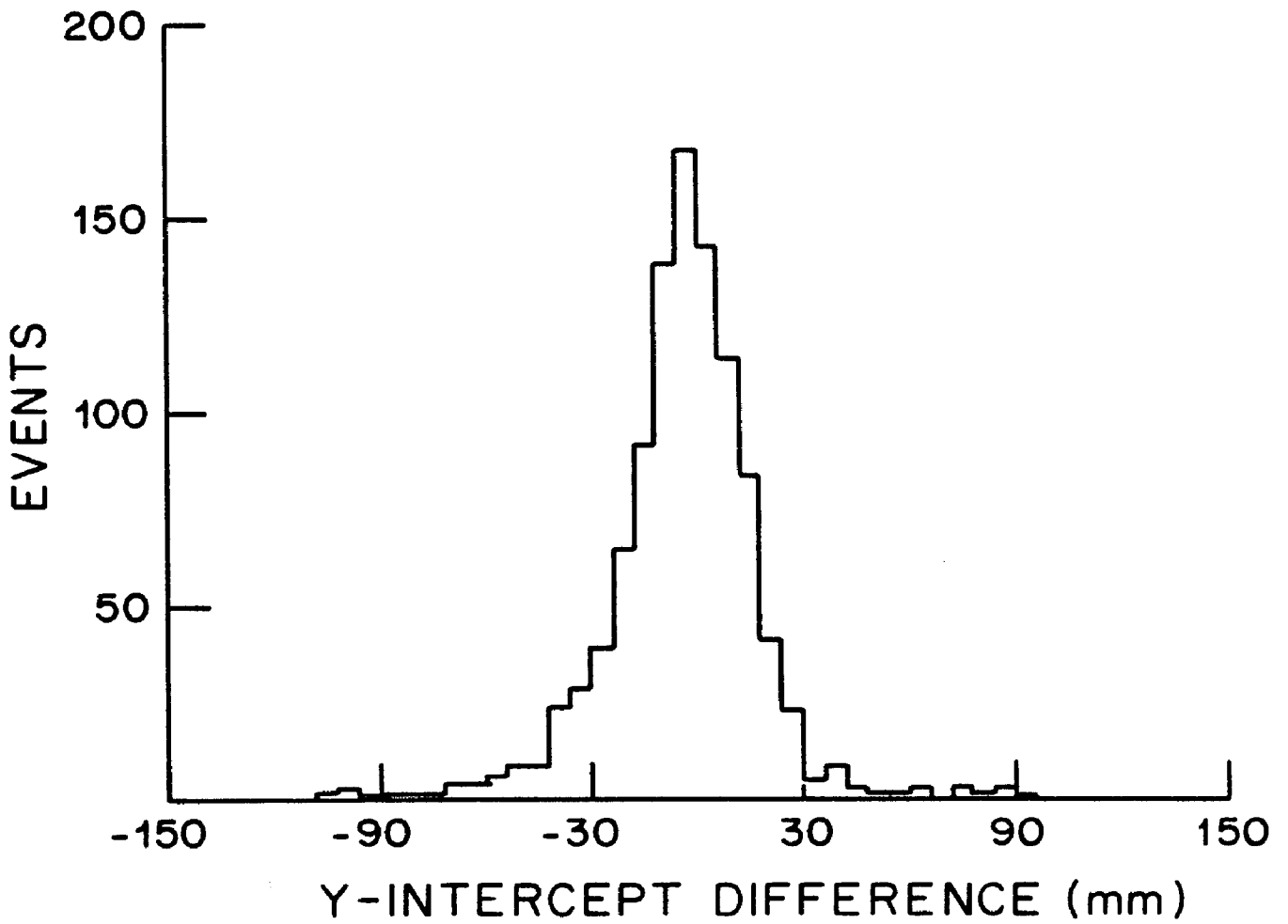


FIGURE 3-2. HISTOGRAM OF DIFFERENCE BETWEEN Y-INTERCEPTS OF UPSTREAM AND DOWNSTREAM TRACKS.

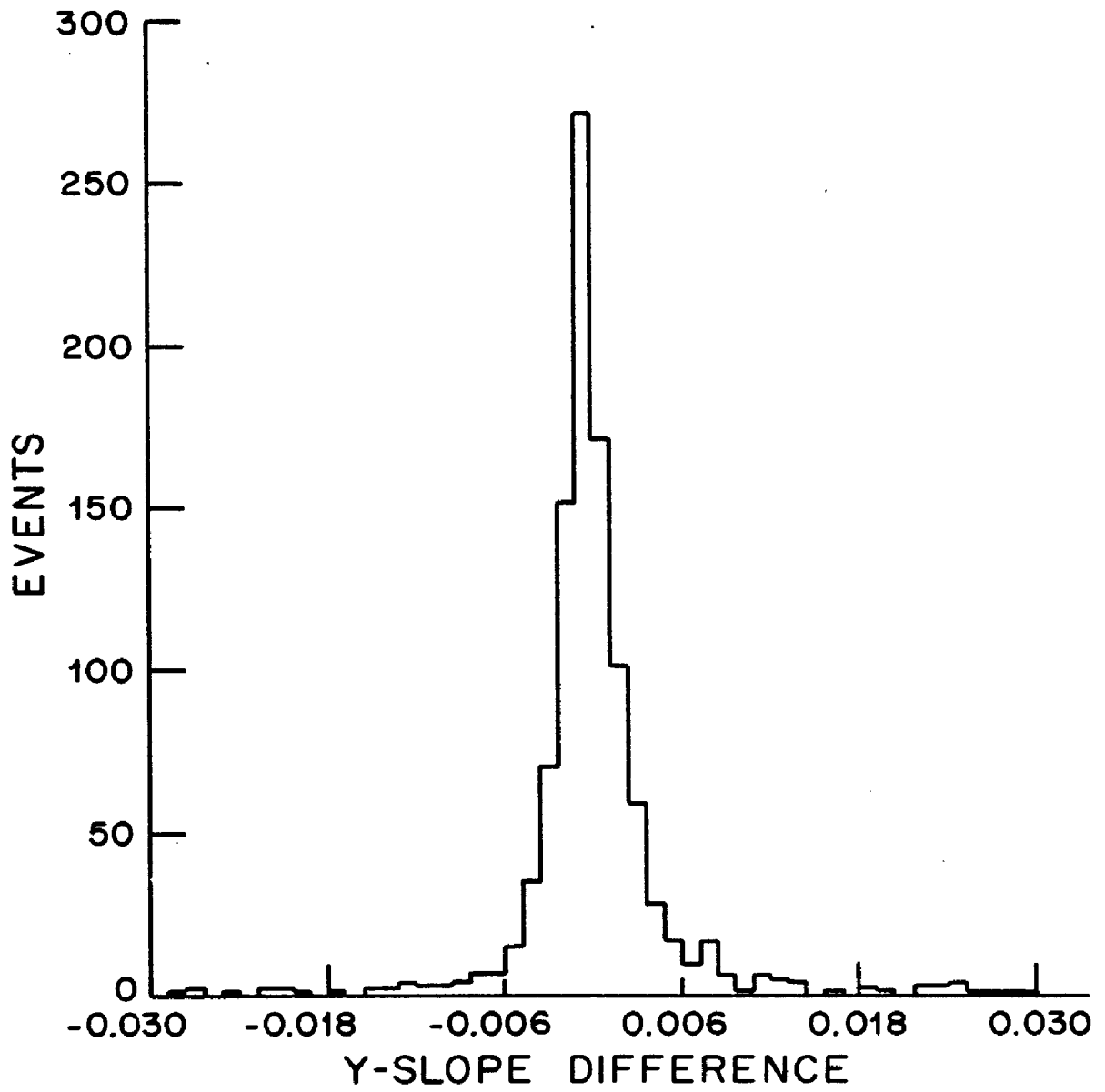


FIGURE 3-3. HISTOGRAM OF DIFFERENCE BETWEEN Y-SLOPES OF UPSTREAM AND DOWNSTREAM TRACKS.

linking the maximum number of tracks. For example, if downstream track (A) satisfied the linking requirements with upstream x-tracks (1) and (2), and downstream track (B) did with (1) only, then the result would have been, (A) linked to (2) and (B) linked to (1).

E. Momentum Calculator

After the track linking was completed the muon momentum was computed for each linked track. From a beam trigger run the momentum resolution (σ) was measured to be 12.8 GeV/c at 222 GeV/c, which is consistent with chamber measurement errors. If the spread is due only to measurement error, this gives a 1.3 percent resolution at 50 GeV/c.

Since the momentum was measured downstream of the iron absorber, it was necessary to correct for energy loss in the absorber. We made a momentum dependent correction using a simple fit to calculations made by Theriot²⁷, which included the effects of collision losses, pair production, bremsstrahlung, and nuclear interactions.

F. Reconstruction Efficiency

As a check, two independent reconstruction programs were written and were compared event by event before the primary analysis was done. Reconstruction inefficiencies were found in both of the programs. These were then corrected and the comparison was made again. After the

programs were tuned up in this way, each showed a two percent inefficiency in reconstruction when using events reconstructed by the other program as a sample. An additional two percent of the events were found to have significant differences in the reconstructed tracks. Although this gives only an upper limit on the reconstruction efficiency, since there could be correlations between the two programs, it indicates the reconstruction programs had a high efficiency.

For parts of the run the readout on the two by six meter chambers was not functioning. Reconstruction was then done downstream with only the two by four meter chambers. This caused a five percent inefficiency in reconstruction due to chamber inefficiency. We measured this by comparing the number of events reconstructed with and without the 2X6 meter chambers using a sample of data where they were working properly.

To check for problems with some parts of the data, the number of good events per incident beam particle was plotted as a function of run number (figure 3-4). This quantity was constant, aside from the obvious dependence on target thickness, to within ten percent. This of course also checks for trigger efficiency fluctuations.

From the above checks on the reconstruction we found

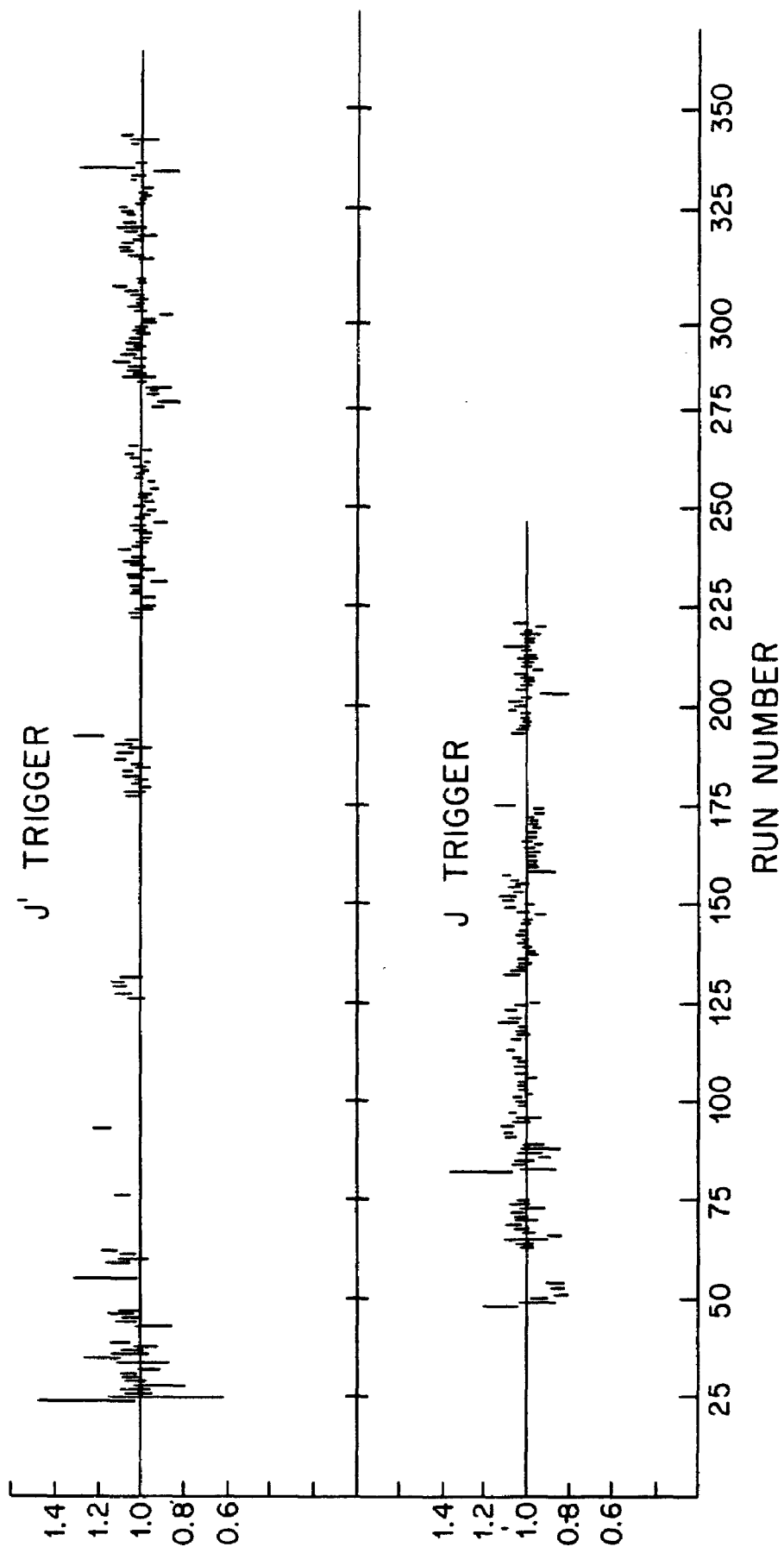


FIGURE 3-4. Plot of the number of good events satisfying the J trigger requirement divided by the number of incident beam particles versus run number. The results have been normalized so that the average is one and the obvious dependence on target thickness has been removed.

that there were no problems with the program or intermittent equipment problems that caused a significant inefficiency. The absolute reconstruction efficiency was measured by displaying the chamber and counter hits on a CRT and recording the number of good events missed. This could be done easily because of the large number of spark chamber planes (20) downstream of the magnet. Here we were sure to get enough sparks to see a track. By then imposing a P counter requirement the efficiency upstream, where the potential problems lie, could be measured. The efficiency measured was 85 percent (includes the 2 percent program inefficiency). The track reconstruction efficiency of the MWPC's calculated from the measured plane efficiencies was 97.8 percent per track. This gives an event efficiency of 91.2 percent since four upstream tracks were required. We expect the inefficiency to be larger than the simple number calculated from the plane efficiencies because of confusion from electromagnetic showers coming out of the iron which caused the MWPC readout to overflow in some cases.

G. Data Handling

The reconstruction took place in three steps. In the first step, the primary data tape was read, track finding was done and the derived information along with a copy of the primary data was written on a secondary tape. For each

primary tape one secondary tape was written. In the second step all two muon events were written in a compressed form on a tertiary tape. All events with more than two muons were written in the format of the secondary tape on another tape. This reduced the volume of data from 240 primary tapes to about 10 tapes. In the third step of the analysis the good data were binned, normalized and cuts were imposed. This step could be rerun many times because it used relatively little computer time.

CHAPTER IV. ANALYSIS

A. χ^2 Fit To Upstream Slopes

The largest contribution to Δm , the measurement error in the mass, was multiple scattering in the iron absorber. In order to get the best resolution possible we assumed that the μ -pair came from the center of the target along the beam direction and that both muons came from the same point. Then, the slopes upstream of the absorber were calculated from the positions and slopes downstream of the absorber by minimizing a χ^2 .

The joint probability distribution²⁸ for the multiple scattering angle θ_x and the multiple scattering displacement x is

$$P(x, \theta_x) = e^{-\frac{4P^2 X_0}{(.021)^2} \left(\frac{\theta_x^2}{z} - \frac{3\theta_x x}{z^2} + \frac{3x^2}{z^3} \right)}$$

where z is the length of the scattering material and X_0 is the radiation length. Scattering in y is independent of that in x and the same probability distributions apply.

Since $P \propto e^{-x^2/2}$, the χ^2 could simply be written as

$$\chi^2 = \frac{8P_1^2 X_0}{(.021)^2} \left(\frac{\theta_{x_1}^2}{z} - \frac{3\theta_{x_1} x_1}{z^2} + \frac{3x_1^2}{z^3} + \frac{\theta_{y_1}^2}{z} - \frac{3\theta_{y_1} y_1}{z^2} + \frac{3y_1^2}{z^3} \right)$$

$$+ \frac{8P_2^2 X_0}{(.021)^2} \left(\frac{\theta_{x_2}^2}{z} - \frac{3\theta_{x_2} x_2}{z^2} + \frac{3x_2^2}{z^3} + \frac{\theta_{y_2}^2}{z} - \frac{3\theta_{y_2} y_2}{z^2} + \frac{3y_2^2}{z^3} \right)$$

This χ^2 can be rewritten in terms of measured quantities, namely, the position of the vertex, initial slopes of the muons, slopes of the muons downstream of the absorber, and positions of the muons downstream of the absorber. By requiring a χ^2 minimum, the x-y vertex position and the initial muon slopes were computed analytically. From the momenta and from these fit slopes the event parameters m , x_F , p_{\perp} , and $\cos \theta^*$ were calculated.

After the x-y position of the vertex has been calculated by the χ^2 method, the calculation of the fit slopes with the χ^2 is equivalent to an easily visualized method. If the tracks downstream of the absorber are extrapolated to a "magic" plane in the absorber and their intersections with that plane are connected to the vertex with straight lines, the slopes of these lines are the same as the fit slopes (see figure 4-1).

In some cases muon pairs produced in the shield or uncorrelated muons were reconstructed, with the result that an incorrect mass was computed from the fit slopes. For example, muon pairs which come from the shield have a "fit mass" which is about half their actual mass. To remove μ -pairs that did not come from the target, cuts were imposed. First a cut was made on the χ^2 discussed above. The cut was mass dependent since high mass events which do

"Magic" Plane
$$Z_F = \left(1 - \frac{3 \frac{Z_T}{Z_A} - 2}{6 \left(\frac{Z_T}{Z_A}\right)^2 - 3 \frac{Z_T}{Z_A}}\right) Z_T$$

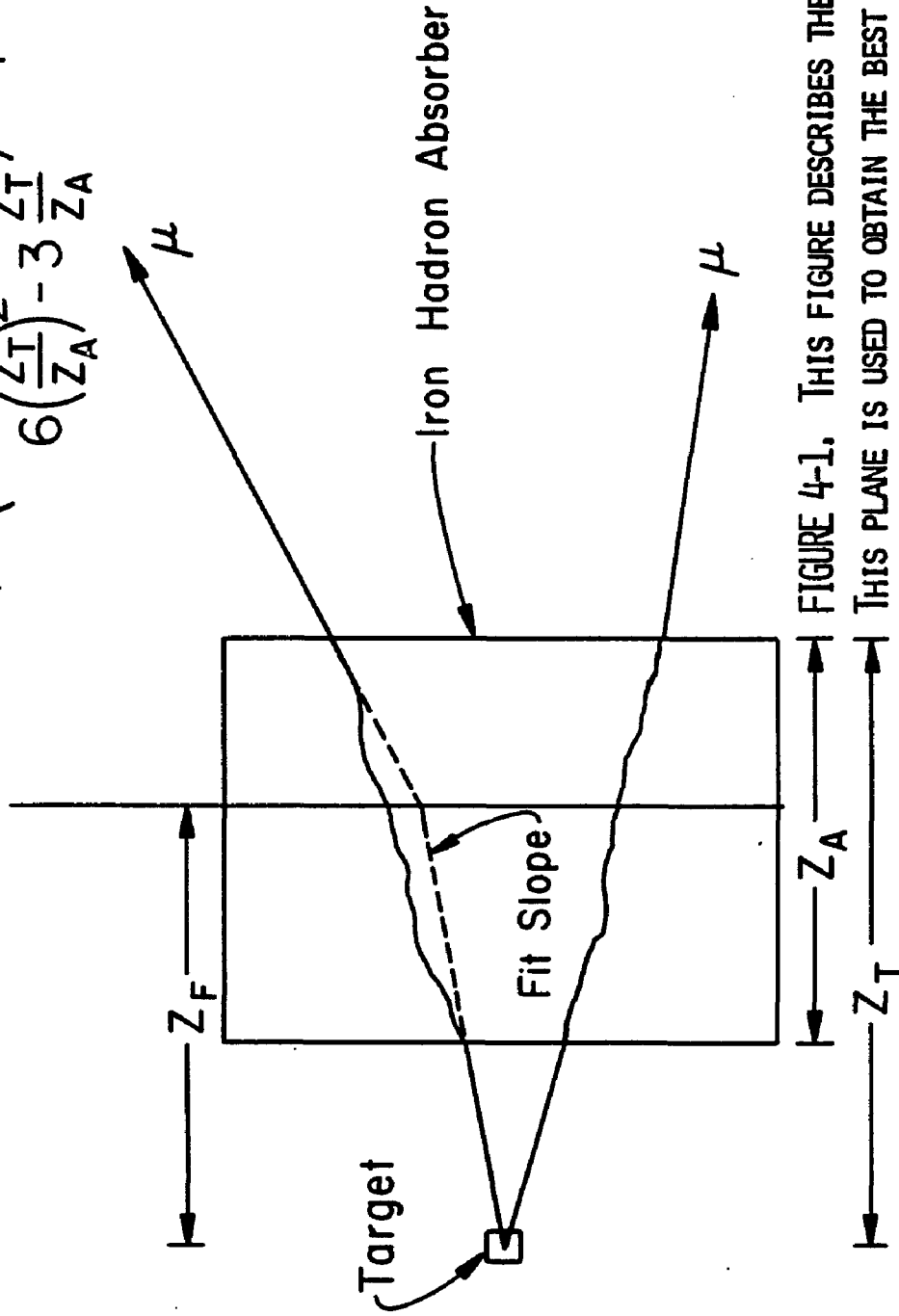


FIGURE 4-1. THIS FIGURE DESCRIBES THE "MAGIC" PLANE. THIS PLANE IS USED TO OBTAIN THE BEST FIT SLOPE FOR A TRACK WHICH IS ASSUMED TO COME FROM THE TARGET. MUON TRAJECTORIES ARE MEASURED IN PROPORTIONAL CHAMBERS AFTER LEAVING THE ABSORBER. THESE TRAJECTORIES ARE EXTRAPOLATED BACK TO THE MAGIC PLANE. THEIR INTERSECTIONS WITH THAT PLANE ARE CONNECTED TO A POINT IN THE TARGET WITH STRAIGHT LINES. THE BEST FIT SLOPES ARE THE SLOPES OF THE LINES.

not come from the target have very large χ^2 's. Events were cut for $\chi^2 > 6 + 2m$ with m in GeV/c^2 . Figures 4-2, 4-3 and 4-4 are scatter plots of the χ^2 for an event with the assumption that it came from the target vs. the χ^2 for the event with the assumption that it came from the absorber. In the first plot ($m < 0.525$) most of the events have low target and absorber χ^2 's. It is not possible to separate target pairs from absorber pairs in this mass region (Use of additional information from chambers upstream of the hadron absorber allows the separation to be made. See the thesis of G. G. Henry). In the second plot ($0.525 < m < 1.0$) most of the events have low target χ^2 's and are distributed uniformly over a large range of absorber χ^2 's. Here a partial separation of target and absorber could be made; however, it is apparent that almost all of the events come from the target. This is reasonable since events in this "fit mass" range which come from the absorber would have actual masses between 1.0 and 2.0 GeV/c^2 where the μ -pair production cross section is about a factor of seven lower than that in the 0.525 to 1.0 GeV/c^2 region. In the third figure ($m > 1.0$) most of the events have small target χ^2 's and large absorber χ^2 's. Here it is easy to separate target and absorber.

χ^2 ABSORBER

40
35
30
25
20
15
10
5

FIGURE 4-2. SCATTER PLOT OF TARGET χ^2 VERSUS SHIELD χ^2 FOR EVENTS IN THE MASS REGION $2 m_\mu < m_{\mu\mu} < 0.525 \text{ GeV}/c^2$.

5 10 15 20 25 30

χ^2 TARGET

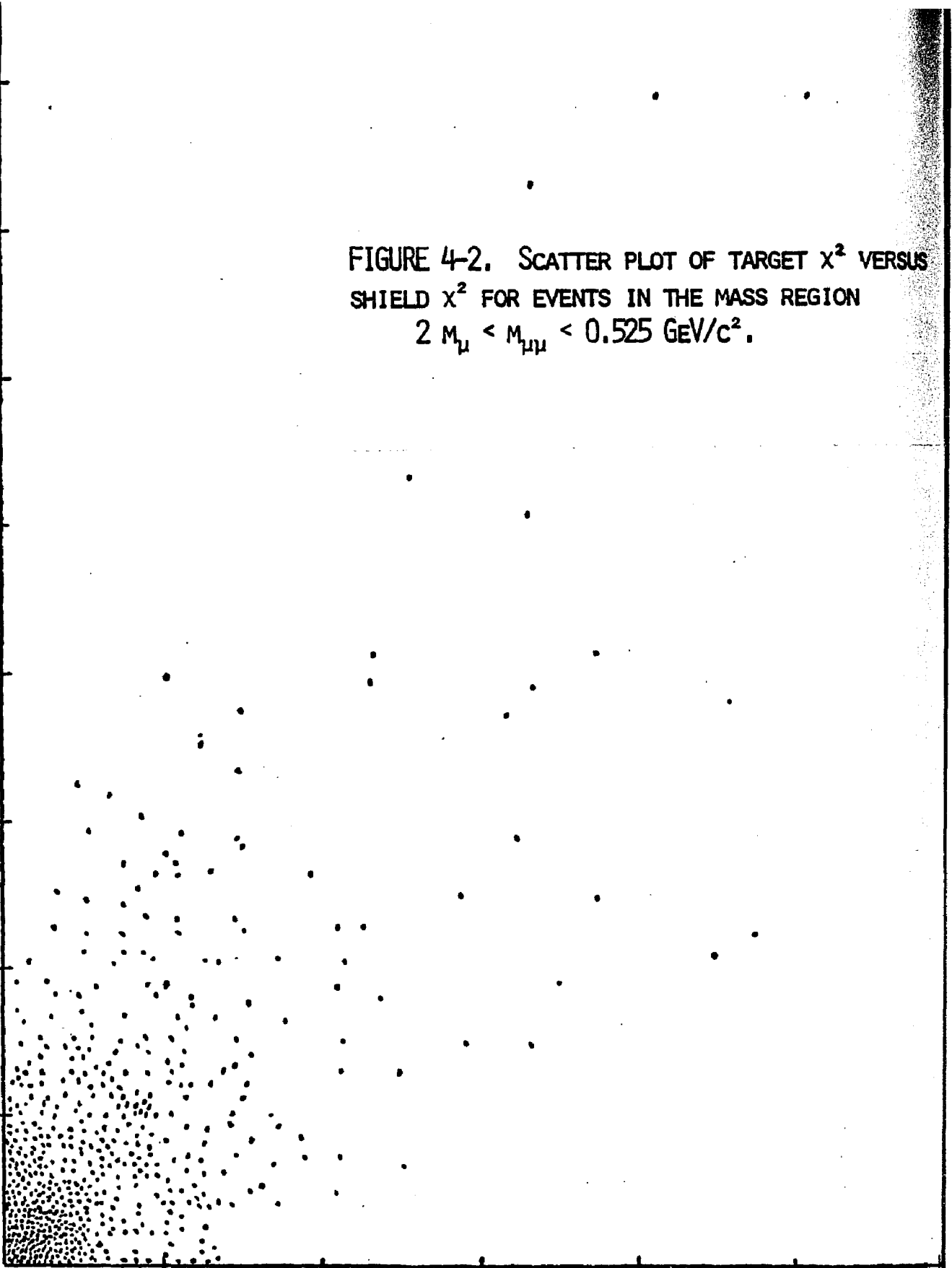
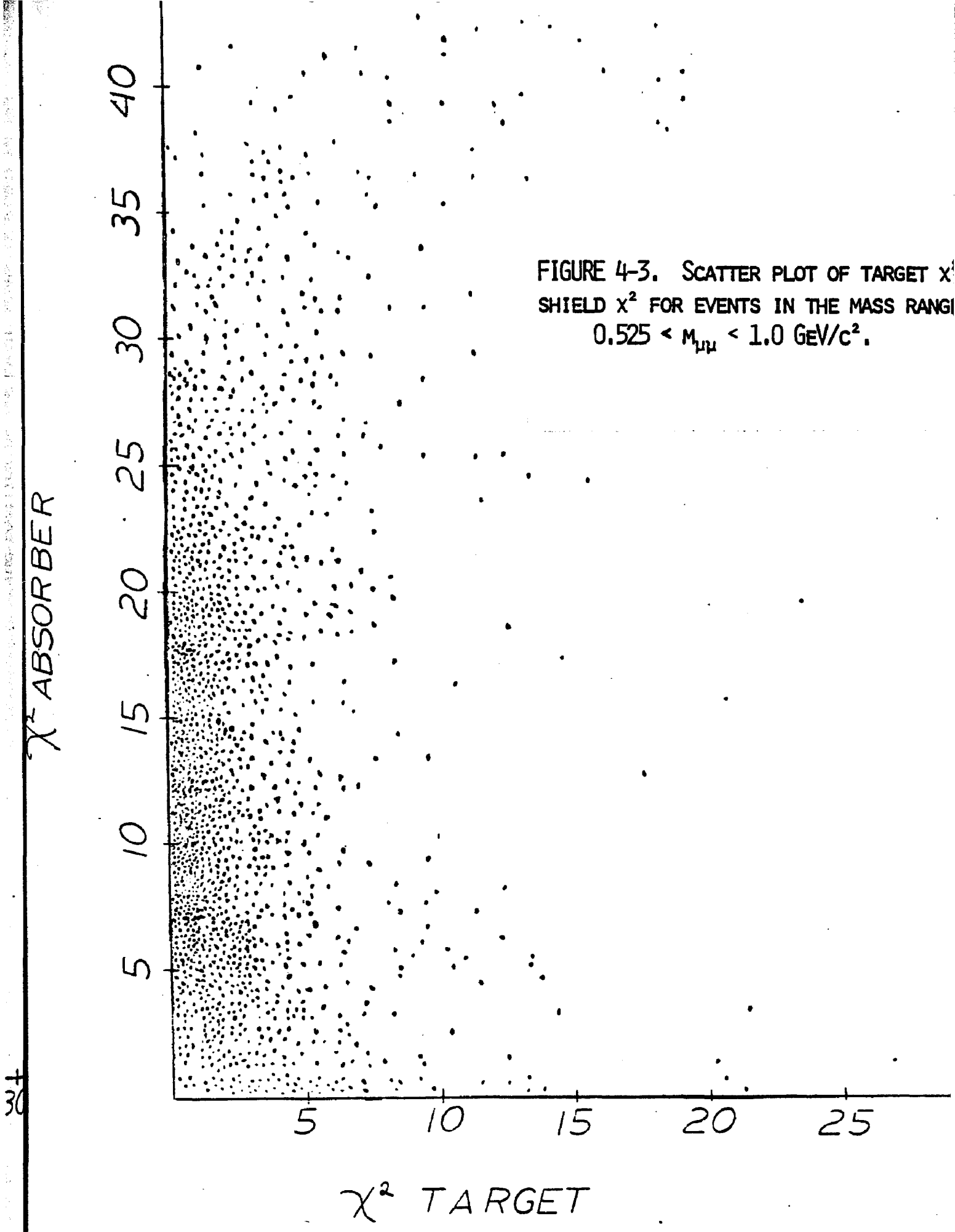


FIGURE 4-3. SCATTER PLOT OF TARGET χ^2 SHIELD χ^2 FOR EVENTS IN THE MASS RANGE $0.525 < m_{\mu\mu} < 1.0 \text{ GeV}/c^2$.



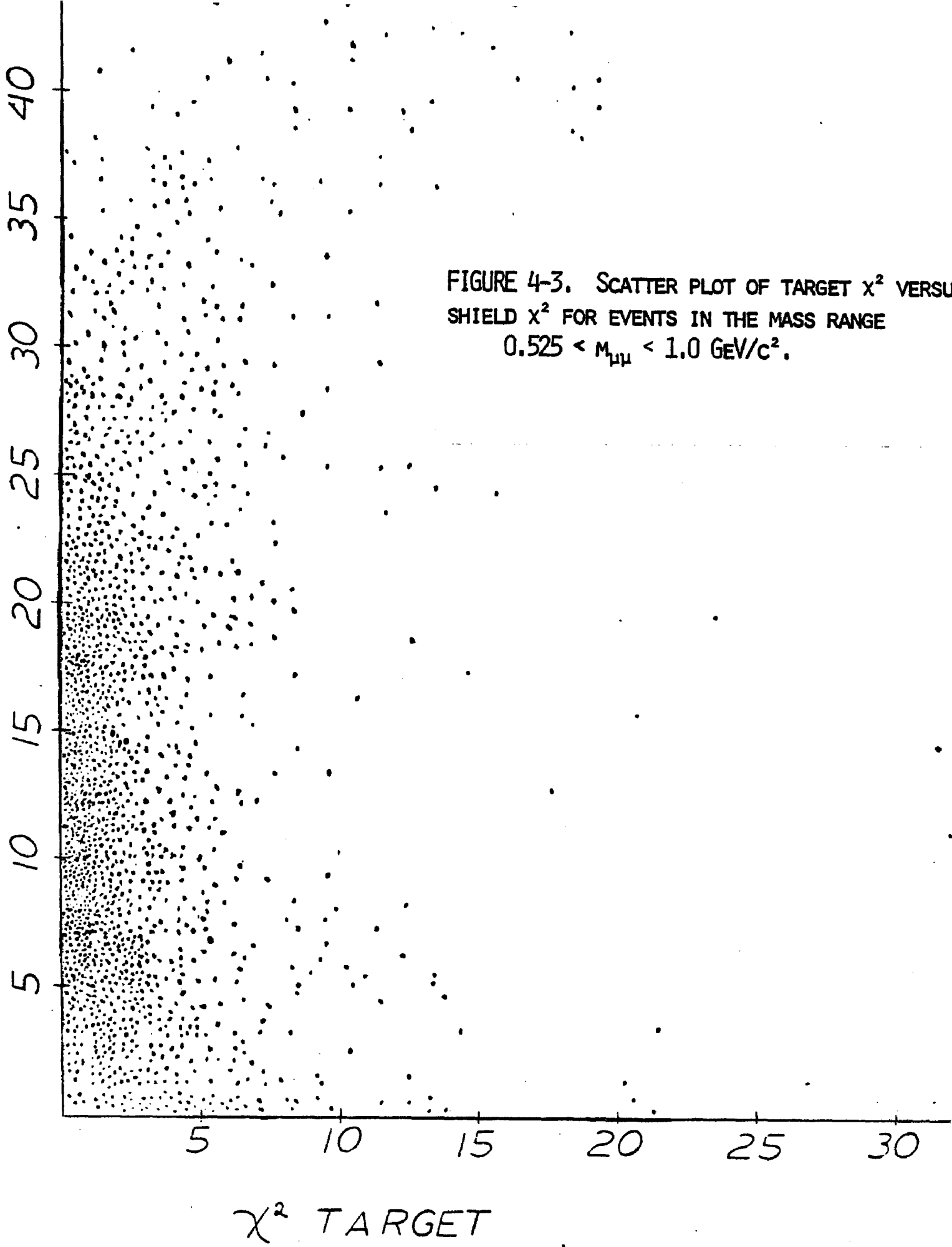


FIGURE 4-3. SCATTER PLOT OF TARGET χ^2 VERSUS SHIELD χ^2 FOR EVENTS IN THE MASS RANGE $0.525 < m_{\mu\mu} < 1.0 \text{ GeV}/c^2$.

χ^2 ABSORBER

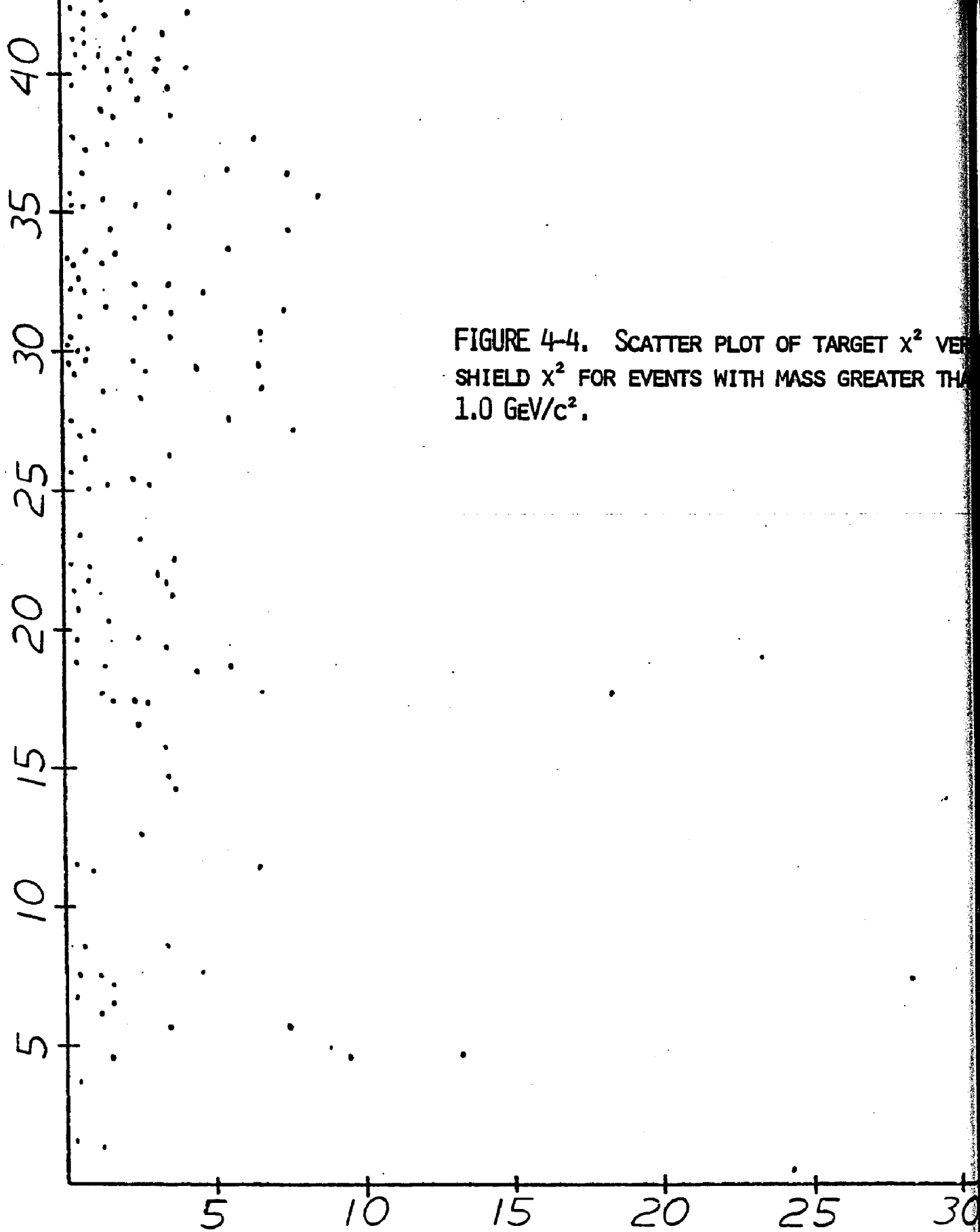


FIGURE 4-4. SCATTER PLOT OF TARGET χ^2 VERSUS SHIELD χ^2 FOR EVENTS WITH MASS GREATER THAN 1.0 GeV/c^2 .

χ^2 TARGET

Additional cuts were applied mainly to eliminate high mass pairs where one muon was from an accidental in the beam halo. This was possible because halo particles populated a very small segment of the phase space for good events. First, no muons were allowed with momentum greater than 195 GeV/c. Second, events having muons with angles from the beam less than six milliradians were cut if the muon had a momentum greater than 120 GeV/c. Finally a momentum dependent target cut was made on individual muon tracks. The projection of a 10 GeV/c muon track had to be within 15 cm of the beam in x and also within 15 cm in y at the z of the target center. The limit imposed was proportional to the inverse of the momentum (see figure 4-5).

Figure 4-6 shows a mass distribution for cut events. There is no noticeable enhancement at the J or ρ masses where we see strong peaks in good events. This indicates that very few μ -pairs from the target were cut (I estimate less than one percent).

B. Normalization and Beam Particle Identification

Beam particle identification was accomplished by using the three beam Cerenkov counters C_2 , C_3 and C_4 (see chapter II section C). If two or more Cerenkov latches were set, the beam particle was said to be a pion. If zero or one were set, the beam particle was said to be a proton. For

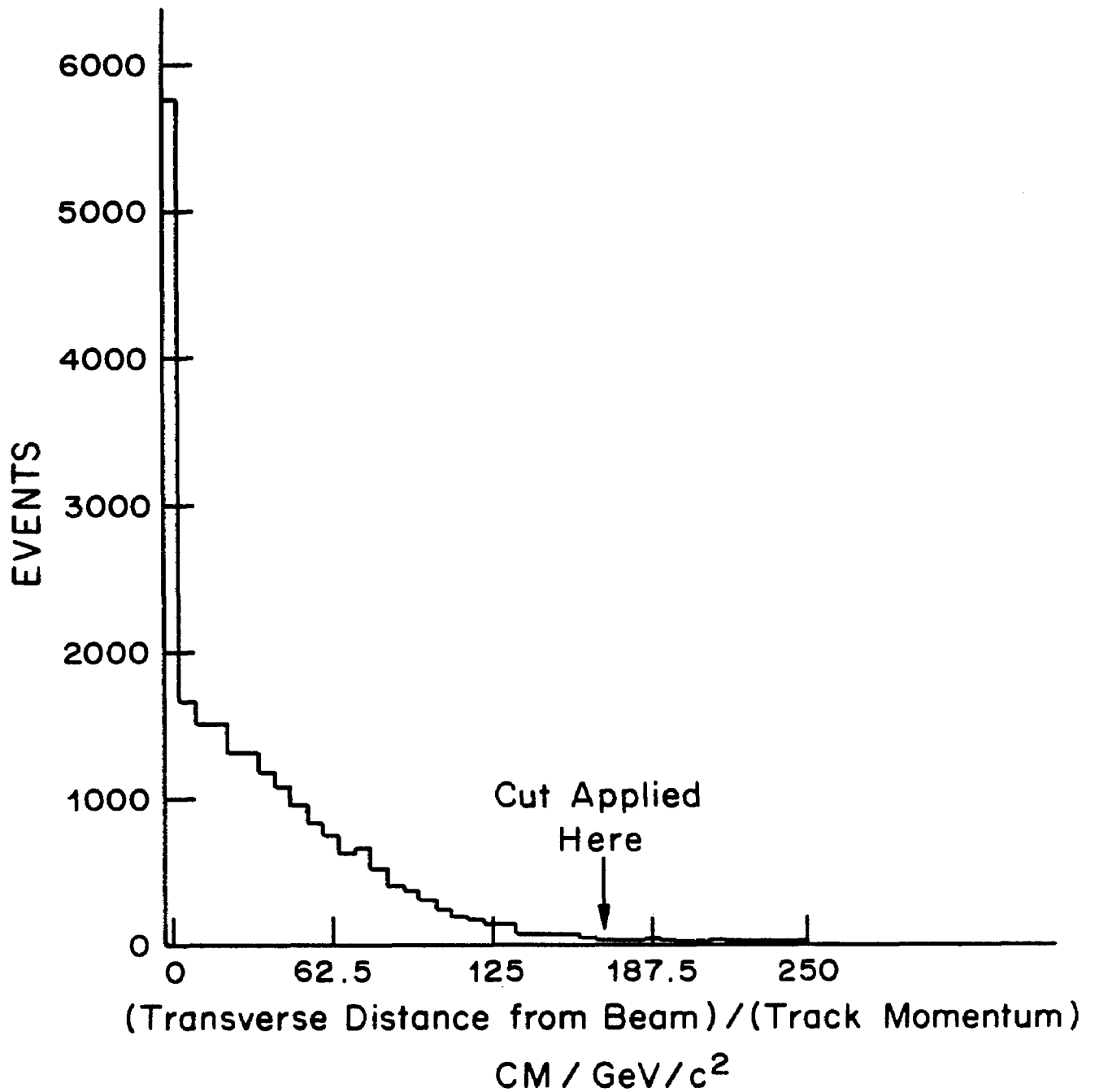


FIGURE 4-5. HISTOGRAM OF EVENTS VERSUS A TRACK PARAMETER USED TO CUT OUT TRACKS WHICH DID NOT COME FROM THE TARGET. THE EXCESS IN THE FIRST BIN IS DUE TO TRACKS WHICH APPEAR TO COME FROM A POINT WITHIN THE BEAM SPOT.

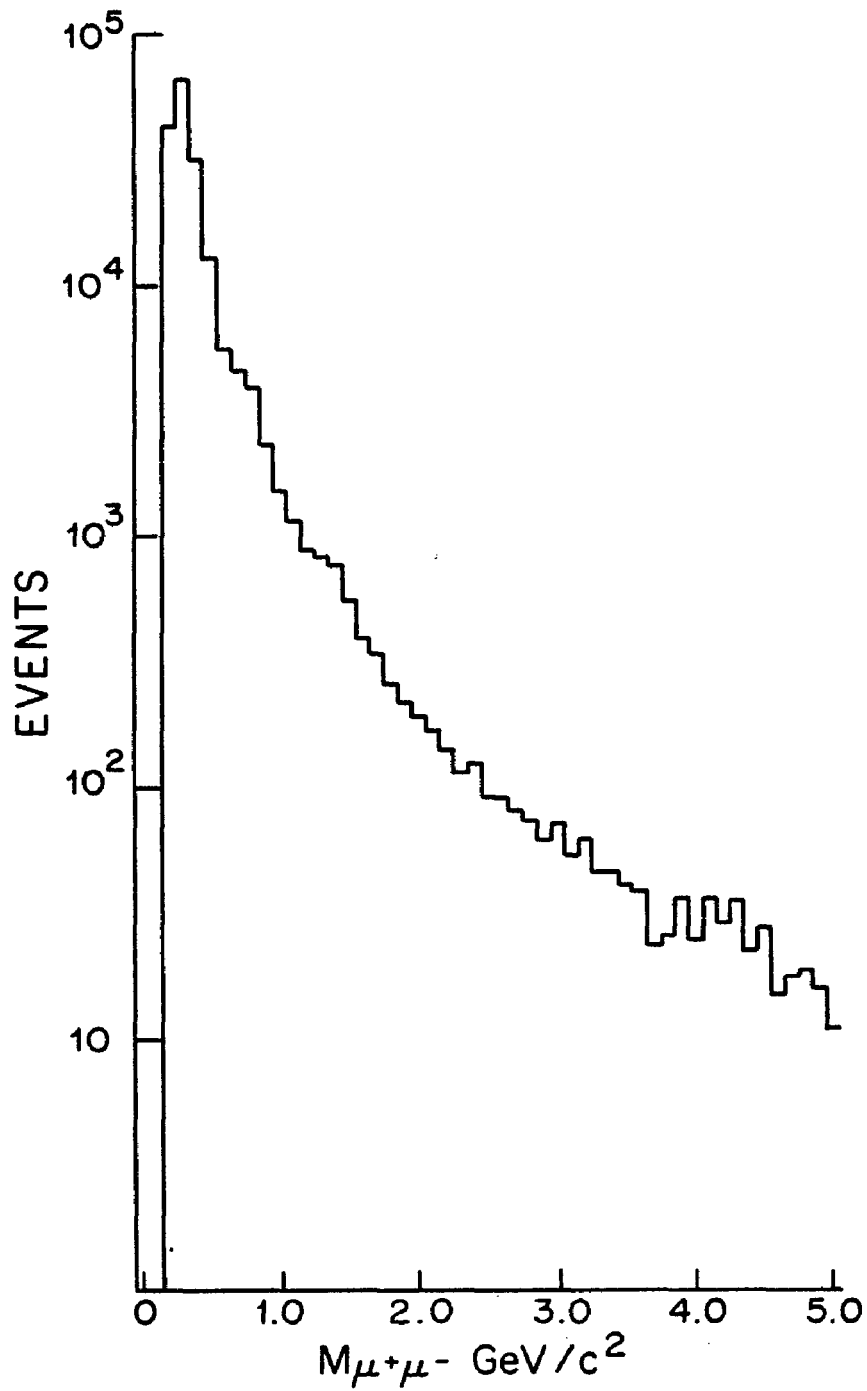


FIGURE 4-6. HISTOGRAM OF CUT EVENTS VERSUS MASS.

the negative beam running, all particles were assumed to be π^- 's. For a typical run, the efficiencies and accidental probabilities are given below.

<u>COUNTER</u>	<u>EFFICIENCY</u>	<u>ACCIDENTAL PROBABILITY</u>
C ₂	.921	.013
C ₃	.896	.010
C ₄	.992	.006

The probability of misidentifying a pion as a proton is then 0.0041 and the probability of misidentifying a proton as a pion is 0.00027. These probabilities are so small that they may be neglected.

The beam normalization was done by using the CAMAC scalars. The coincidences B, B * C₂, B * C₃, B * C₄, B * C₂ * C₃, B * C₂ * C₄, B * C₃ * C₄ and B * C₂ * C₃ * C₄ were scaled, where B is defined in chapter II, section I. From these the number of protons and the number of pions could be calculated:

$$N_{\pi} = (B * C_2 * C_3) + (B * C_2 * C_4) + (B * C_3 * C_4) - 2(B * C_2 * C_3 * C_4)$$

$$N_p = B - N_{\pi}$$

The efficiencies could also be computed:

$$\epsilon_{c_4} = \frac{B \cdot C_2 \cdot C_3 \cdot C_4}{B \cdot C_2 \cdot C_3}, \text{ etc.}$$

Also scaled were, $B * C_2$ (delayed), $B * C_3$ (delayed) and $B * C_4$ (delayed), where the delayed signal is many RF buckets out of time from the B signal. From these the accidental probabilities of the Cerenkov counters could be calculated:

$$\text{Accidental } C_4 = \frac{(B \cdot C_4)_{\text{delayed}}}{B}, \text{ etc.}$$

Well understood corrections were made to this normalization for a few runs due to malfunctions in the electronics. After making these corrections the fraction of pions in the beam held constant throughout the run.

Target thicknesses and densities were measured. The following table summarizes the relevant normalization data.

NORMALIZATION DATA

Target Material	C	C	C	Sn
Length (cm)	7.46	12.54	13.97	5.08
Density	2.188	2.188	2.188	7.31
Exposure J' Trigger in Units of 10^{10} Particles				
Protons	1.092	1.712	.4542	.1641
π^+	.2296	0.	909719	903319
π^-	0.	1.047	0.	0.
Exposure J Trigger in Units of 10^{10} Particles				
Protons	5.035	.1198	1.037	1.961
π^+	.9864	0.	.2066	.4159
π^-	0.	0.	0.	0.

The following table summarizes the normalization results.

<u>NORMALIZATION RESULTS</u>				
target	C (7.46)	C (12.54)	C (13.97)	Sn (5.08)
Proton α	.927	.882	.870	.909
Pion α	.894	.830	.813	.880
Sensitivity J' Trigger in nanobarns/nucleus/event				
Proton	.1250	.0511	.1765	3.677
π^+	.5735	.6872	.7707	17.60
π^-		.7863		
Sensitivity J Trigger in nanobarns/nucleus/event				
Proton	.02712		.07731	.3977
π^+	.1335		.3626	1.404
π^-				

The rows labeled α give the coefficients used to correct for beam attenuation in the target.

C. The J Trigger

For data which were taken with the J trigger requirement (chapter II, section K), it was necessary to impose a software J requirement since electromagnetic showers or other spurious hits could trigger the apparatus on μ -pairs that would not satisfy the J requirement. During a large fraction of the run, the J counter latches

had a slight inefficiency. Therefore the only requirement imposed in the analysis was that the tracks of the μ -pair in the 1X1 meter proportional chambers intersect a legal combination of J counters.

From the portion of the run in which the J latches were working optimally, the J counter positions and efficiencies were checked. As an additional check, the same software J requirement was imposed on data taken with the J' trigger. The ratio of good events to incident beam particles was plotted versus run number (figure 3-4). No systematic difference between J and J' triggers was noticeable. This shows that there was no significant trigger inefficiency.

D. Backgrounds

The most common background is from μ -pairs produced in the shield. These trigger the apparatus in essentially the same way as events from the target and appear at about half their actual mass. This background is eliminated by the χ^2 and vertex cuts for masses greater than about 1 GeV/c².

Other backgrounds were approximately measured in the like charge muon pair data ($\mu^+\mu^-$ or $\mu^-\mu^-$). These backgrounds were removed by subtracting the like charged events from the oppositely charged events. The chief backgrounds in this category are muonic decays of two

hadrons produced in the target and a single hadron decay accompanied by a halo muon. Most events involving halo muons are vetoed either by the veto jaws or by the pulse height requirement in T_4 . Due to two particle correlations, the double decay probability was slightly lower for like charged pairs than for those oppositely charged. For mass greater than $1.0 \text{ GeV}/c^2$ these correlations are small²⁹.

A like charge mass spectrum is shown in figure 4-7 along with the opposite charge mass spectrum for the same data. For mass greater than $2.0 \text{ GeV}/c^2$, the number of like charge events is very small.

E. The Monte Carlo Program

An extensive Monte Carlo calculation was done to determine the acceptance of the spectrometer. This Monte Carlo included multiple scattering, energy loss and energy loss fluctuations in the material. It took into account the detailed geometry of the spectrometer and required that accepted events satisfy the trigger. The calculation was checked by comparing it with an independently written program. The two were in excellent agreement.

Using the Monte Carlo program, we made a study of resolutions and shifts in the kinematic variables measured: mass, x_F , P_{\perp} and $\cos \theta^*$. The following table gives the results of this study.

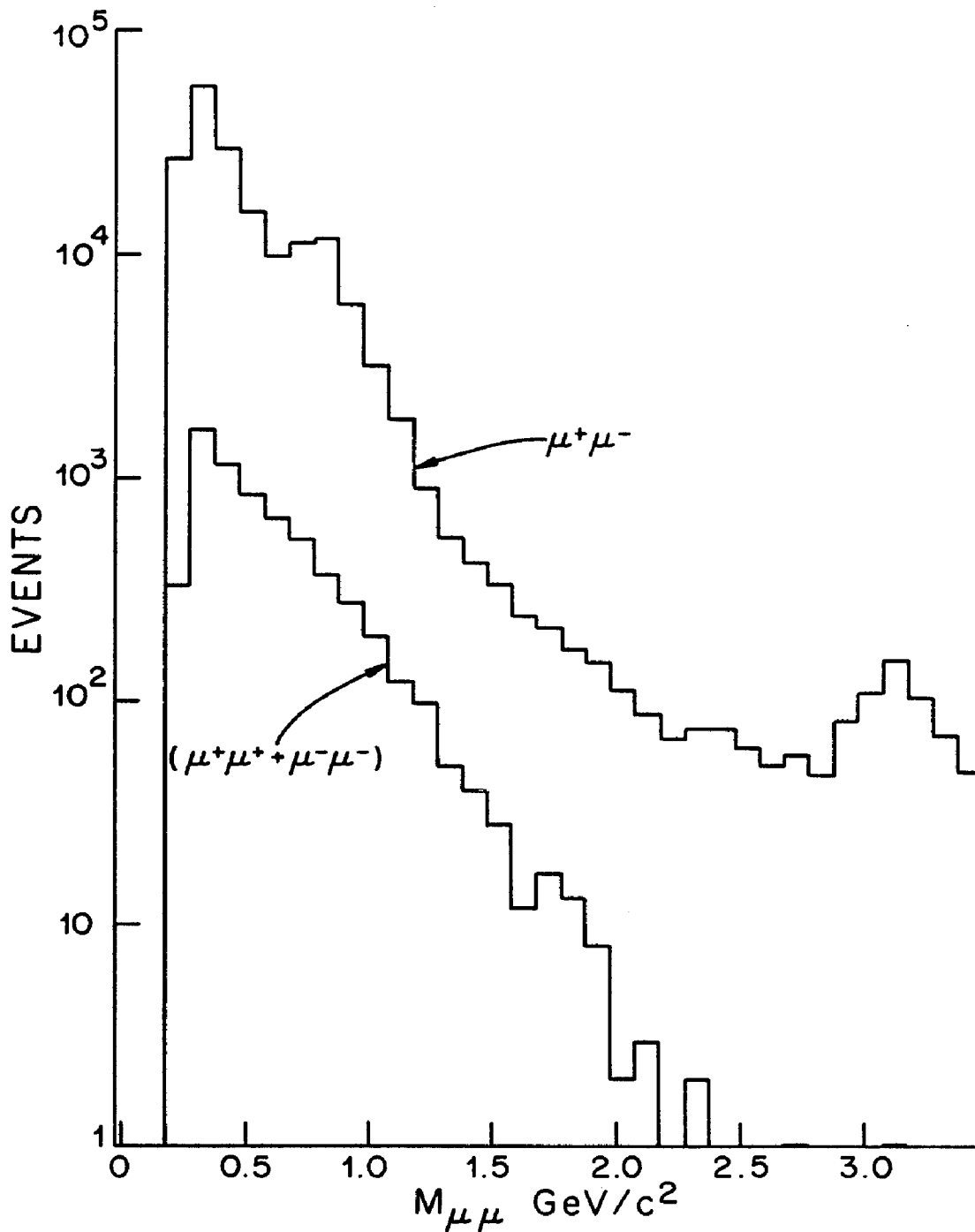


FIGURE 4-7. MASS HISTOGRAMS OF LIKE CHARGED AND OPPOSITE CHARGED MUON PAIRS. THE NUMBER OF OPPOSITELY CHARGED EVENTS FROM π AND K DECAY IS EXPECTED TO BE ROUGHLY EQUAL TO THE NUMBER OF LIKE CHARGED EVENTS.

		<u>MASS RESOLUTION (MeV/c²)</u>			
		x_F .1	.3	.5	.7
P_{\perp}	0.	176	198	243	256
	0.25	163	201	234	263
	0.5	169	198	238	251
	1.0	143	207	236	255
	1.5	182	193	245	265
	2.0	183	201	240	263

		<u>x_F RESOLUTION</u>			
		.1	.3	.5	.7
P_{\perp}	0.	.009	.021	.040	.057
	0.25	.009	.020	.038	.058
	0.5	.009	.020	.039	.056
	1.0	.009	.021	.039	.057
	1.5	.012	.018	.039	.061
	2.0	.011	.020	.039	.058

P_⊥ RESOLUTION (MeV/c)

P_{\perp} \ X_F	.1	.3	.5	.7
0.	121	153	193	243
0.25	146	194	232	275
0.5	160	226	291	333
1.0	165	244	330	416
1.5	201	256	361	446
2.0	226	287	378	473

cos e^{*} RESOLUTION

P_{\perp} \ X_F	.1	.3	.5	.7
0.	.05	.06	.08	.09
0.25	.05	.07	.08	.09
0.5	.05	.06	.08	.08
1.0	.04	.07	.08	.09
1.5	.05	.06	.08	.09
2.0	.05	.06	.08	.09

		<u>MASS SHIFT (MeV/c²)</u>			
P_{\perp}	X_F	.1	.3	.5	.7
0.		-42	-87	-101	-133
0.25		-38	-85	-101	-137
0.5		-43	-82	-101	-136
1.0		-27	-84	-112	-133
1.5		-46	-77	-114	-135
2.0		-52	-85	-110	-132

		<u>X_F-SHIFT</u>			
P_{\perp}	X_F	.1	.3	.5	.7
0.		-.001	-.005	-.012	-.019
0.25		-.001	-.005	-.011	-.019
0.5		-.001	-.005	-.012	-.019
1.0		0	-.005	-.011	-.018
1.5		-.001	-.004	-.012	-.020
2.		0	-.005	-.012	-.020

		<u>E_L SHIFT (MeV/c)</u>			
<u>P_L</u>	<u>X_F</u>	.1	.3	.5	.7
0.		207	319	453	585
0.25		59	137	247	381
0.5		27	57	121	233
1.0		-2	4	35	76
1.5		-20	-2	-15	7
2.0		-44	-31	-45	-34

		<u>CCS e[*] SHIFT</u>			
<u>P_L</u>	<u>X_F</u>	.1	.3	.5	.7
0.		.001	-.002	.002	.002
0.25		.002	-.002	0.	.001
0.5		.002	-.002	-.001	-.002
1.0		.002	-.001	.001	.003
1.5		-.001	.001	-.001	-.001
2.0		.001	0.	.001	.002

There is a mass shift of around 60 MeV/c^2 toward lower mass, due to bremsstrahlung and pair production energy loss in the absorber. In the final results, the masses have been shifted slightly upward to correct for this. The mass resolution is also inflated by these energy loss

fluctuations. Figure 5-33 shows the J line shape, generated by the Monte Carlo program, superimposed on the data. The agreement with the data is excellent. The full width at half maximum of this peak is $275 \text{ MeV}/c^2$ corresponding to a σ of $117 \text{ MeV}/c^2$.

The shifts for the x_F measurements are very small and the resolution is good. Figure 4-8 shows the spread in x_F due to Fermi motion in the target nucleus. The biggest effect is at low x_F where the resolution is about 0.05.

The shifts for the P_{\perp} measurement are rather large. They are worst at high x_F and in general shift events toward higher P_{\perp} . This causes a depletion at the low end of the P_{\perp} distributions. The uncertainties and shifts in $\cos \theta^*$ are small.

To measure the efficiency as a function of the variables m , x_F , P_{\perp} and $\cos \theta^*$, the Monte Carlo program was run for two million tries. Events were generated flat in mass over the region $0.2 < m < 4.2$, flat in P_{\perp} over the region $0 < P_{\perp} < 4$, flat in $\cos \theta^*$ over the region $-1 < \cos \theta^* < 1$ and with a probability proportional to $(1 - x_F)$ in the region $-0.1 < x_F < 0.9$. This generation populated the entire region nearly uniformly with successes. The events were weighted roughly according to their cross section.

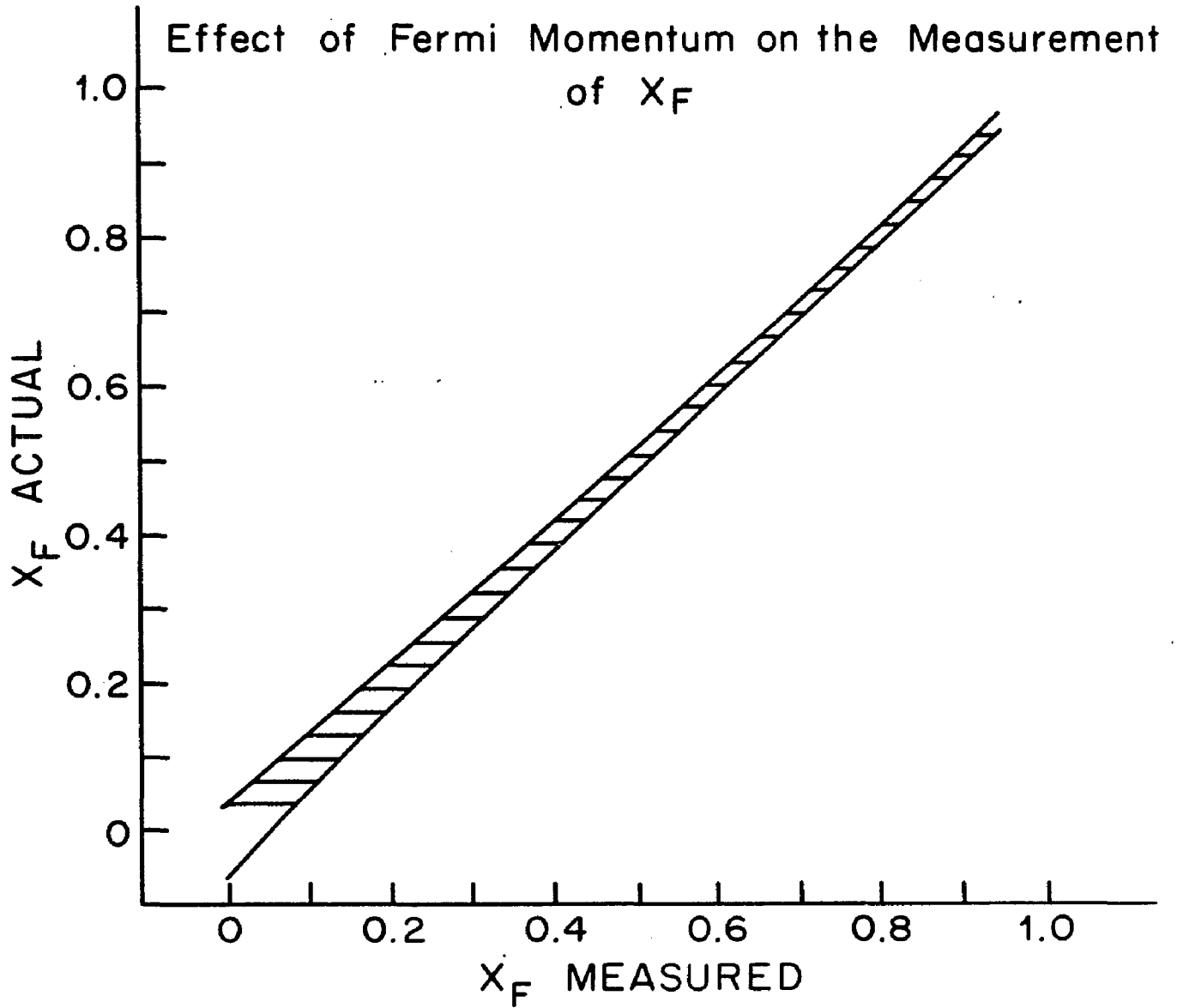


FIGURE 4-8. THIS PLOT DISPLAYS THE EFFECT OF FERMI MOTION IN THE TARGET NUCLEUS ON THE MEASUREMENT OF FEYNMANN X . IF THE MAXIMUM ALLOWED FERMI MOMENTUM IS 225 MEV/C, THE ACTUAL VALUE OF X_F CAN VARY WITHIN THE SHADED REGION FOR SOME VALUE OF MEASURED X_F .

$$\text{Weight} = (1-x_F)^{4-m} P_{\perp} e^{-(3.5-1.4 \ln(m)) P_{\perp}} e^{-4m}$$

Results were accumulated in order to calculate four types of cross sections.

1. $\frac{d^2\sigma}{dm dx_F}$; 20 Bins in x_F and 80 bins in mass.
2. $E \frac{d^3\sigma}{dm dP_{\perp}^2}$; 20 Bins in P_{\perp} and 80 bins in mass.
3. $E \frac{d^4\sigma}{dm dx_F dP_{\perp}^2}$; 20 Bins in x_F and P_{\perp} and 12 bins in mass.

The twelve mass bins are:

$$0.21 < m < 0.45$$

$$0.45 < m < 0.65$$

$$0.65 < m < 0.95$$

$$0.95 < m < 1.1$$

$$1.1 < m < 1.5$$

$$1.5 < m < 1.9$$

$$1.9 < m < 2.3$$

$$2.3 < m < 2.7$$

$$2.7 < m < 3.1$$

$$3.1 < m < 3.5$$

$$3.9 < m < 4.2$$

4. $\frac{d^3\sigma}{dm dx_F d(\cos\theta^*)}$; 20 bins in x_F and $\cos\theta^*$ and 12 bins in mass.

Events were accumulated separately for the J' and J triggers because efficiencies differed at low mass.

The Monte Carlo program was used to correct for the

shifts discussed earlier. The "efficiency" calculated was

$$E = \frac{\text{weighted successes using reconstructed quantities}}{\text{weighted tries using generated quantities}}$$

The "generated quantities" are the m , x_F , P_{\perp} and $\cos \theta^*$ values with which an event was generated. The "reconstructed quantities" are the m , x_F , P_{\perp} and $\cos \theta^*$ that would have been measured after multiple scattering, energy loss and other effects had been simulated. The generated and reconstructed variables were used to determine into which bin the success or try should be added.

In this way, shifts in the data can be removed. For example, on the average, events are shifted to higher P_{\perp} . If the efficiency definition above is used, the weighted successes at low P_{\perp} will be smaller because of the shift. This will cause the efficiency to be smaller and therefore when the cross section is calculated, the low P_{\perp} data will be raised relative to those from a simple efficiency calculation.

For the data analysis, E was split into two parts,

$$E = \epsilon D$$

where

$$\epsilon = \frac{\text{weighted successes using generated quantities}}{\text{weighted tries using generated quantities}}$$

and

$$D = \frac{\text{weighted successes using reconstructed quantities}}{\text{weighted successes using generated quantities}}$$

The "distortion" factors D were usually near one and were well behaved. Figures 4-9 through 4-12 are contour plots of the efficiency and distortion.

As seen in figures 4-13 through 4-15, the efficiency of the spectrometer is large and slowly varying in most regions. An exception is the low x_F region, where the efficiency drops off rapidly due mainly to limited MWPC size upstream of the magnet and energy loss in the hadron absorbers. Because of this rapid variation, most results are presented for x_F greater than 0.1 or 0.15.

For data taken with the J trigger requirement imposed, the efficiency varied rapidly in the low mass region. Figure 4-16 is a plot of the ratio of $d\sigma/dm$ as computed from J trigger data to that computed from J' trigger data. Above a mass of $0.5 \text{ GeV}/c^2$, the two are in good agreement. Figure 4-17 is a plot of the J versus J' ratio of $d\sigma/dx_F$ in the $0.65 < m < 0.95$ mass bin. This ratio is within errors of one except at the highest values of x_F . Therefore we conclude

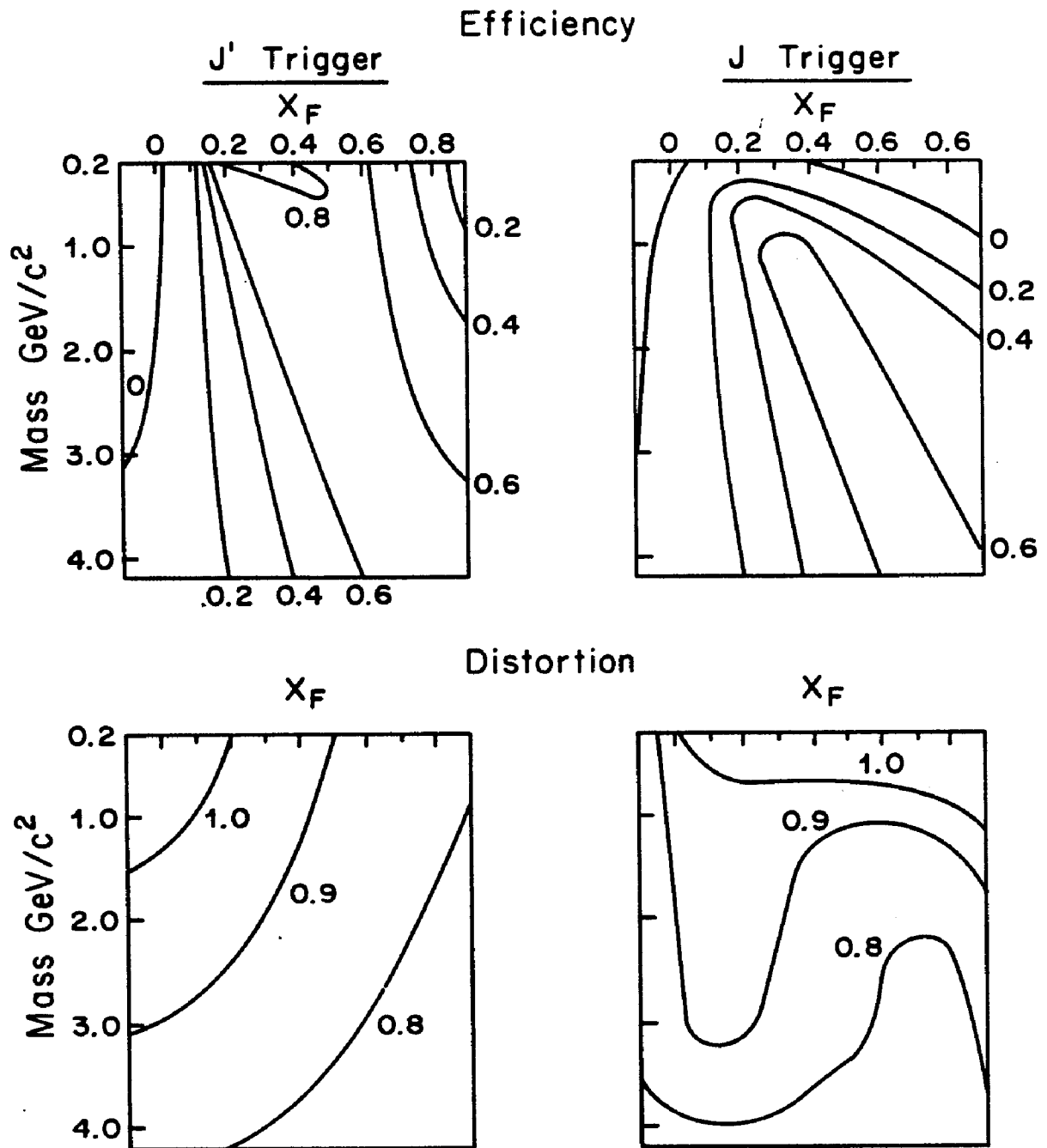


FIGURE 4-9. CONTOUR PLOTS OF EFFICIENCY AND DISTORTION USED TO CALCULATE $\frac{d^2\sigma}{dm dx_F}$ VERSUS X_F AND MASS.

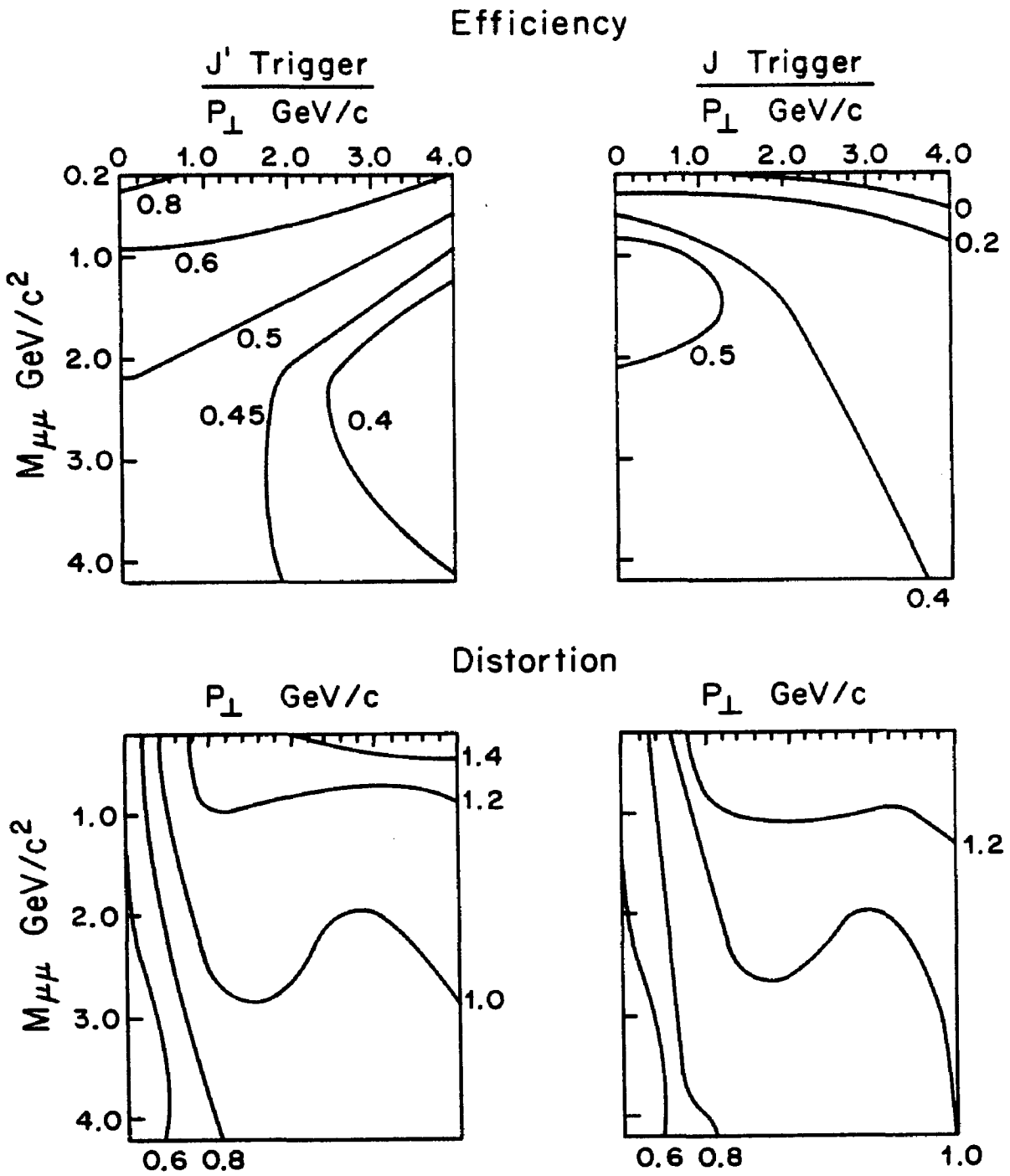


FIGURE 4-10. CONTOUR PLOTS OF EFFICIENCY AND DISTORTION VERSUS P_⊥ AND MASS, USED TO CALCULATE $E \frac{d^3\sigma}{dm dP_{\perp}^2}$

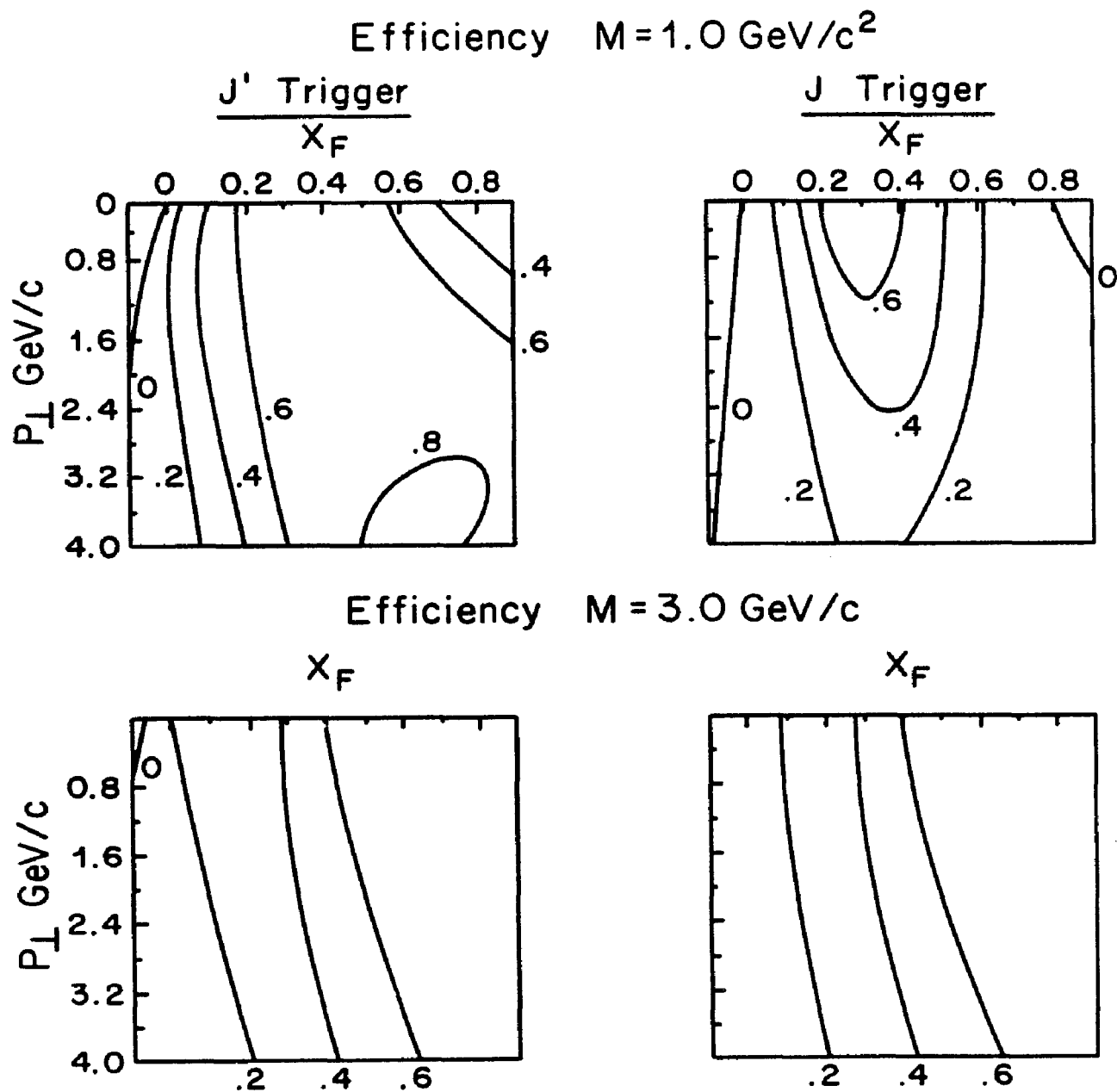


FIGURE 4-11. CONTOUR PLOTS OF EFFICIENCY AND DISTORTION
 VERSUS x_F AND P_{\perp} , USED TO CALCULATE $E \frac{d^3\sigma}{dx_F dP_{\perp}^2}$

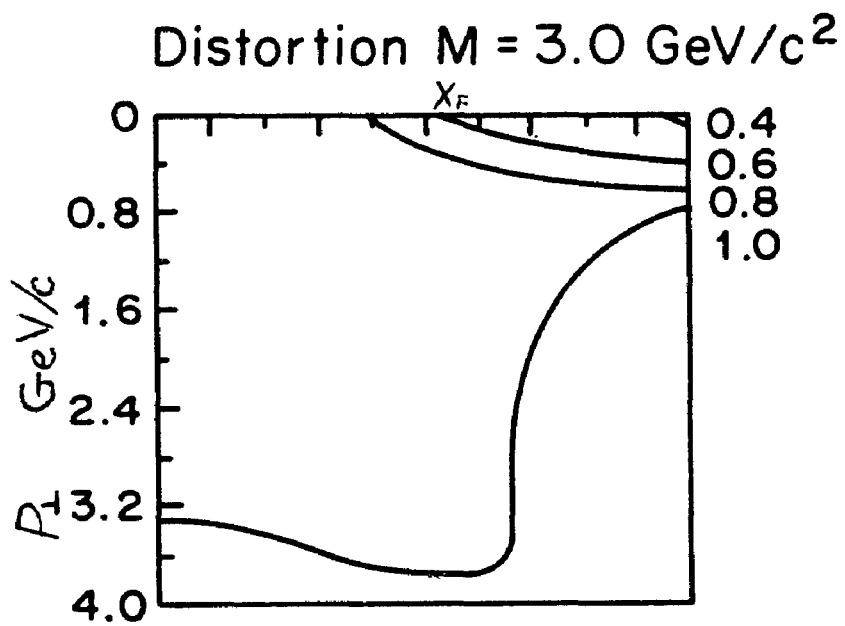
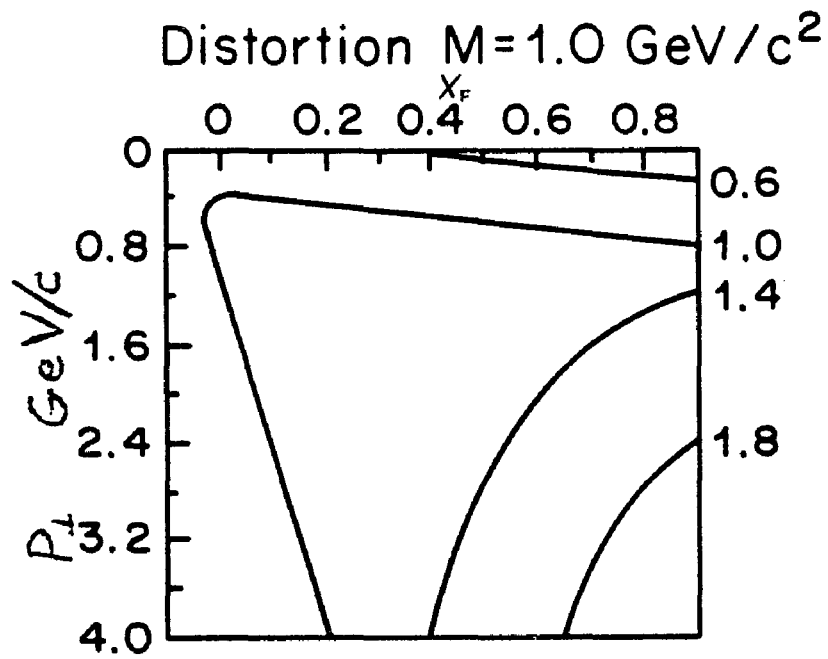


FIGURE 4-11 (CONTINUED).

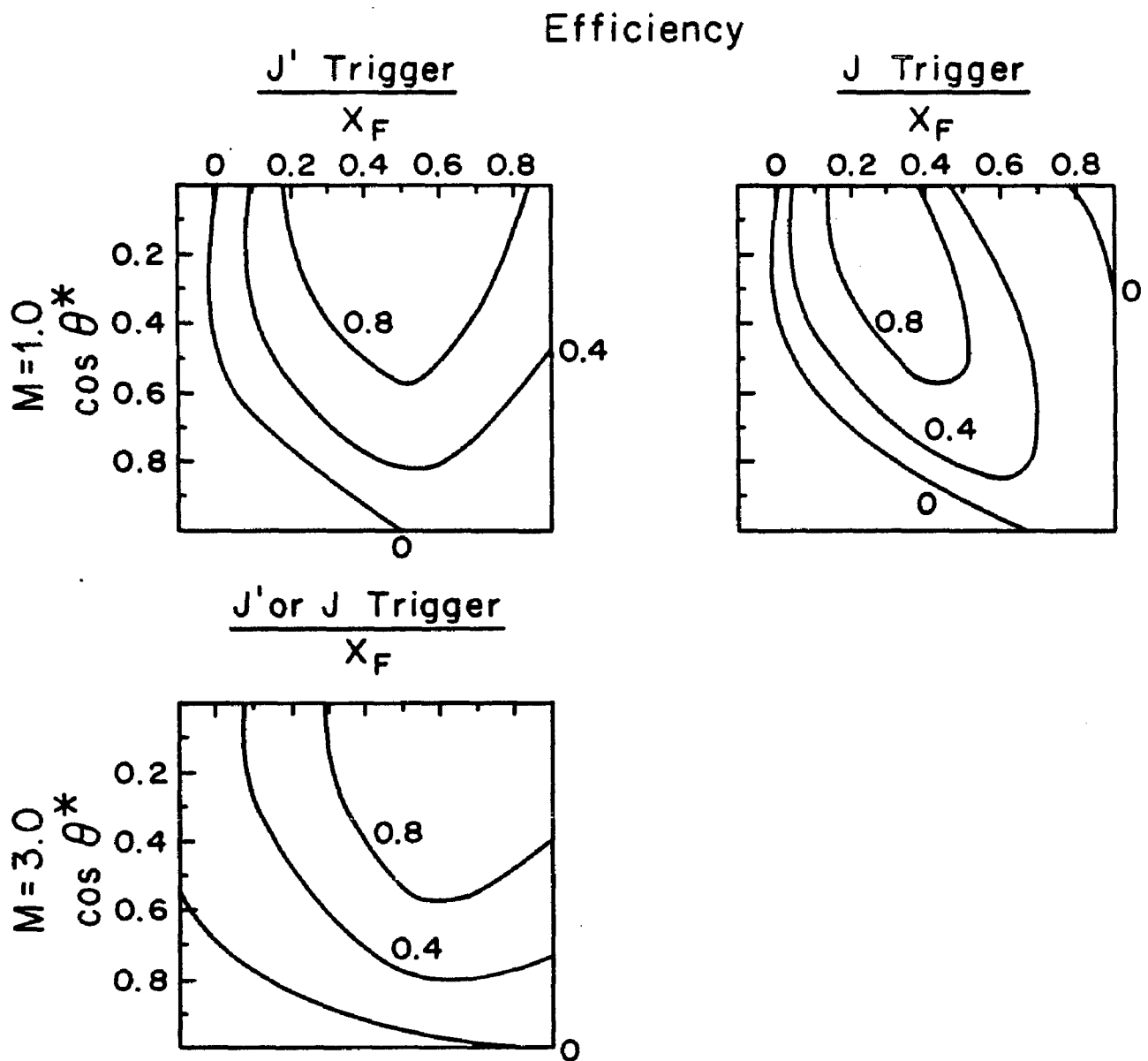


FIGURE 4-12. CONTOUR PLOTS OF EFFICIENCY AND DISTORTION AS A FUNCTION OF X_F AND $\cos \theta^*$ USED TO CALCULATE

$$E \frac{d^2\sigma}{dx_F d(\cos \theta^*)}$$

Distortion

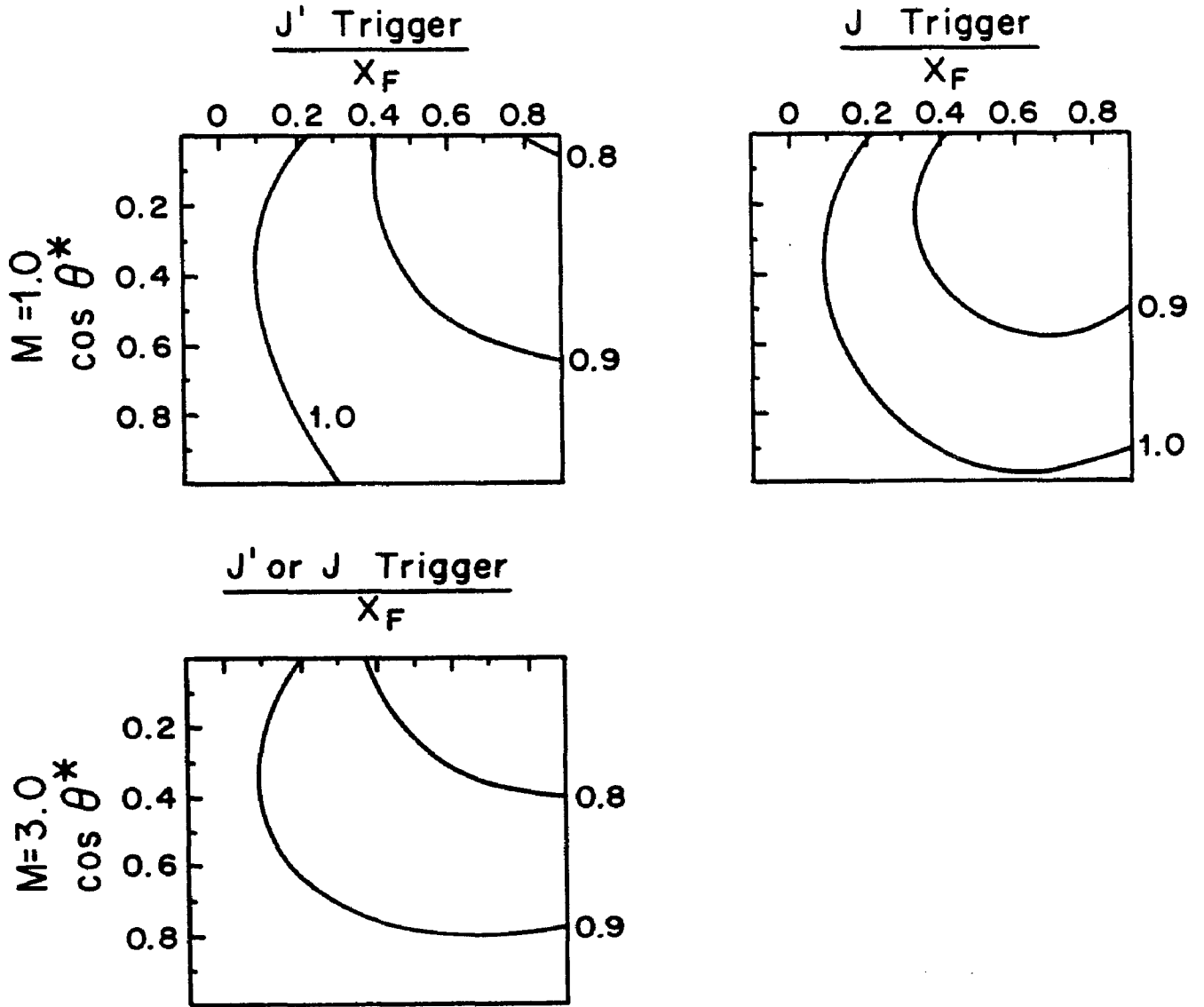


FIGURE 4-12 (CONTINUED).

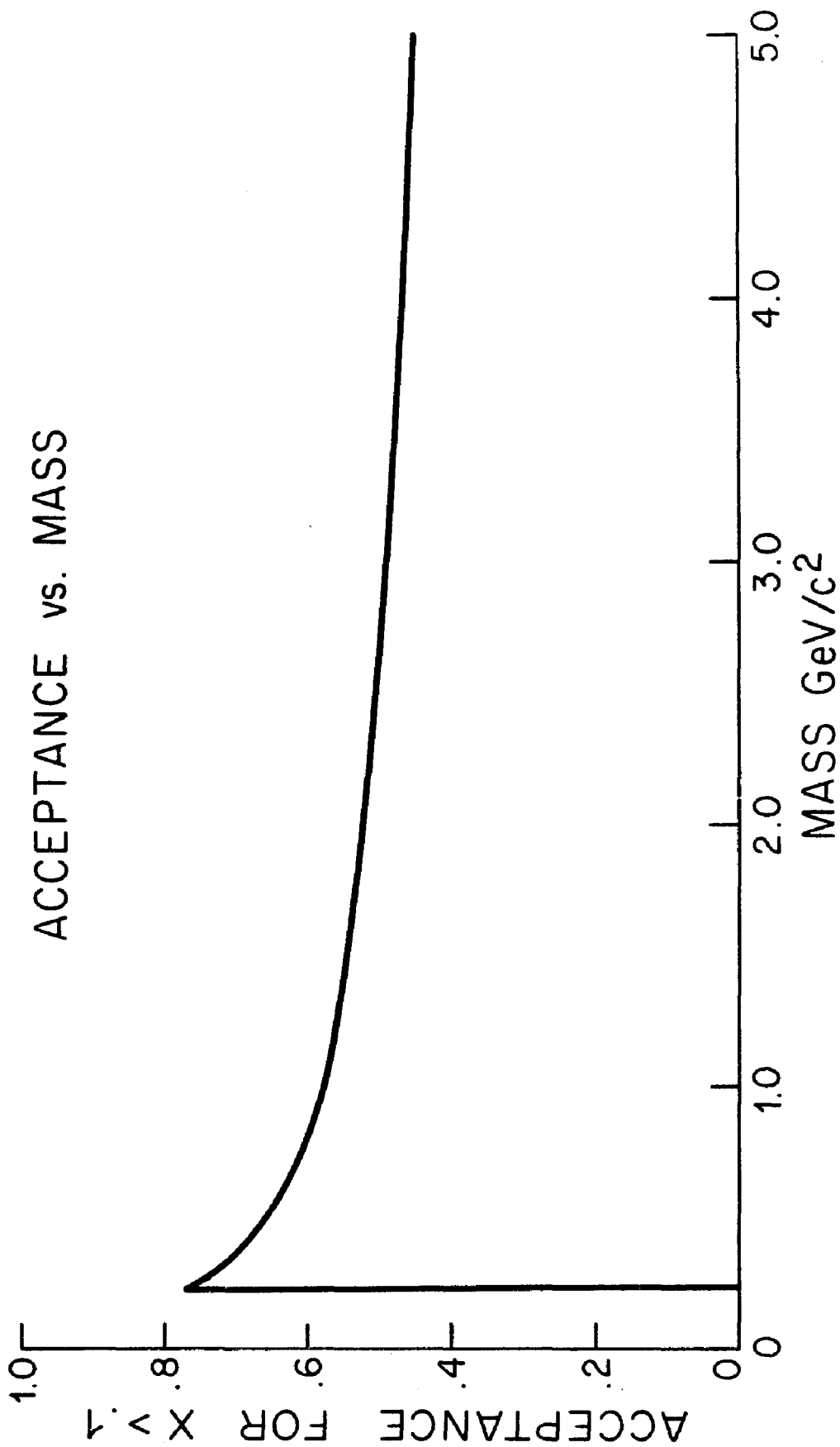


FIGURE 4-13. ACCEPTANCE AS A FUNCTION OF MASS. THE MEASURED X_F AND P_T DISTRIBUTIONS ARE ASSUMED TO CALCULATE THIS CURVE. ONLY EVENTS WITH X_F GREATER THAN 0.1 ARE CONSIDERED.

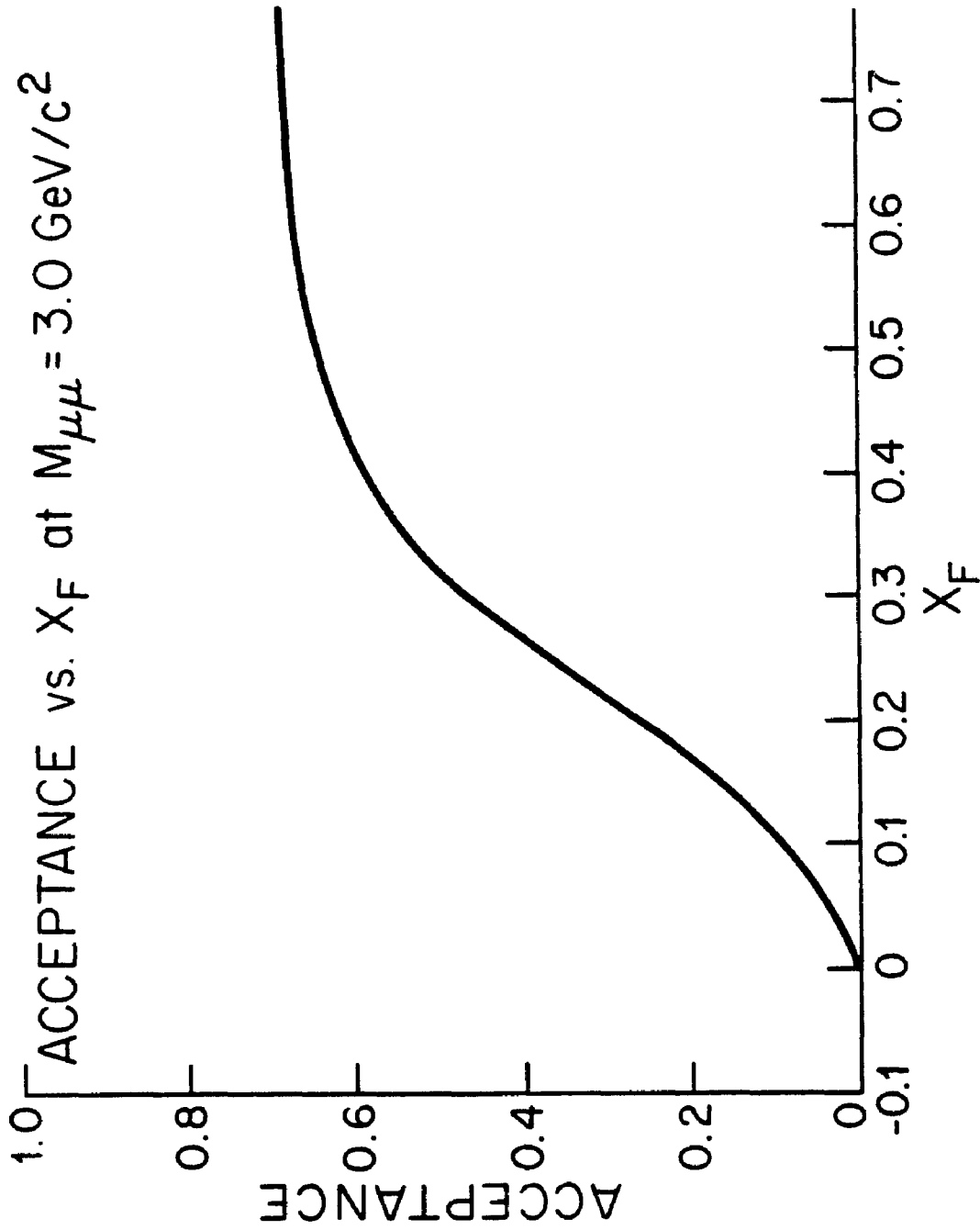


FIGURE 4-14. ACCEPTANCE AS A FUNCTION OF X_F AT A MASS OF $3.0 \text{ GeV}/c^2$. THE MEASURED P_{\perp} DISTRIBUTION IS ASSUMED TO CALCULATE THIS CURVE.

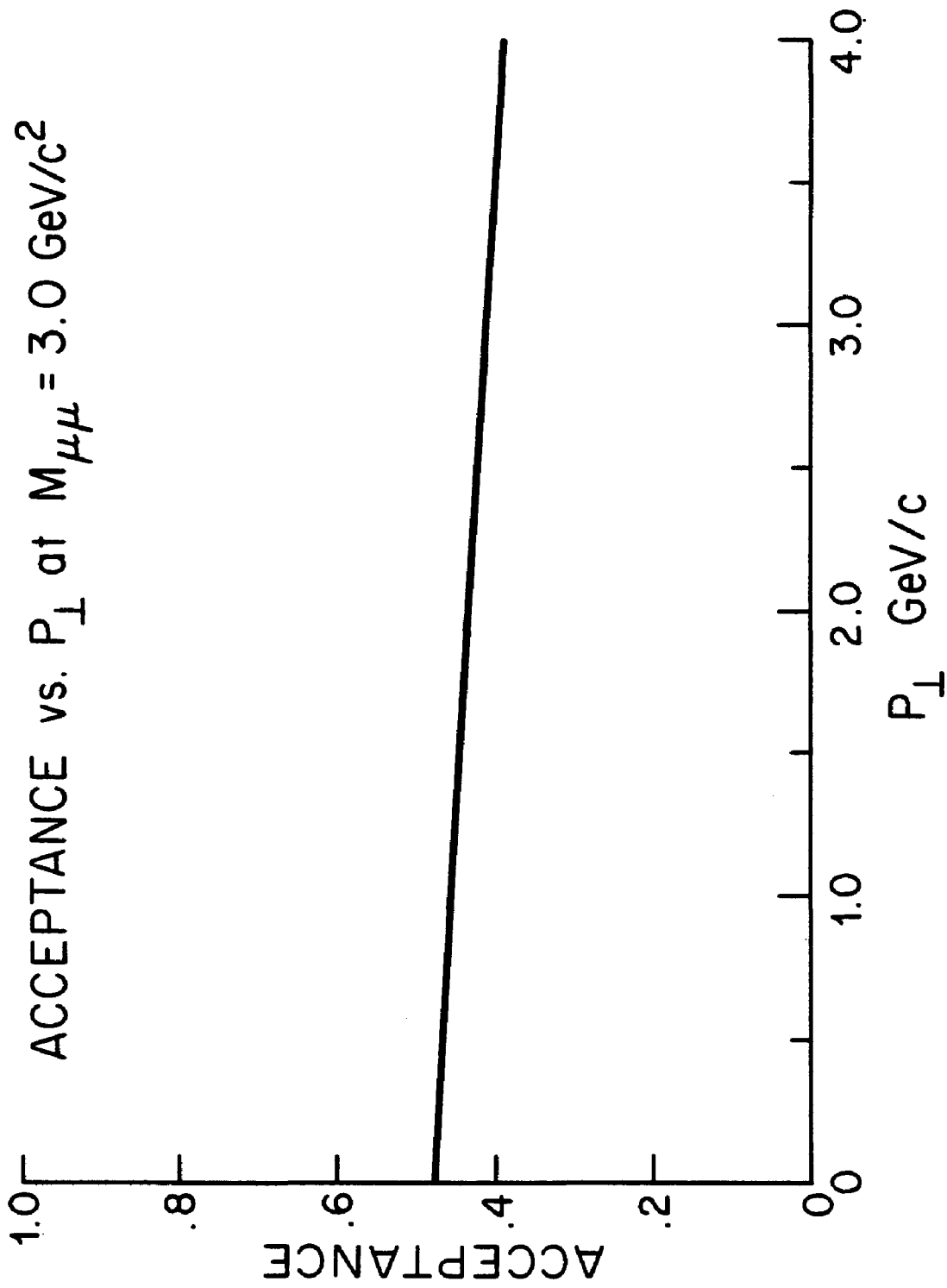


FIGURE 4-15. ACCEPTANCE AS A FUNCTION OF P_{\perp} AT A MASS OF $3.0 \text{ GeV}/c^2$. THE MEASURED X_F DISTRIBUTION IS ASSUMED TO CALCULATE THIS CURVE. EVENTS WITH $X_F > 0.1$ ARE CONSIDERED.

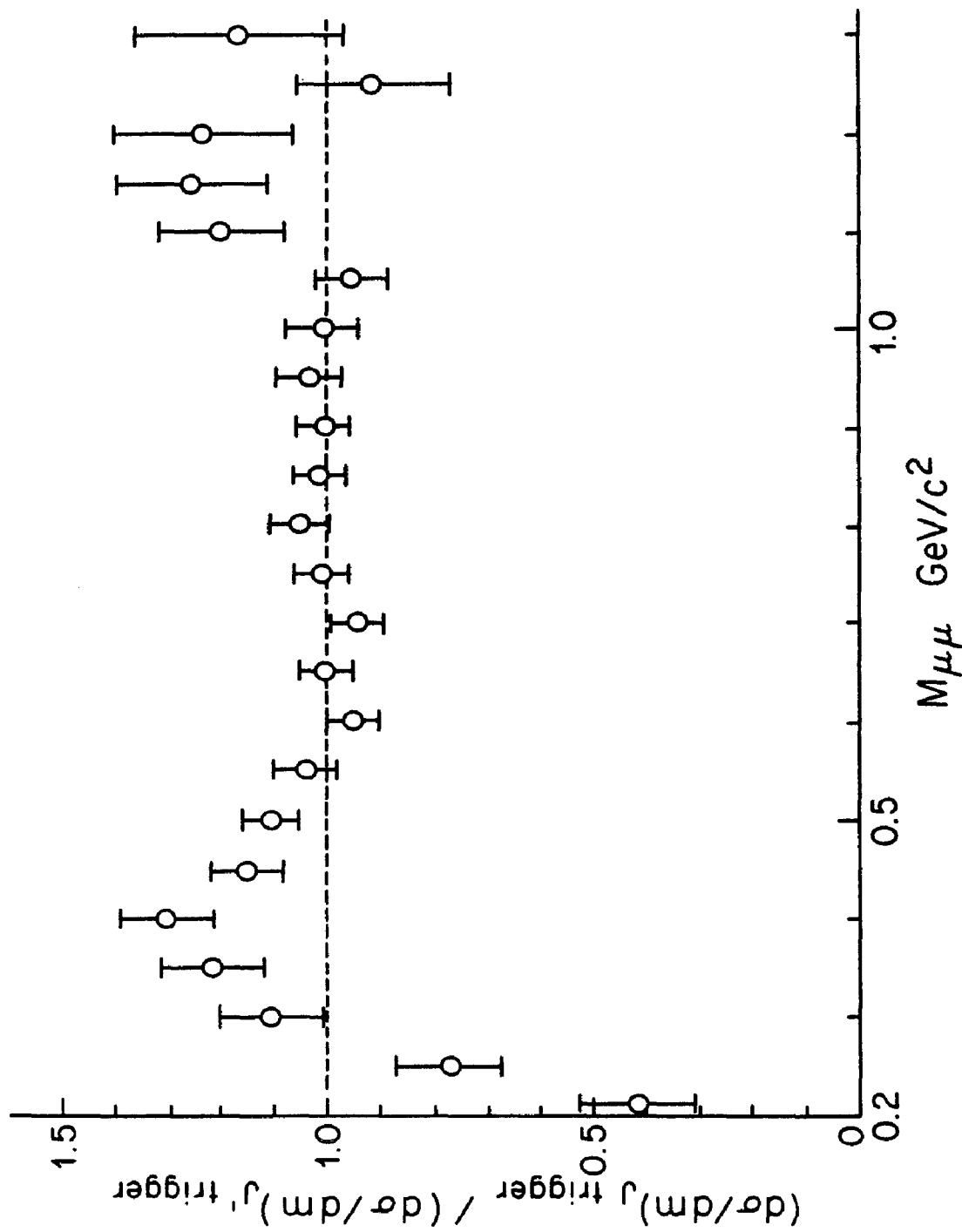


FIGURE 4-16. THE RATIO OF $\frac{d\sigma}{dm}$ AS CALCULATED FROM DATA TAKEN WITH THE J TRIGGER TO THAT TAKEN WITH THE J' TRIGGER IS SHOWN AS A FUNCTION OF MASS. THIS TESTS OUR UNDERSTANDING OF THE ACCEPTANCE WITH THE J TRIGGER REQUIREMENT AS WELL AS THE EFFICIENCY OF THE J TRIGGER.

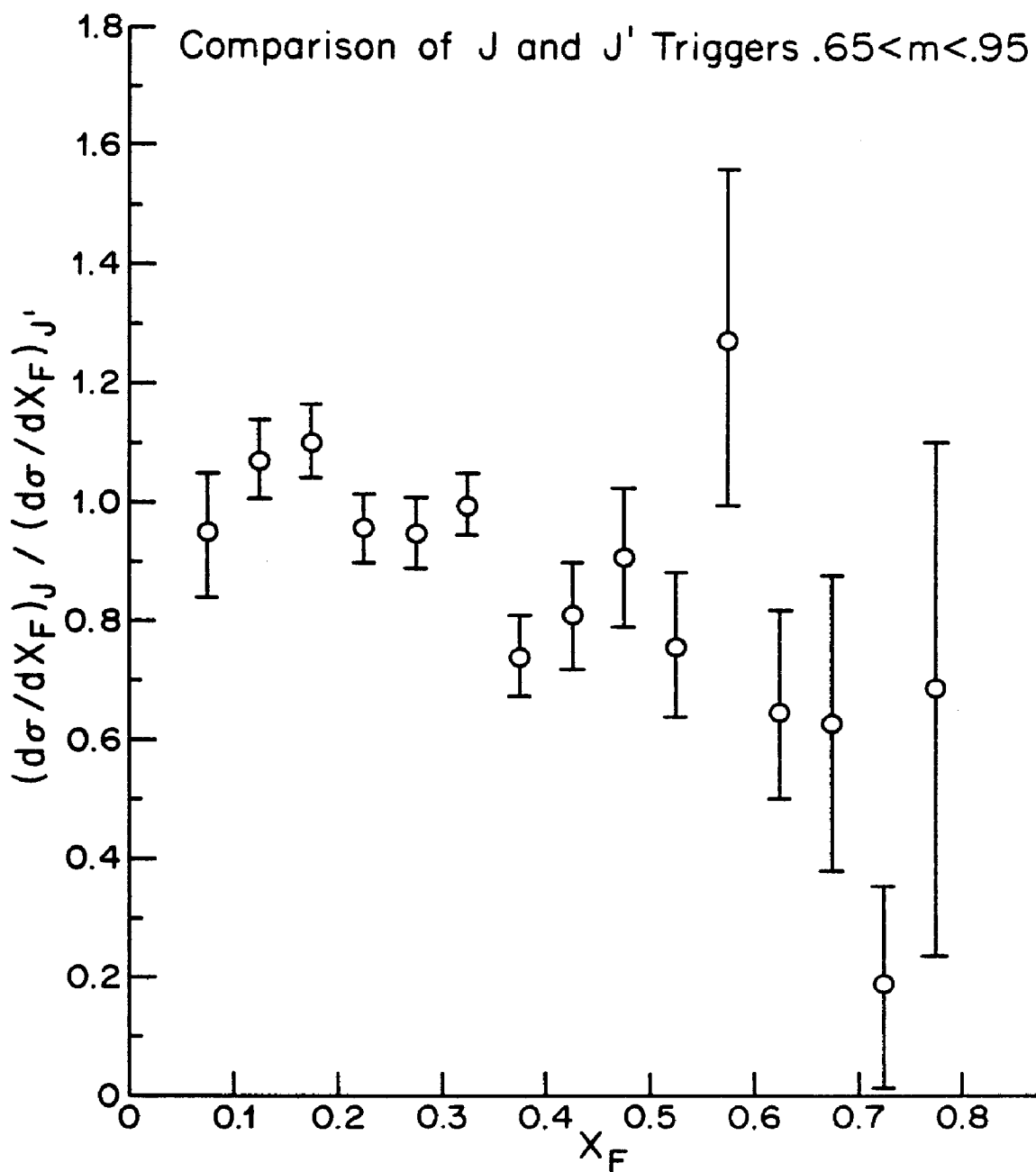


FIGURE 4-17. THE RATIO OF $\frac{d\sigma}{dx}$ ($0.65 < m_{\mu\mu} < 0.95$)

FROM DATA TAKEN WITH THE J TRIGGER TO THAT TAKEN WITH THE J' TRIGGER IS SHOWN AS A FUNCTION OF X_F .

that the J trigger data is useful for $m > 0.65 \text{ GeV}/c^2$.

Statistical errors on the efficiency and distortion were also calculated and were folded in with the statistical errors on the data to give the final errors. The efficiency errors, however, make only a very small contribution to the overall error. Since the efficiencies are weighted the calculation of the error is somewhat complicated. The following is the formula used:

$$\sigma_{\epsilon}^2 = \frac{\epsilon^2 \sum_{\text{tries}} W_i^2 + (1-2\epsilon) \sum_{\text{Successes}} W_i^2}{\sum_{\text{tries}} W_i^2}$$

The error on the distortion D was very small and was calculated in a similar way, with correlations between distorted and undistorted successes taken into account.

The data were binned in the same way as the efficiencies and weighted with E/p_{\perp} for cross sections 2 and 3 of the four types listed above. Cross sections were computed with the normalization, efficiencies and distortions described.

F. Secondary Production

The data from carbon targets of different thicknesses were compared to measure the effect of secondary production. Figure 4-18 shows the ratio of $d\sigma/dx_{\perp}$ for the 13.97 cm target to that for the the 7.46 cm target in the ρ - w mass region.

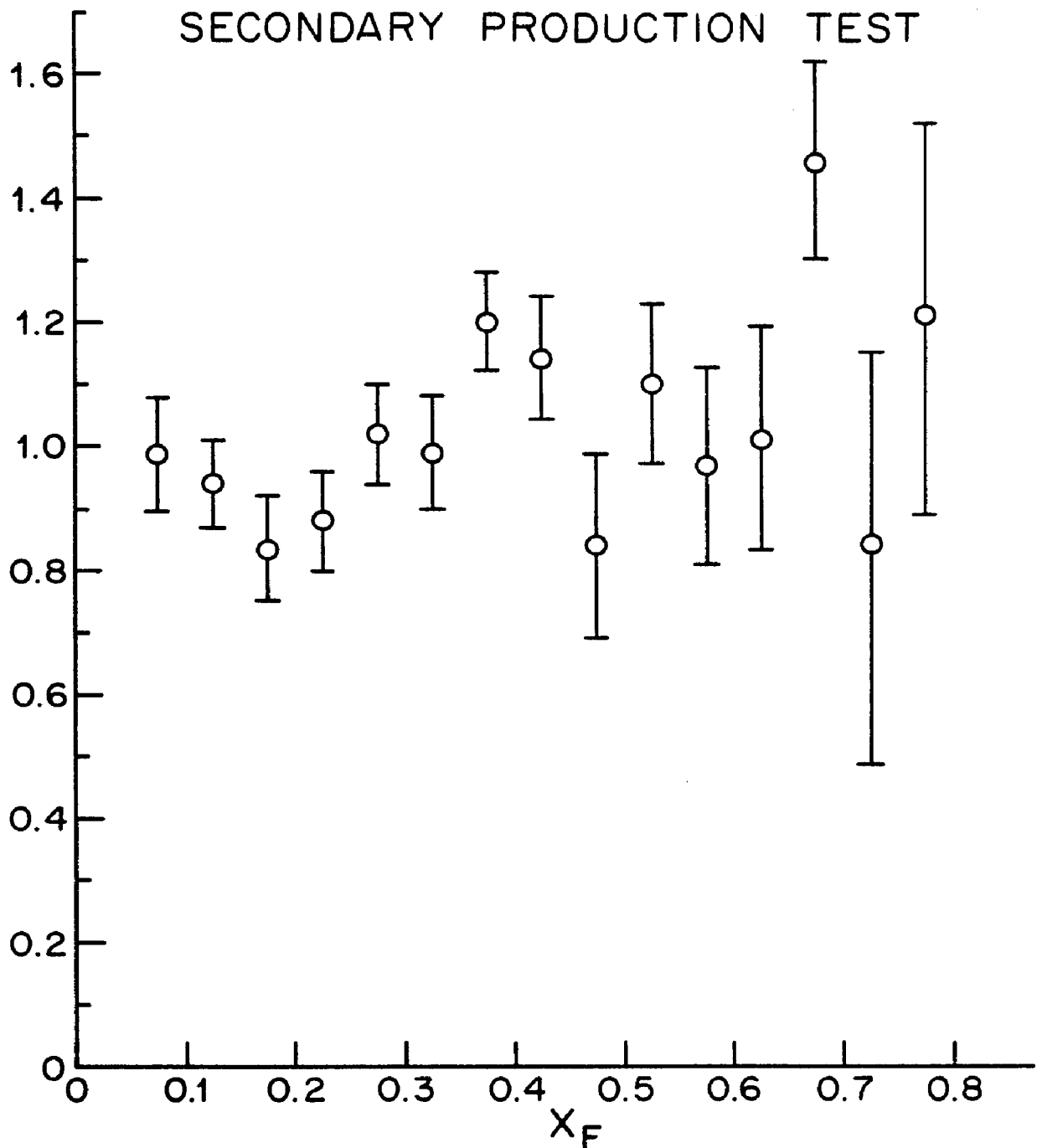


FIGURE 4-18. THE RATIO OF $\frac{d\sigma}{dx_F}$ ($0.65 < m < 0.95$) COMPUTED FROM DATA TAKEN WITH A 13.97 CM CARBON TARGET TO THAT COMPUTED FROM DATA TAKEN WITH A 7.46 CM CARBON TARGET AS A FUNCTION OF x_F . A SIGNAL OF SECONDARY PRODUCTION HERE WOULD BE RATIOS GREATER THAN ONE AT LOW x_F .

There is no surplus at low x_F in the 13.97 cm data as would be expected if secondary production played an important role. The following table shows total cross sections for ρ - ω and J production for the various targets.

Total ρ - ω and J Cross Sections for Various Target Thicknesses
($x_F > .1$) (nanobarns / nucleus)

Target Thickness (cm)	Beam		
7.46	p	134 \pm 2	2.03 \pm .10
12.54	p	125 \pm 2	1.81 \pm .15
13.97	p	133 \pm 2	1.82 \pm .15
7.46	π^+	152 \pm 3	4.02 \pm .27
12.54	π^+	153 \pm 4	3.87 \pm .69
13.97	π^+	153 \pm 3	3.55 \pm .37

Again there is no evidence of secondary production in these results.

CHAPTER V. Results

A. Mass, x_F and P_{\perp} Distributions

In this section, I will present differential cross sections as functions of mass, x_F and transverse momentum. Because of the large acceptance of the CCM spectrometer, the amount of information to be displayed is vast. I will present this information, here, in figures and tables, leaving the general features of these results to be discussed in section B of the chapter.

In figures 5-1 and 5-2 $d\sigma/dm$ ($x_F > 0.1$) is plotted for the five interactions listed below.

$$p + C \text{ -----} \rightarrow \mu^+ \mu^- + X$$

$$\pi^+ + C \text{ -----} \rightarrow \mu^+ \mu^- + X$$

$$\pi^- + C \text{ -----} \rightarrow \mu^+ \mu^- + X$$

$$p + Sn \text{ -----} \rightarrow \mu^+ \mu^- + X$$

$$\pi^+ + Sn \text{ -----} \rightarrow \mu^+ \mu^- + X$$

The five spectra are similar in general characteristics, all showing peaks due to known vector mesons which decay to muon pairs (ρ , ω , and J). The ψ and ψ' mesons also make visible contributions.

Figures 5-3 through 5-16 display our measurement of $E \frac{d\sigma}{dx_F}$ in seven mass bins chosen to isolate resonant and continuum regions. Fits to the form $A(1-x_F)^N$ are also shown. The above functional form is used in the fits because

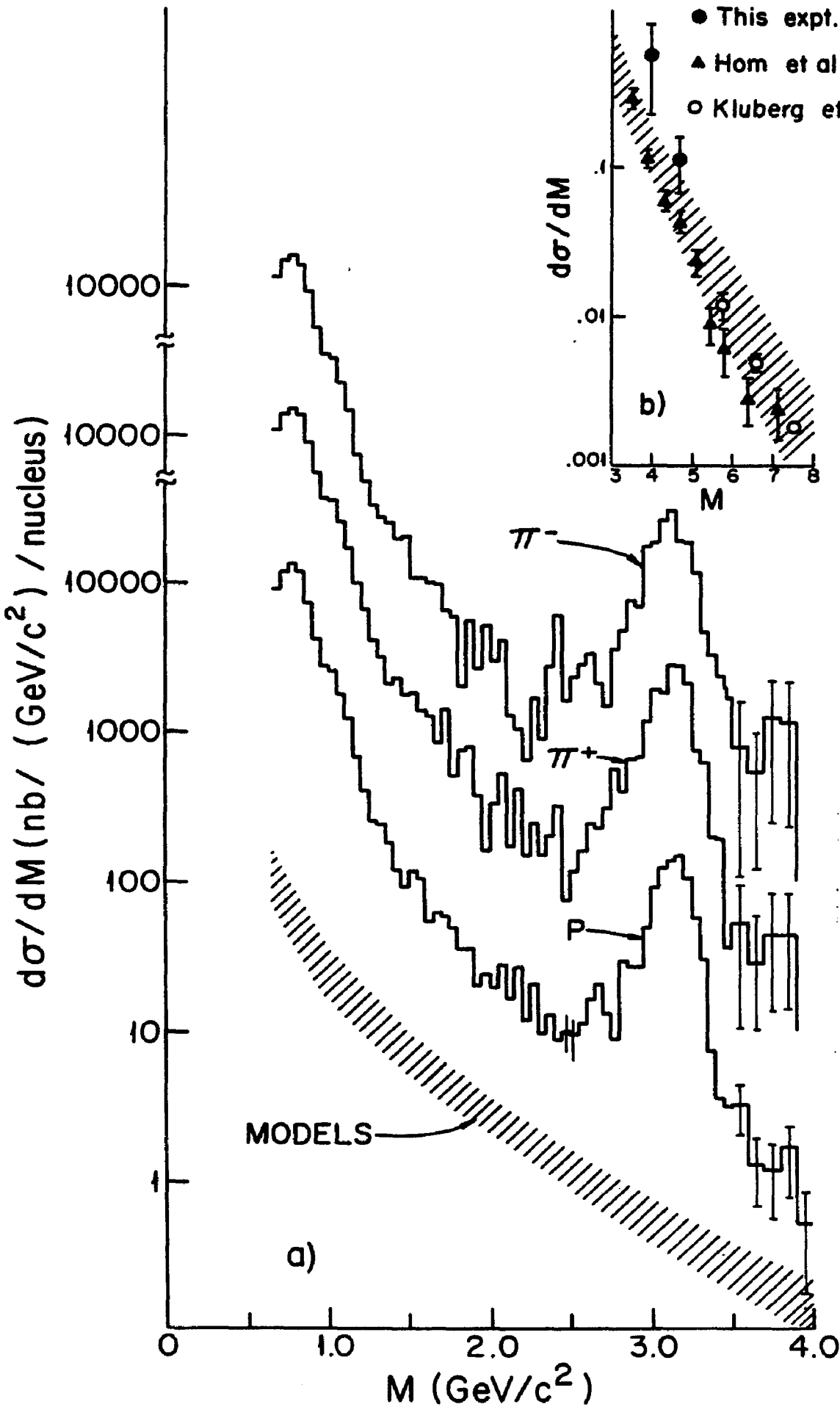


FIGURE 5-1. PLOTS OF $\frac{d\sigma}{dM}$ ($x_F > 0.1$) VERSUS MASS FOR π^+ , π^- AND PROTONS INCIDENT UPON A CARBON TARGET. (A) OUR DATA ARE SHOWN ALONG WITH DRELL-YAN MODEL CALCULATIONS (CROSSHATCHED AREA) FOR INCIDENT PROTONS. (B) OUR DATA AND SCALED DATA OF TWO OTHER EXPERIMENTS ARE SHOWN ALONG WITH DRELL-YAN MODEL PREDICTIONS.

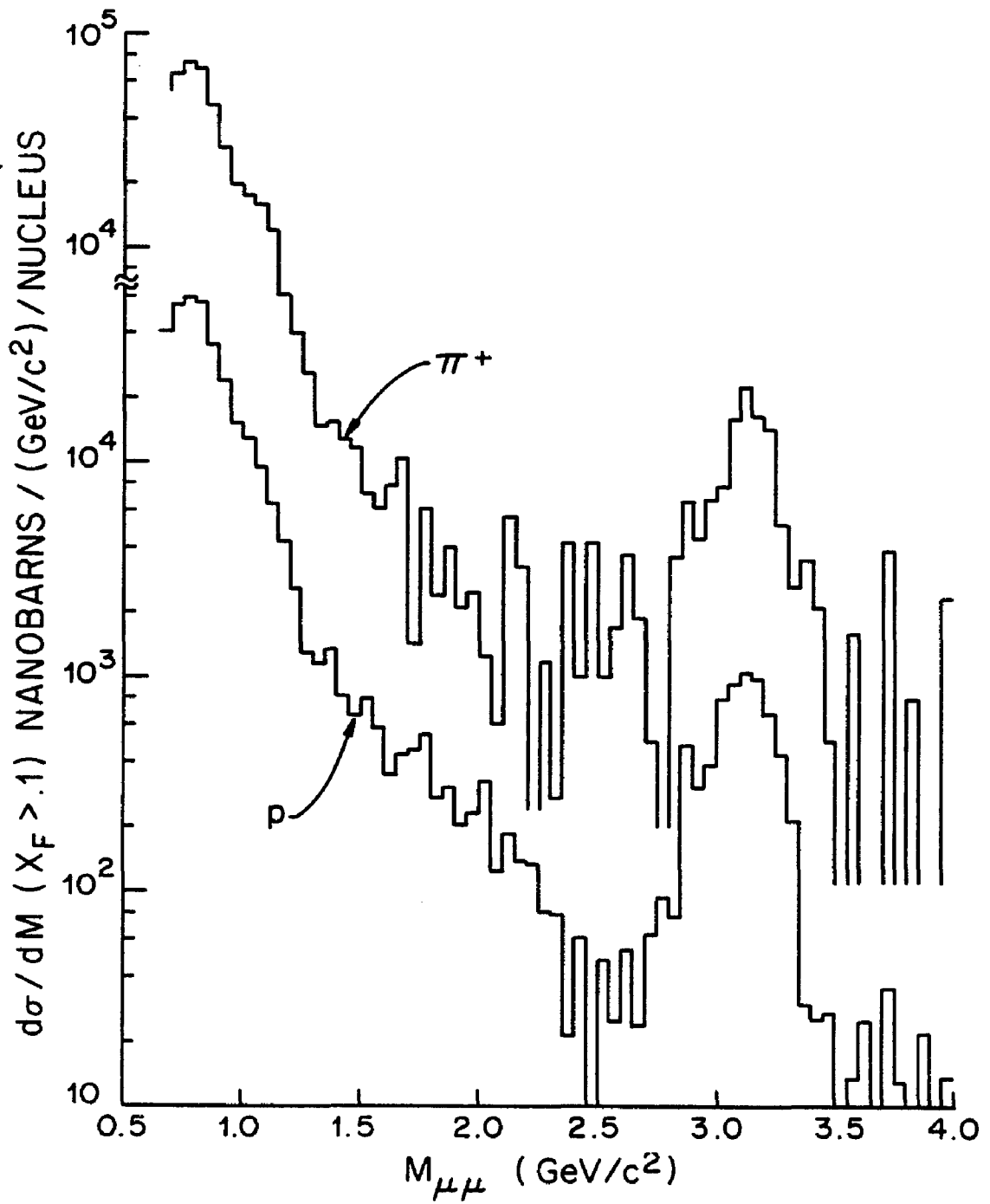


FIGURE 5-2. PLOTS OF $\frac{d\sigma}{dm} (x_F > 0.1)$ VERSUS MASS FOR π^+ AND PROTONS INCIDENT UPON A TIN TARGET.

FIGURES 5-3 THROUGH 5-9. PLOTS OF $E \frac{d\sigma}{dx_F}$
FOR π^+ , π^- AND PROTONS INCIDENT UPON A
CARBON TARGET. FITS TO THE FORM $A(1-x_F)^N$
ARE SHOWN.

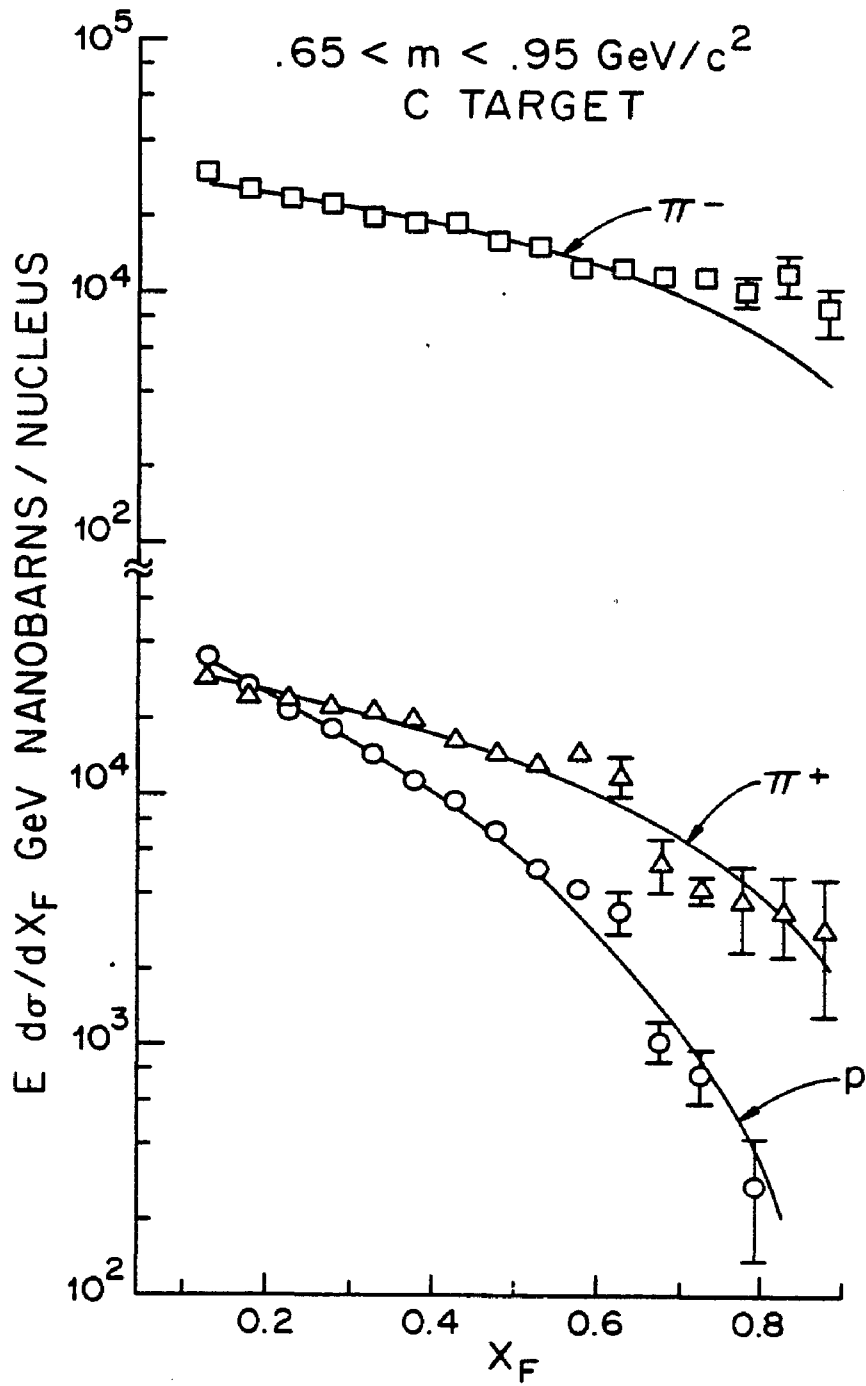


FIGURE 5-3

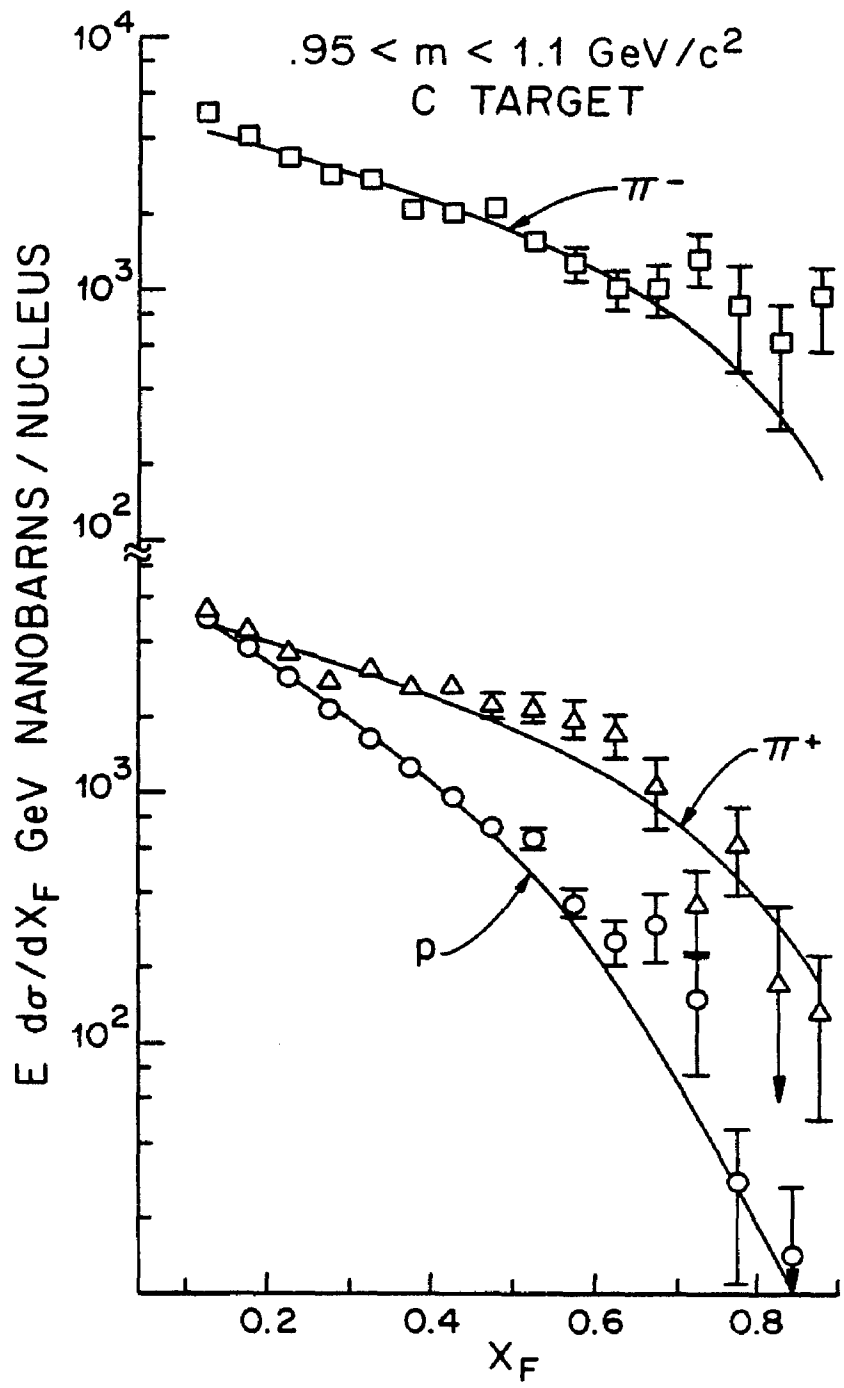


FIGURE 5-4

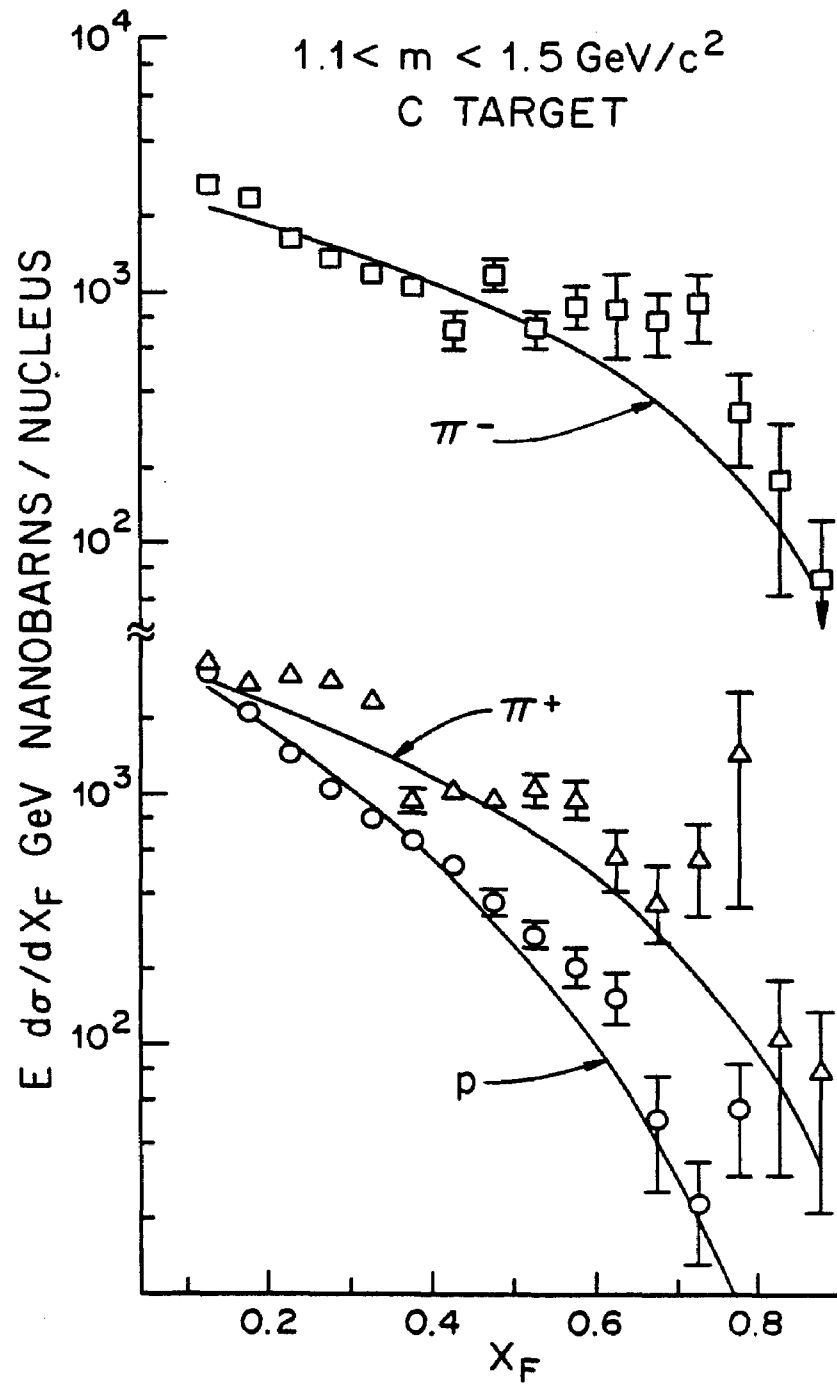


FIGURE 5-5

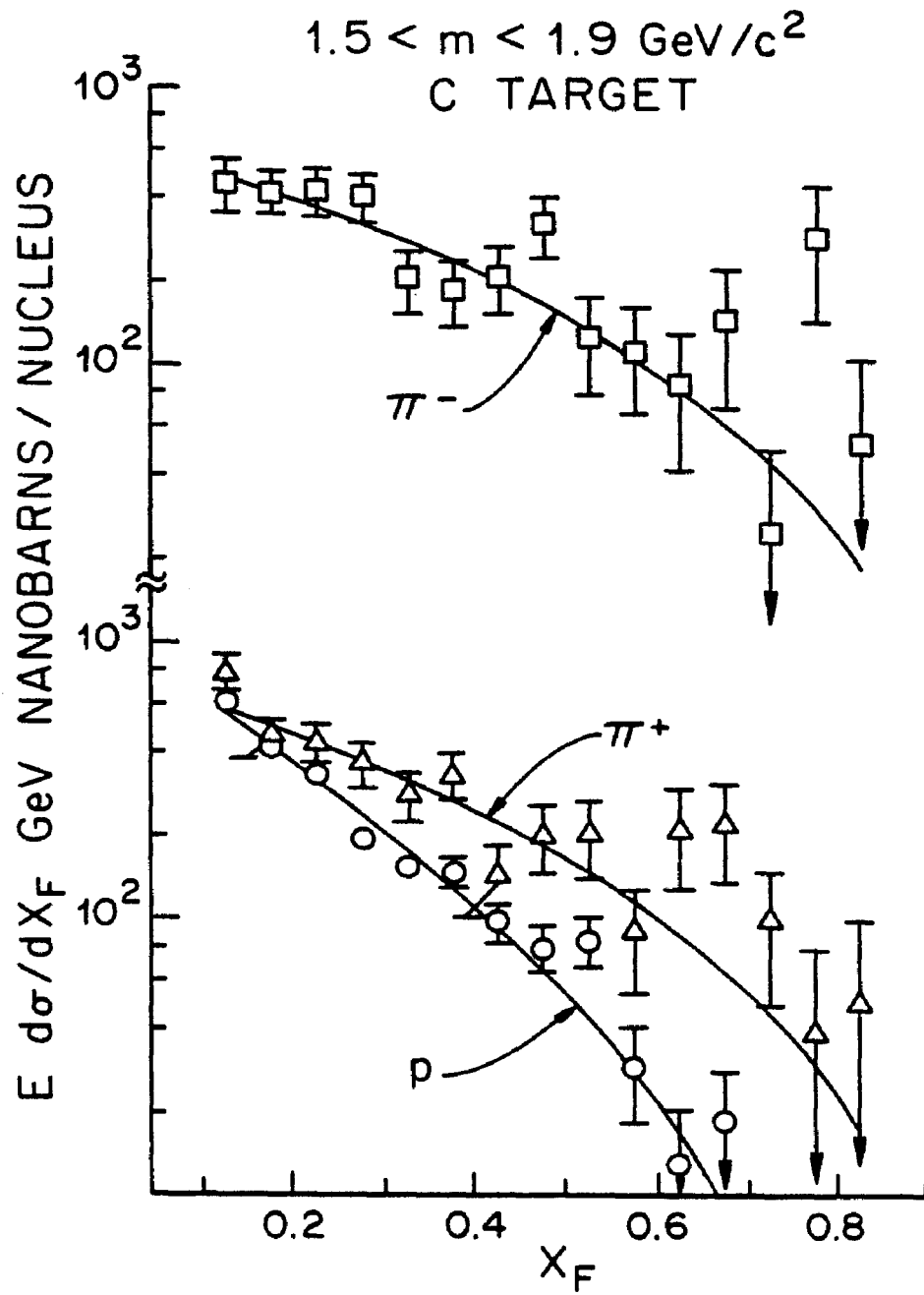


FIGURE 5-6

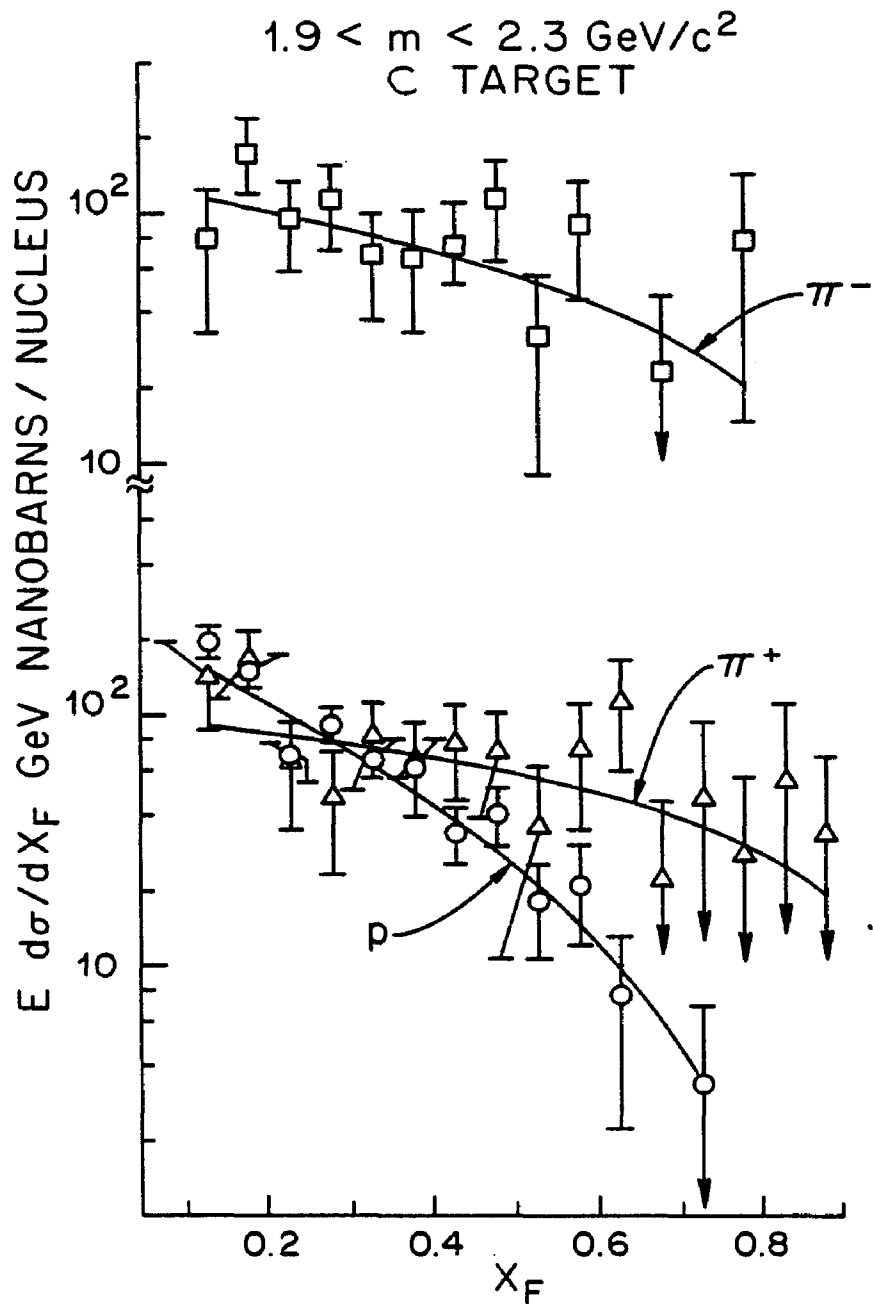


FIGURE 5-7

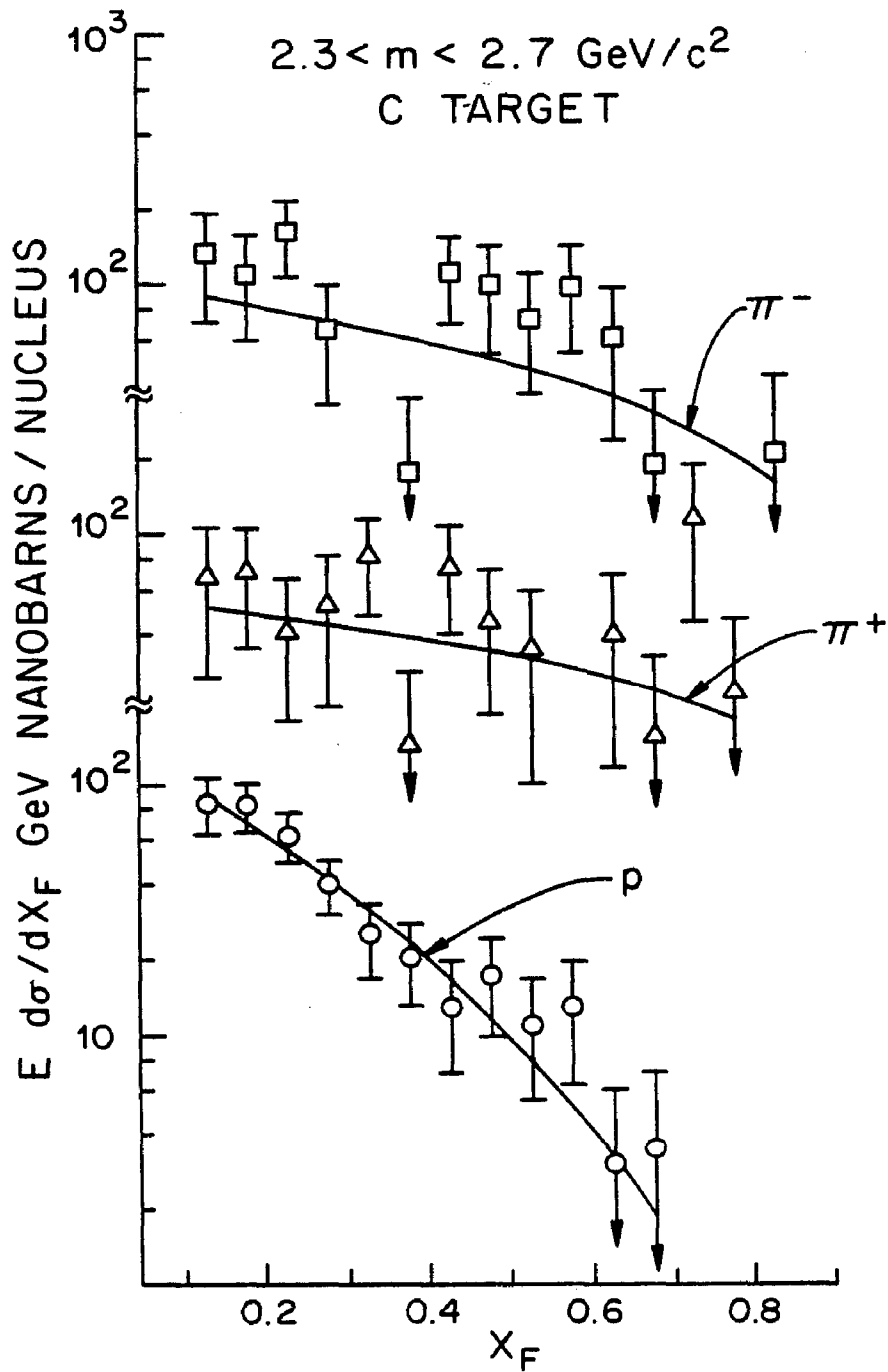


FIGURE 5-8

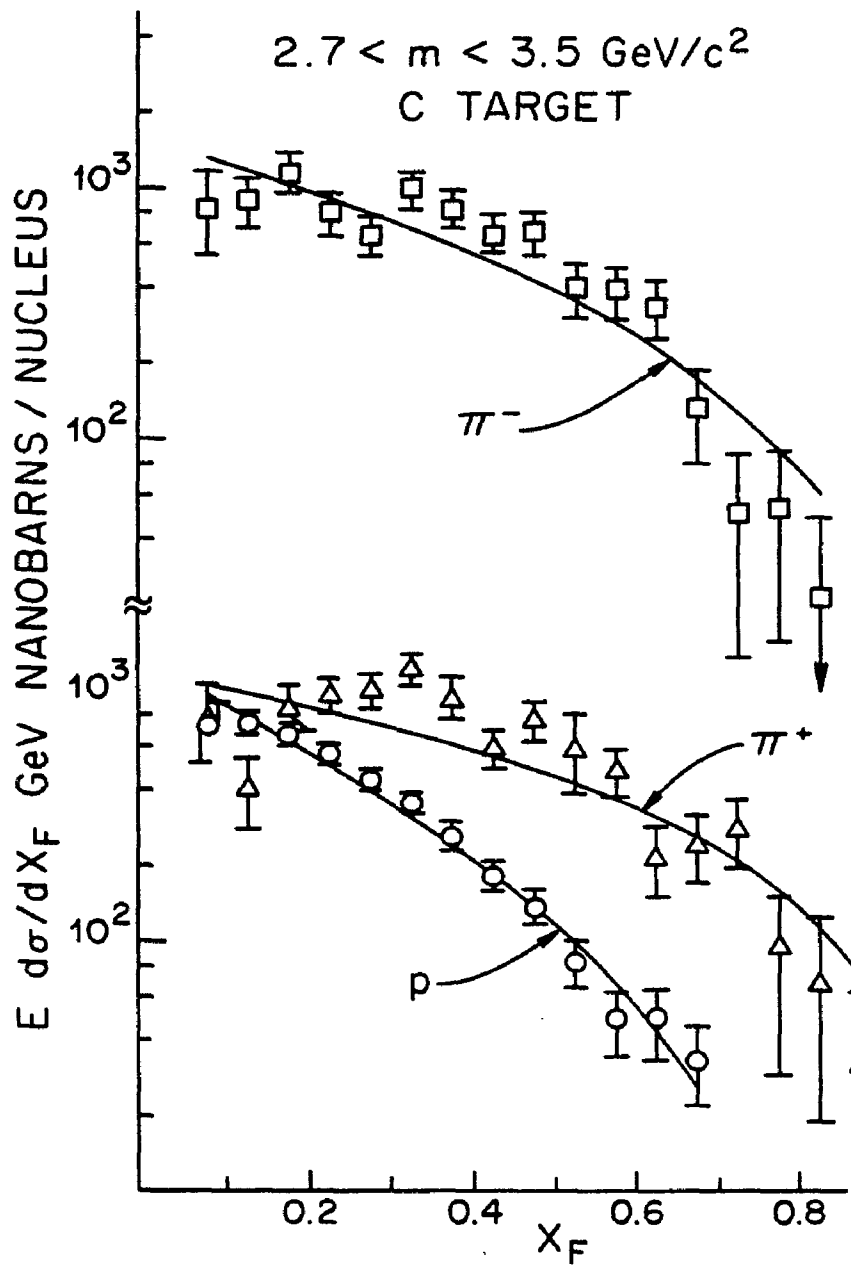


FIGURE 5-9

FIGURES 5-10 THROUGH 5-16. PLOTS OF $E \frac{d\sigma}{dx_F}$
FOR π^+ , π^- AND PROTONS INCIDENT UPON A SN
TARGET. FITS TO THE FORM $A(1 - x_F)^N$ ARE
SHOWN.

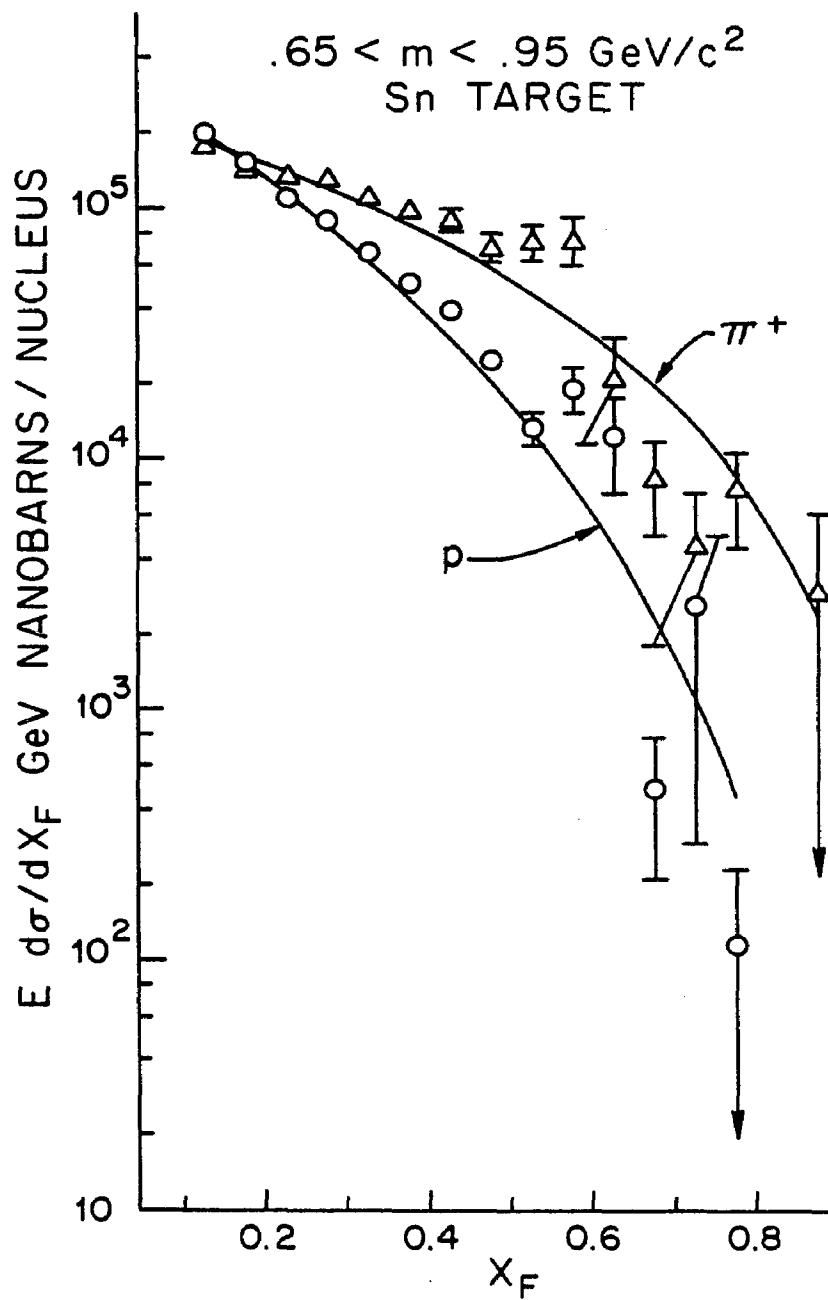


FIGURE 5-10

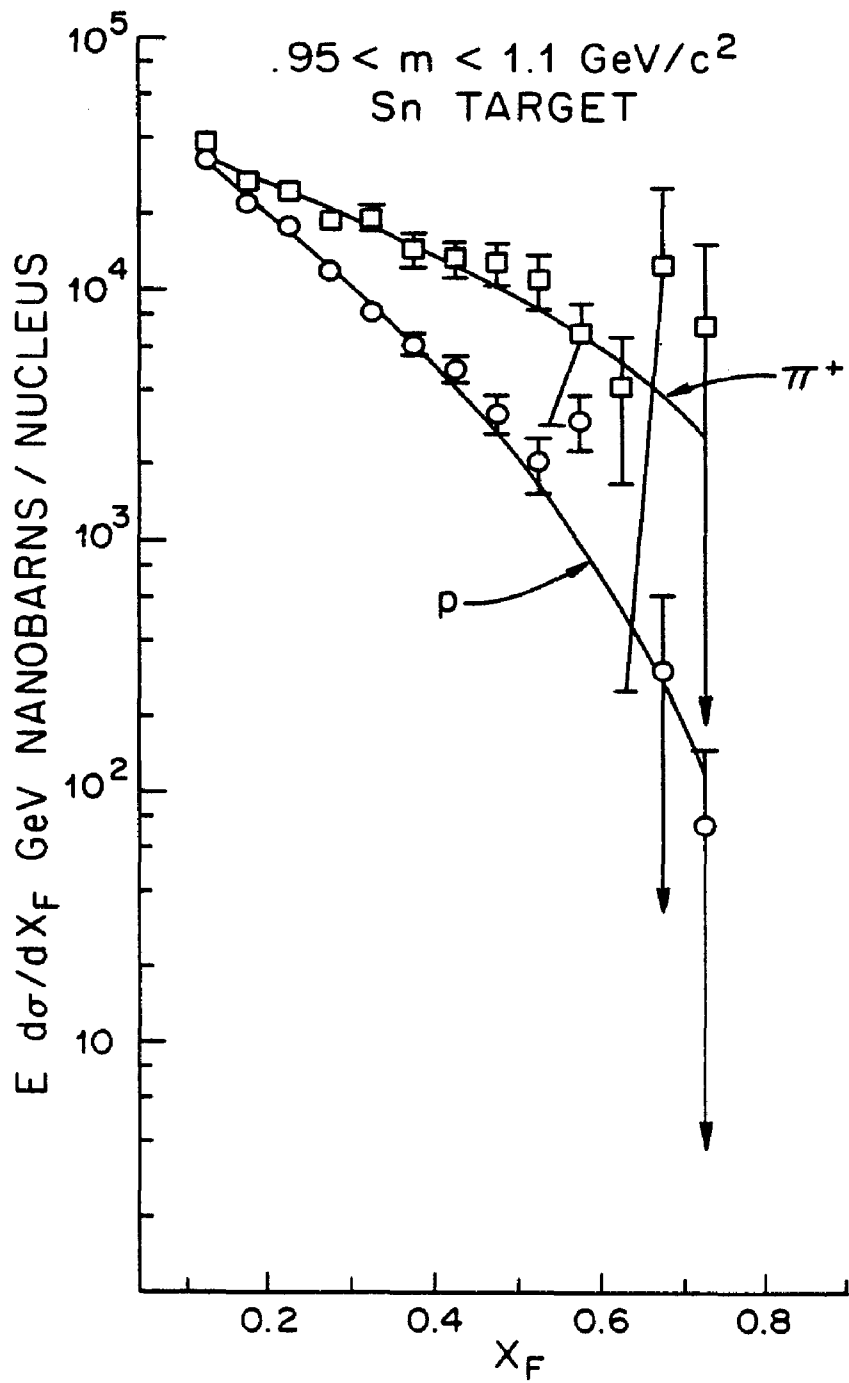


FIGURE 5-11

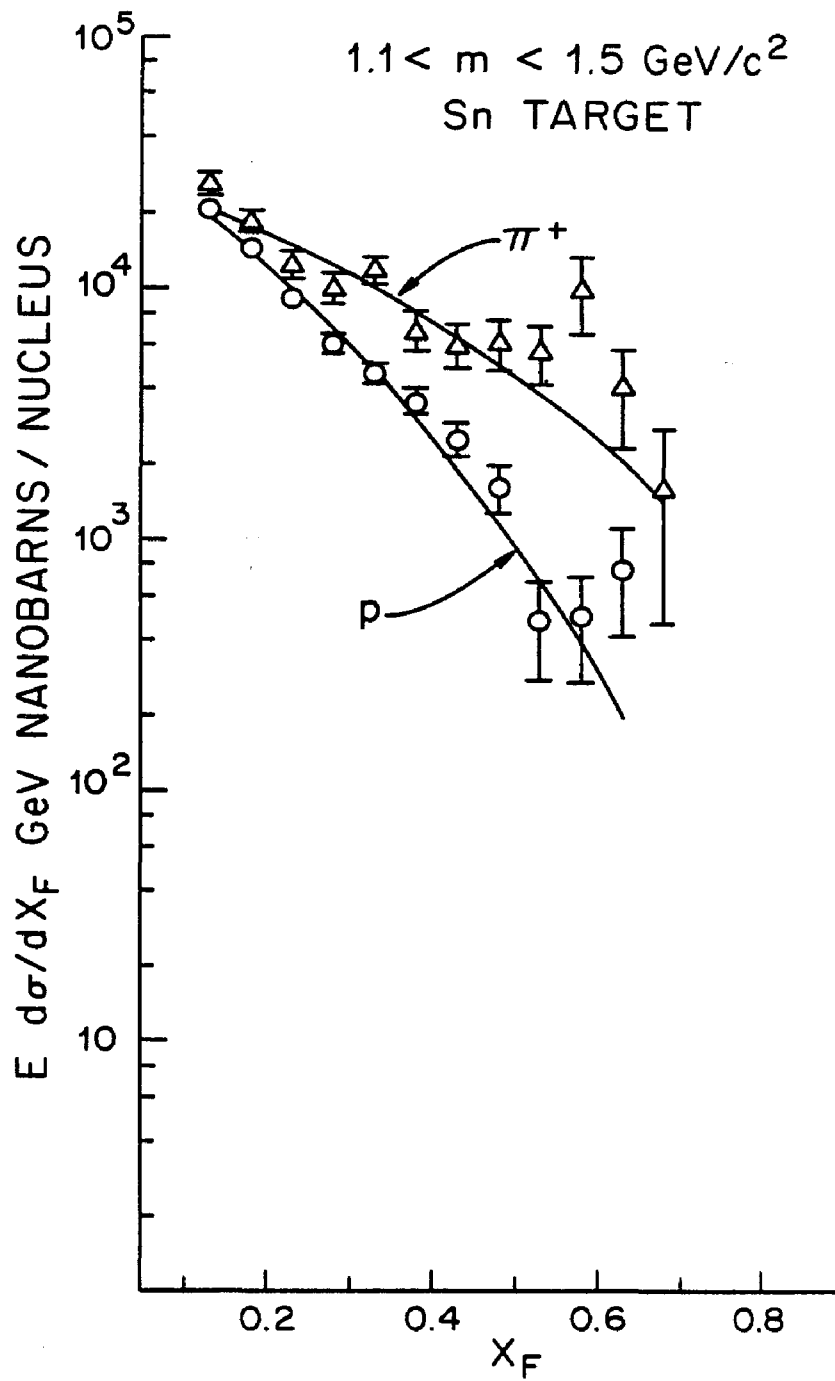


FIGURE 5-12

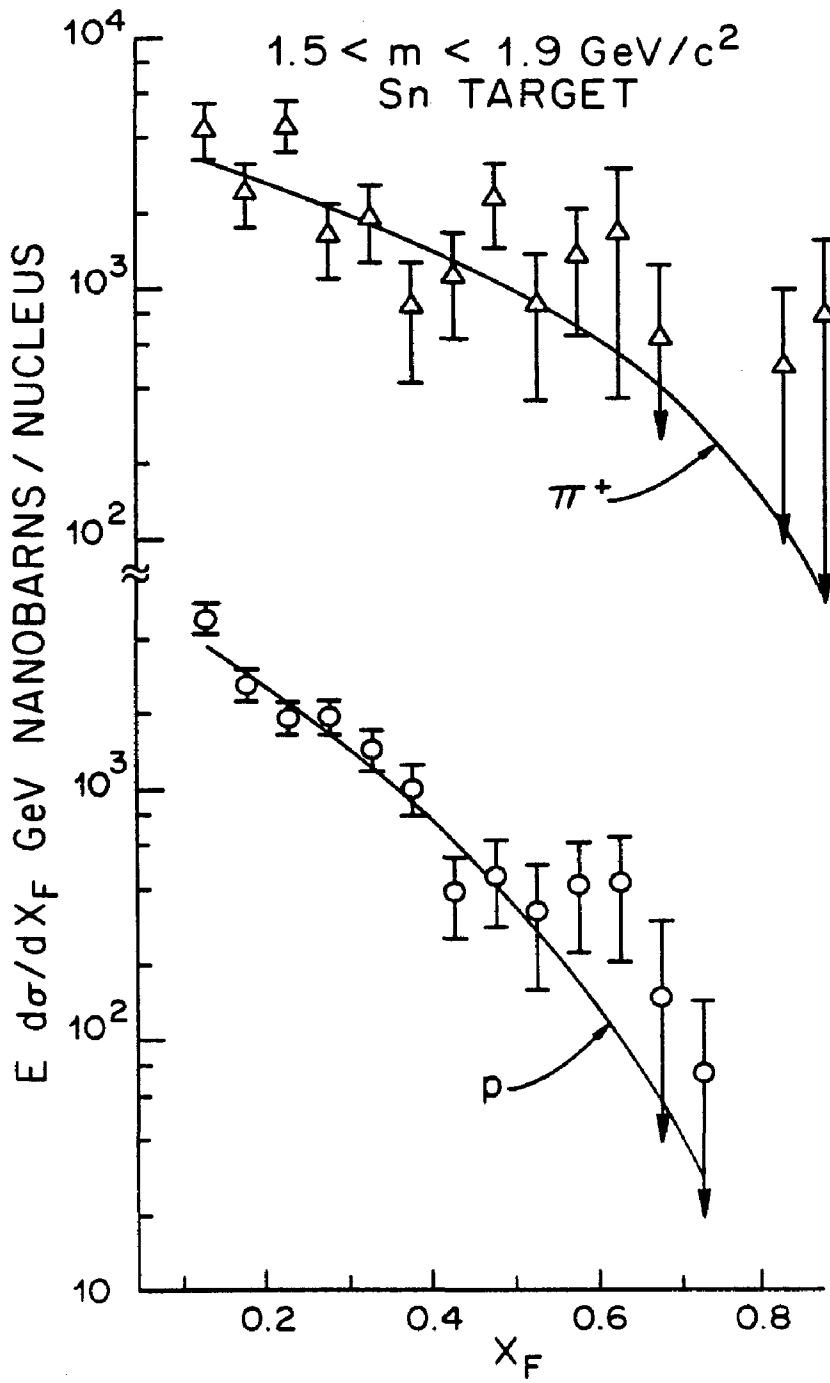


FIGURE 5-13

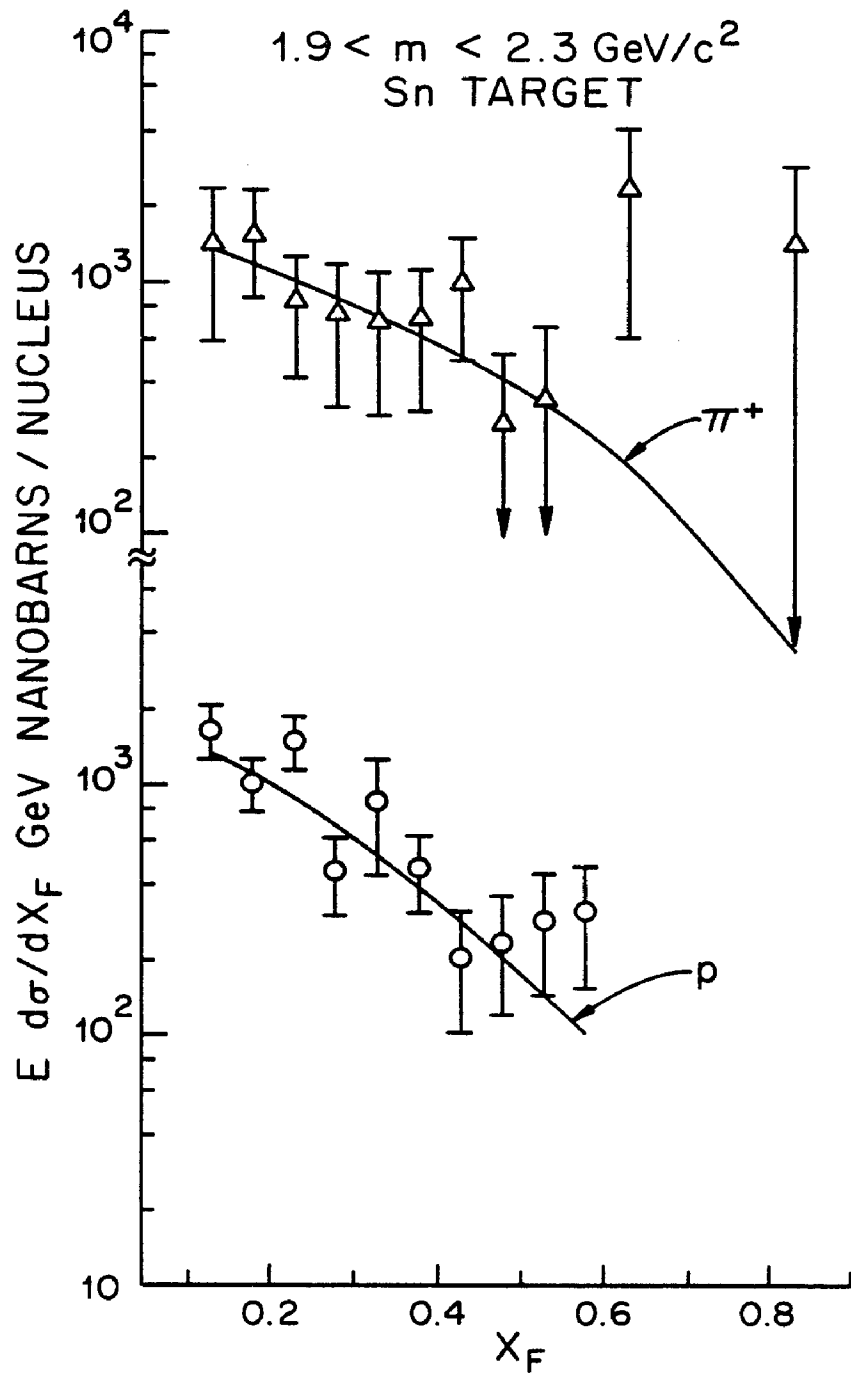


FIGURE 5-14

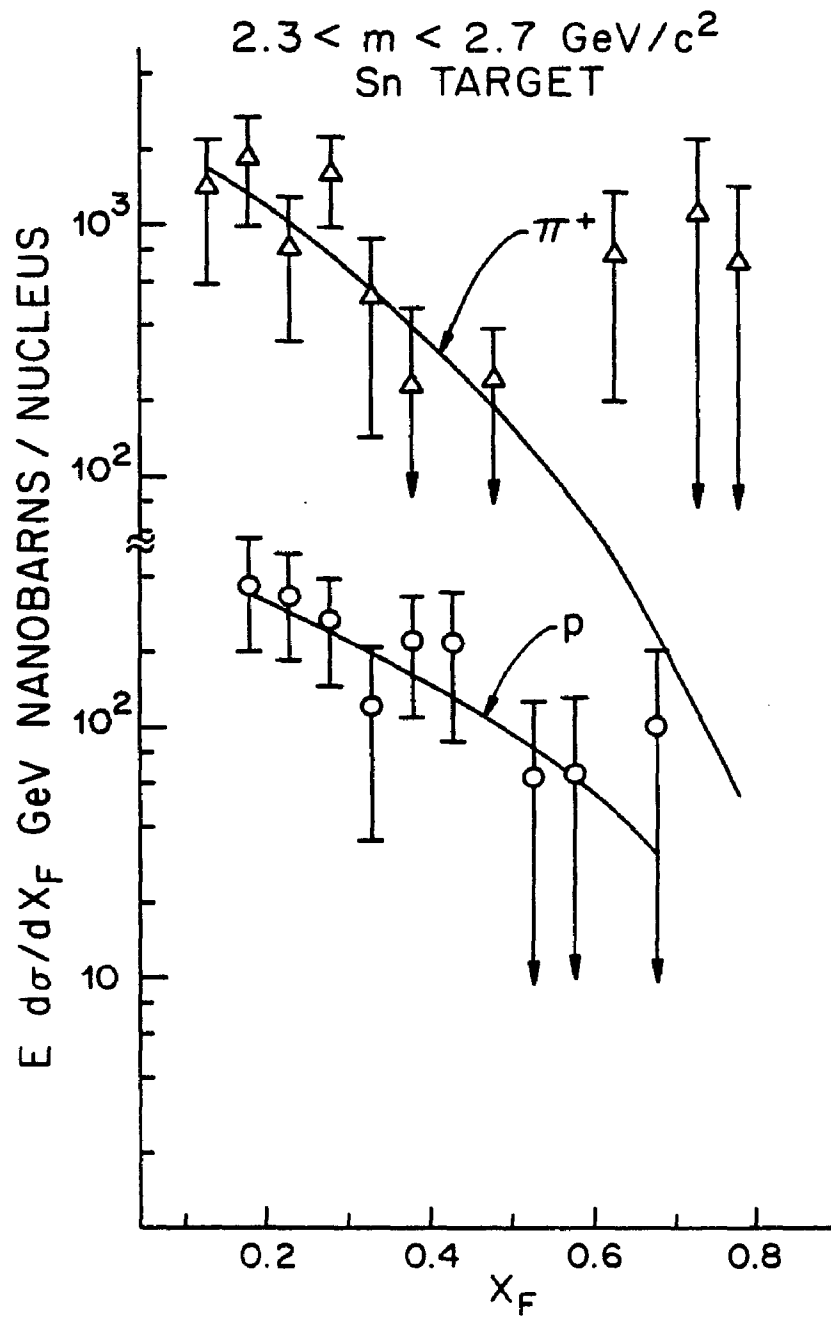


FIGURE 5-15

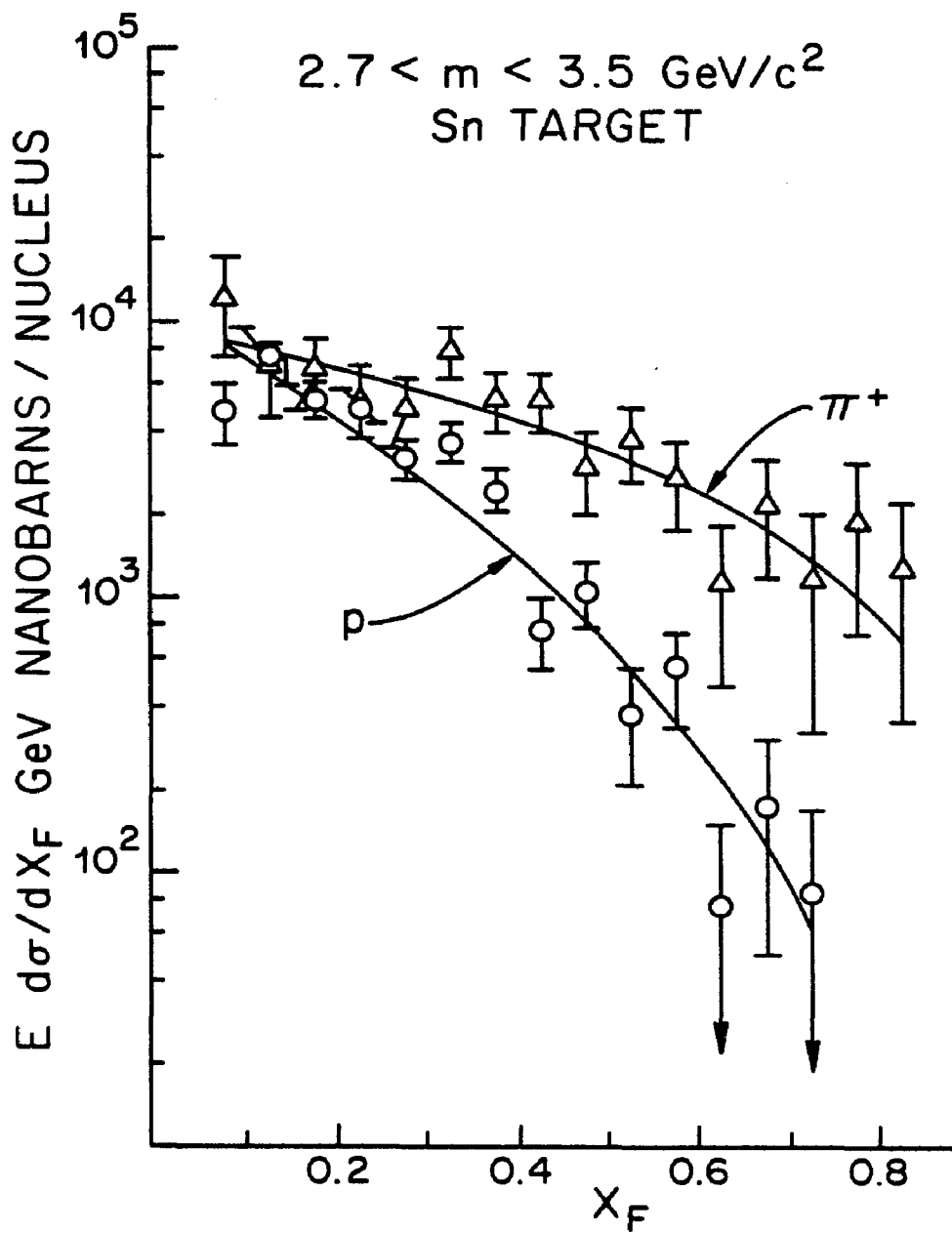


FIGURE 5-16

FIGURES 5-17 THROUGH 5-23. PLOTS OF $\frac{E}{P_{\perp}} \frac{d\sigma}{dP_{\perp}}$
FOR π^{+} , π^{-} AND PROTONS INCIDENT UPON A CARBON
TARGET. FITS TO THE FORM $A e^{-BP_{\perp}}$ ARE SHOWN.

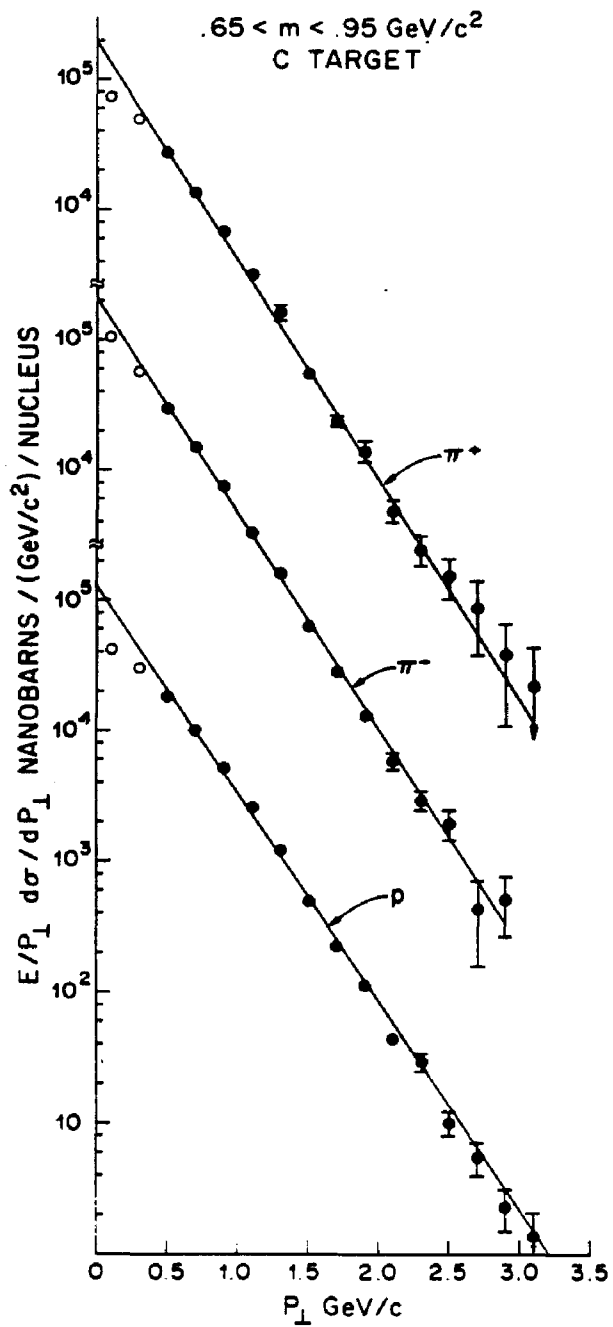


FIGURE 5-17

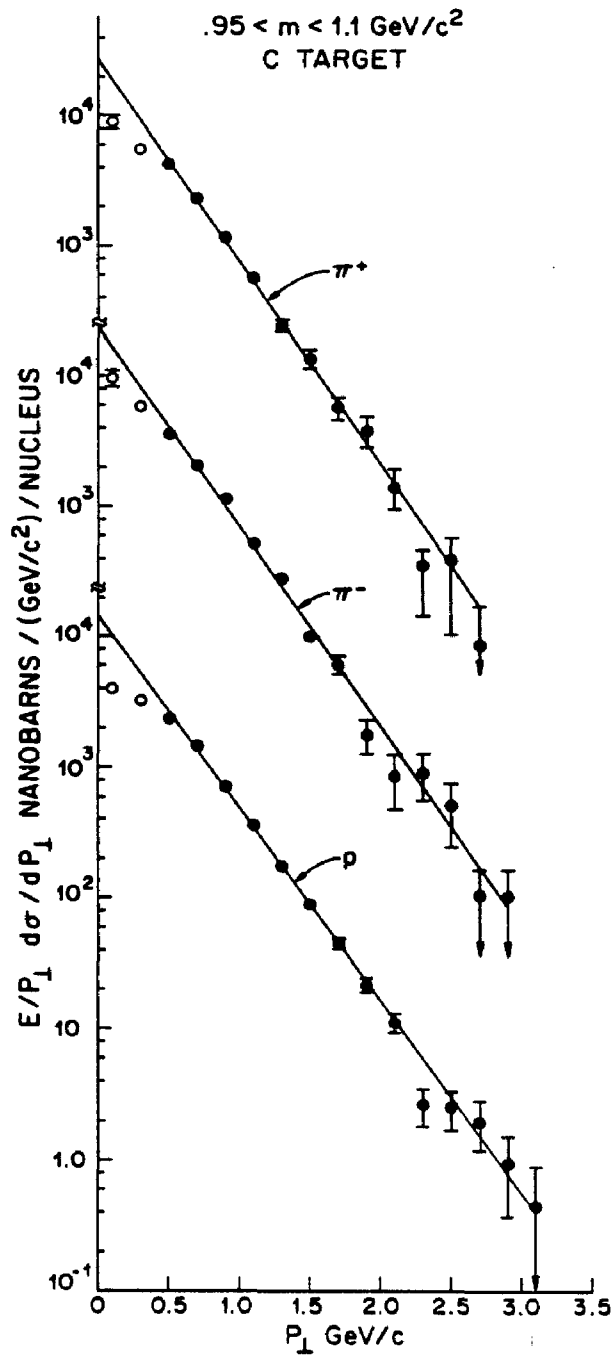


FIGURE 5-18

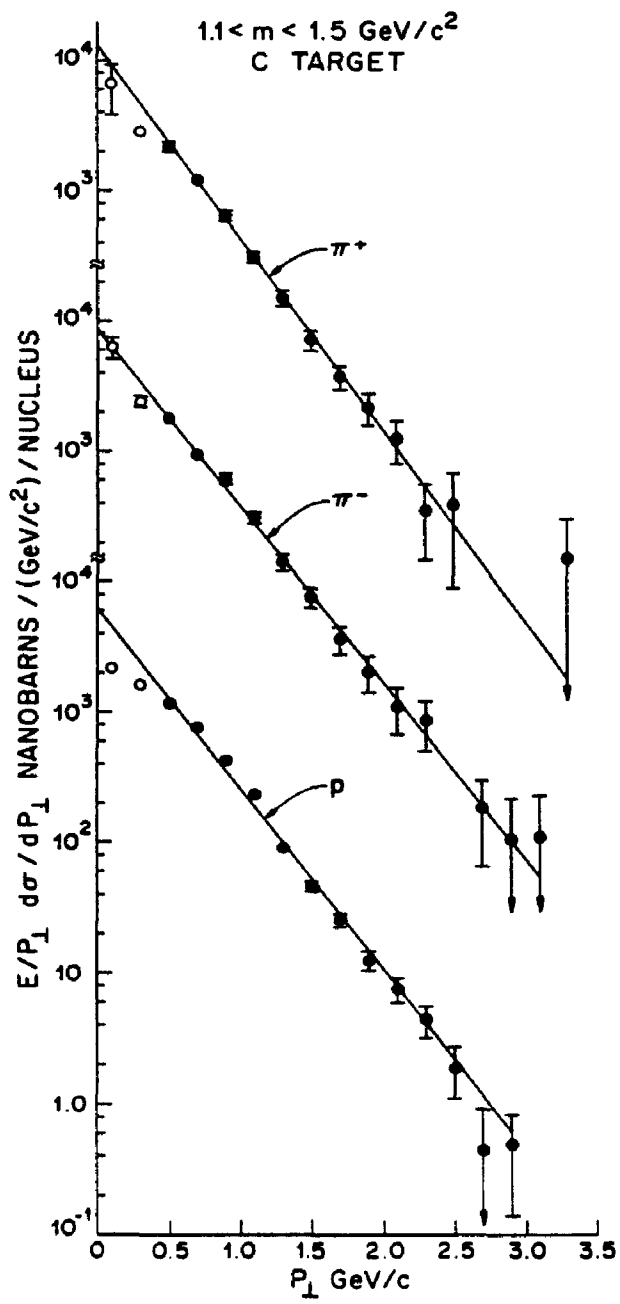


FIGURE 5-19

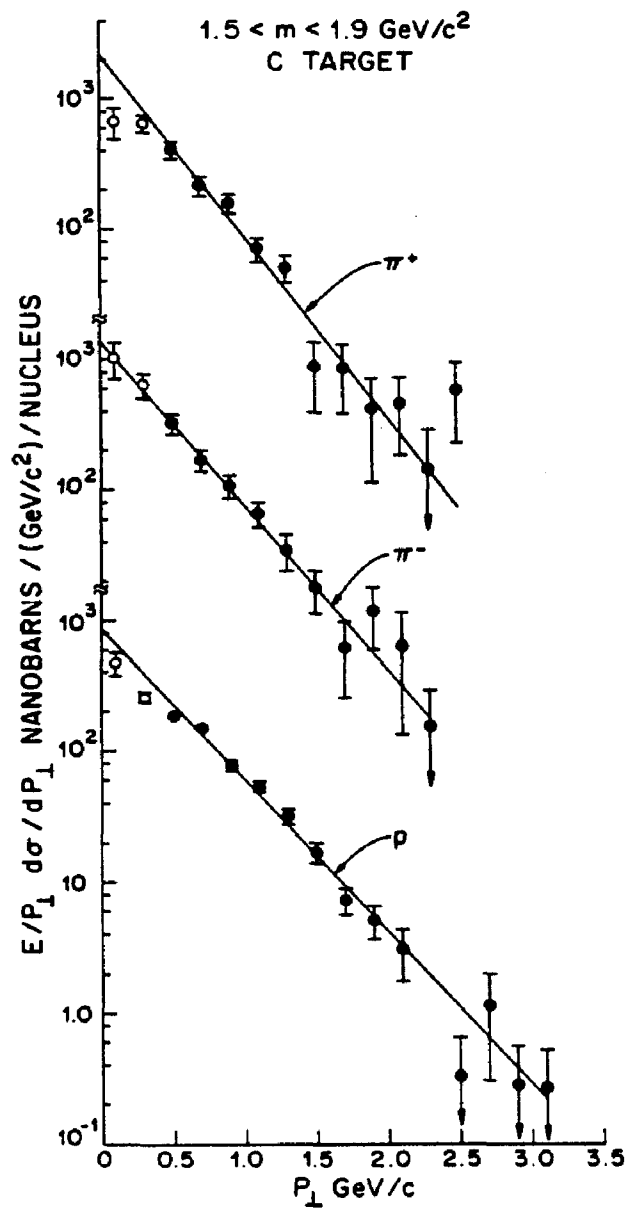


FIGURE 5-20

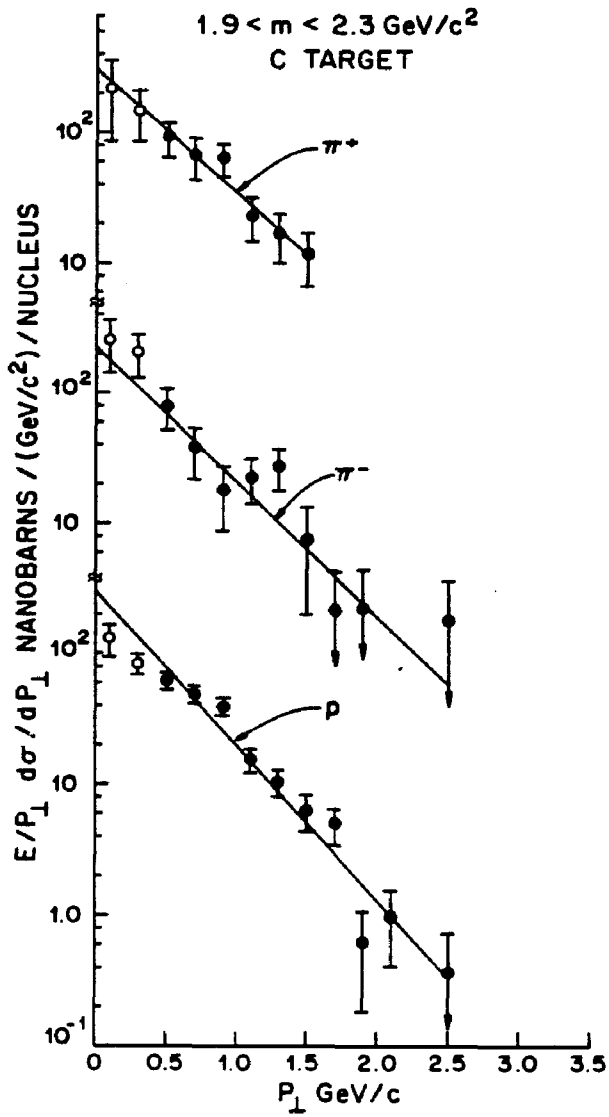


FIGURE 5-21

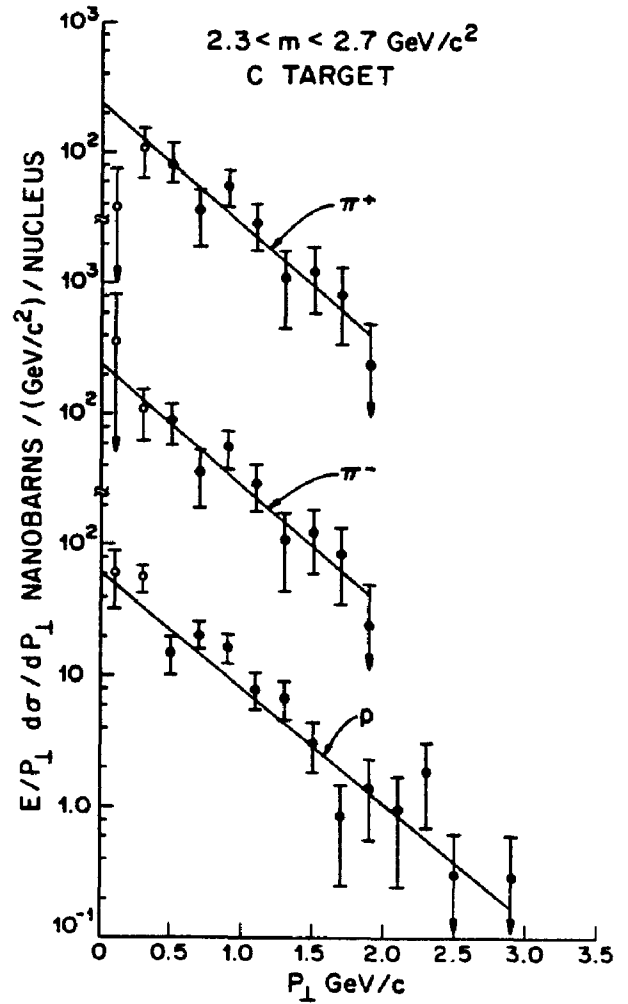


FIGURE 5-22

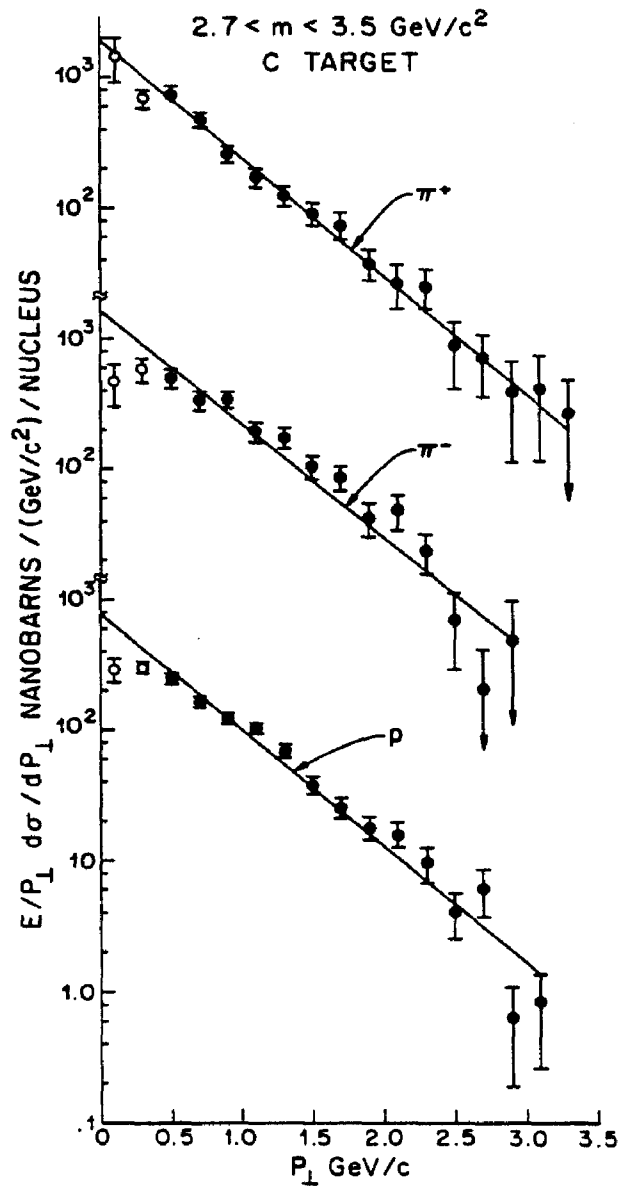


FIGURE 5-23

FIGURES 5-24 THROUGH 5-30. PLOTS OF $\frac{E}{P_{\perp}} \frac{d\sigma}{dP_{\perp}}$
FOR π^{+} AND PROTONS INCIDENT UPON A TIN TARGET.
FITS TO THE FORM $A e^{-BP_{\perp}}$ ARE SHOWN.

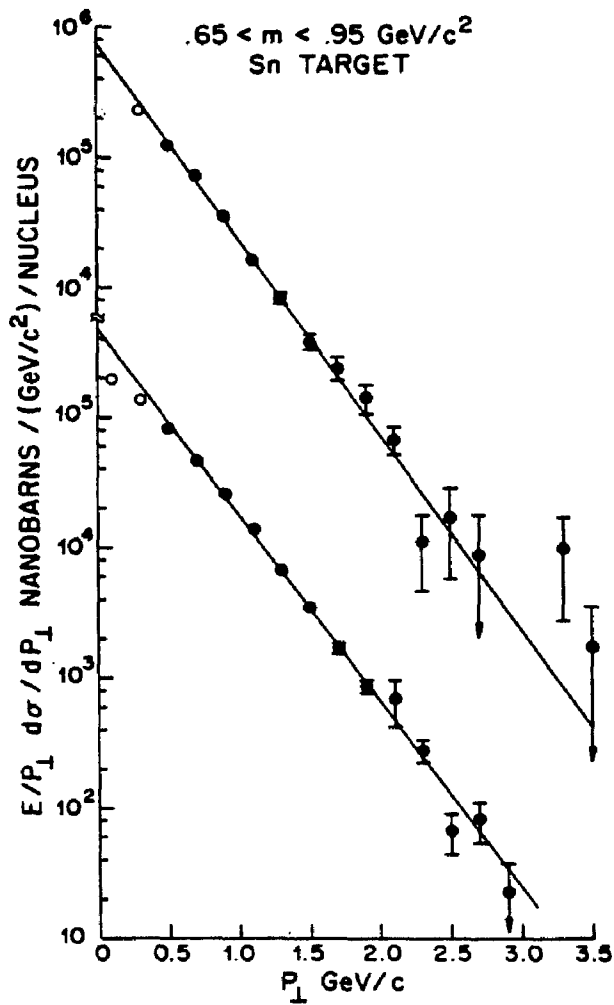


FIGURE 5-24

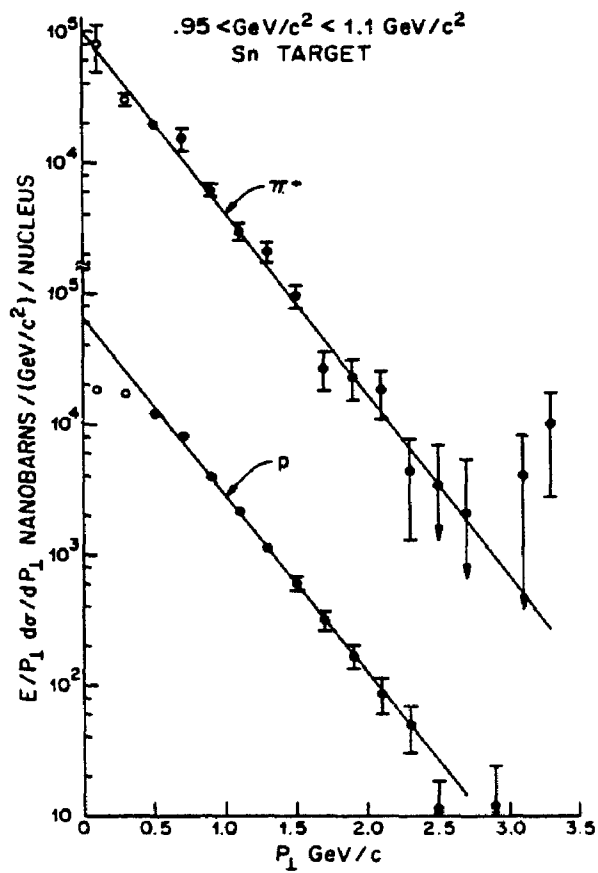


FIGURE 5-25

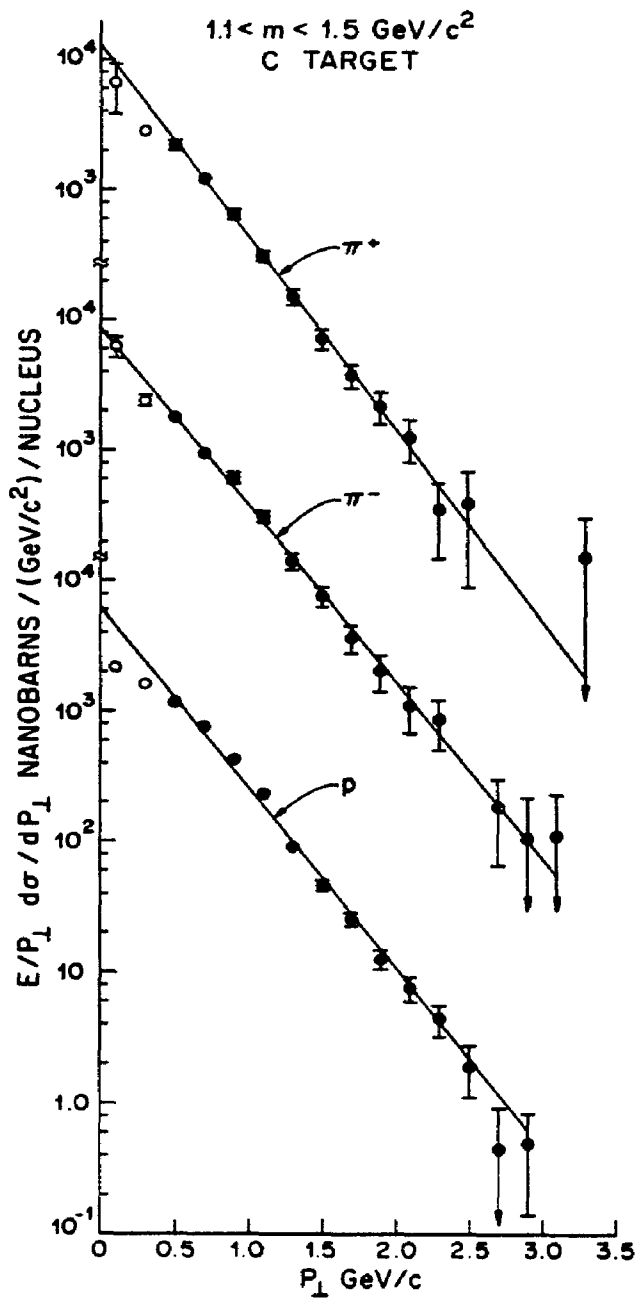


FIGURE 5-26

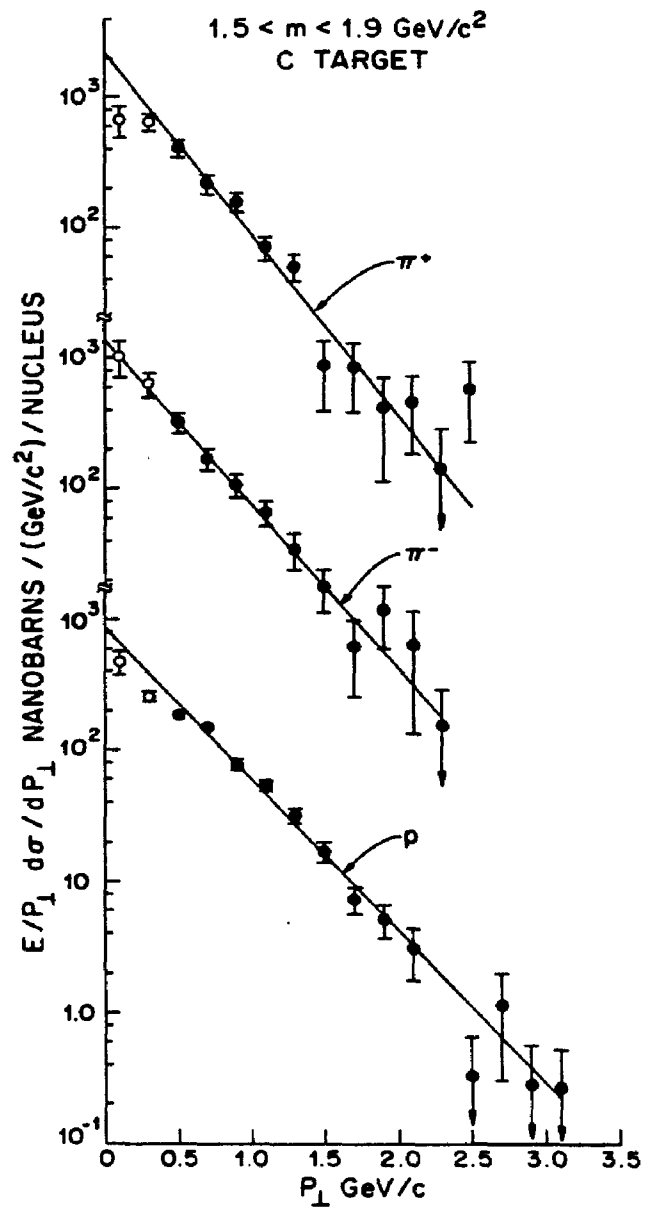


FIGURE 5-27

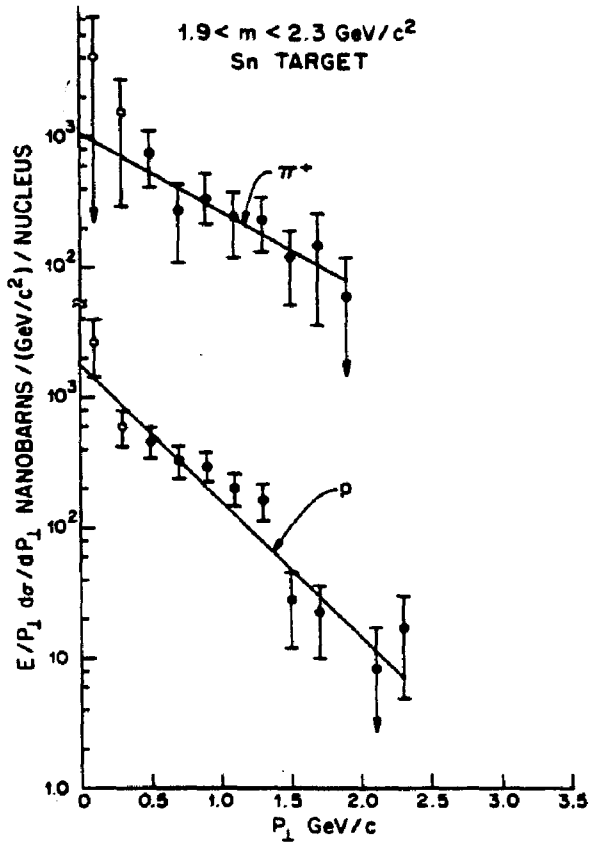


FIGURE 5-28

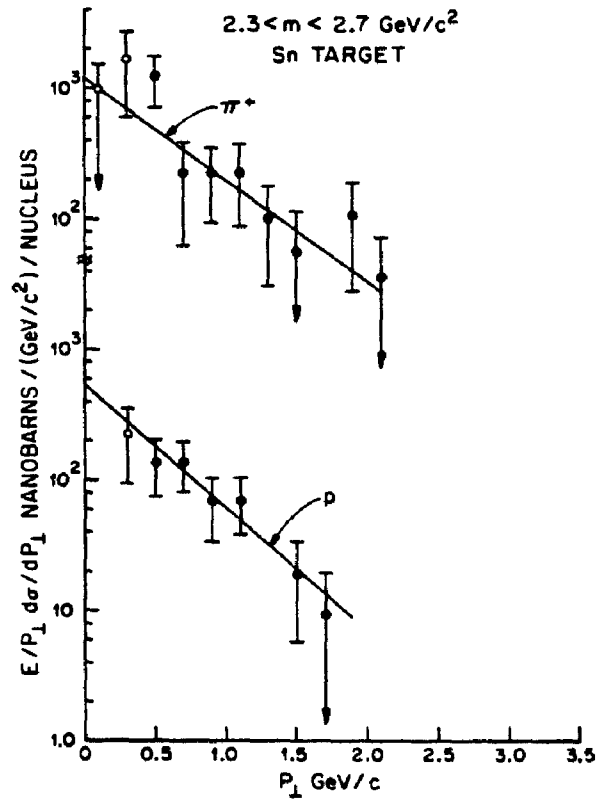


FIGURE 5-29

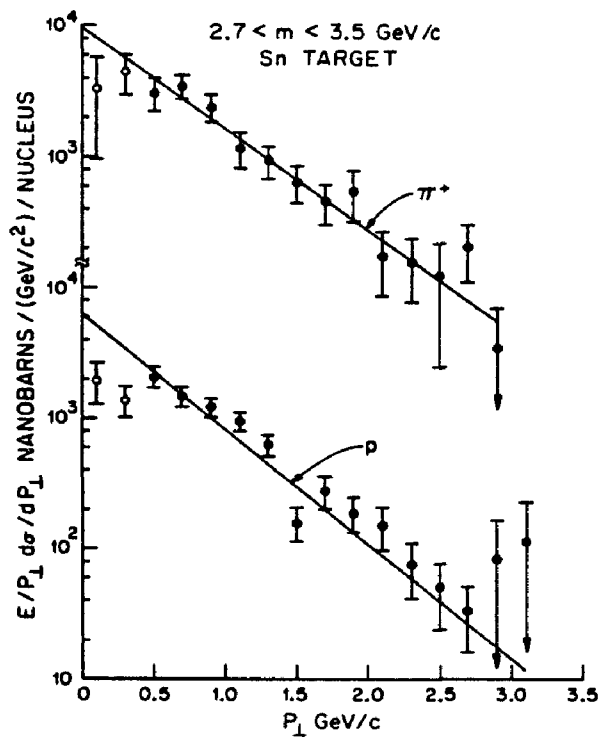


FIGURE 5-30

it represents the data well and because it is generally used by other experimenters and in parton model calculations.

Shown in figures 5-17 through 5-30 are plots of $E \frac{d^2\sigma}{dP_{\perp}^2}$ ($x_F > 0.1$) and fits to the form $Ae^{-BP_{\perp}}$, also for the five interactions and seven mass bins. The form $Ae^{-BP_{\perp}}$, which is commonly used by others, fits the data well in all but the lowest P_{\perp} bins. The two lowest bins were excluded from the fitting so that the parameters obtained would better represent the overall picture. This exclusion made a small difference in the fit parameter B. In the 2.3 to 3.5 GeV/c² mass bin (J), the parameter changed from $1.84 \pm .09$ to $2.05 \pm .09$.

The parameters of the fits to $E \frac{d\sigma}{dx_F}$ and $E \frac{d^2\sigma}{dP_{\perp}^2}$ are given in the following table. The normalization constants from the two fits were combined giving an overall normalization constant A for the form

$$E \frac{d^3\sigma}{dx_F dP_{\perp}^2} = Ae^{-BP_{\perp}} (1 - x_F)^C.$$

Attempts to fit $E \frac{d^3\sigma}{dx_F dP_{\perp}^2}$ failed for masses above 1.5 GeV/c² because of low statistics.

The following tables list the measured value of
E $\frac{d^3\sigma}{dx_p dp_{\perp}^2}$ in the seven mass bins as a function of x_p and
p_⊥.

$\pi^+ + C \rightarrow \pi^+ K^+ X$
 CROSS SECTION (95 < M < 11)

	.025	.075	.125	.175	.225	.275	.325	.375	.425	.475	.525	.575	.625	.675	.725	.775	.825	.875
1	.243E0	.255E1	.271E3	.270E3	.221E3	.115E3	.220E3	.213E3	.110E3	.104E3	.200E3	.500E3	.500E3	.000E0	.000E0	.225E3	.130E3	.000E0
3	.495E0	.710E1	.149E3	.149E3	.137E3	.139E3	.167E3	.174E3	.143E3	.115E3	.149E3	.671E3	.101E3	.000E0	.000E0	.147E2	.000E0	.000E0
5	.133E1	.546E1	.157E3	.137E3	.170E3	.470E2	.470E2	.470E2	.112E3	.104E3	.440E2	.741E2	.754E2	.113E2	.000E0	.211E2	.000E0	.709E1
7	.607E0	.548E1	.434E2	.455E2	.414E2	.601E2	.700E2	.444E2	.570E2	.400E2	.335E2	.304E2	.371E2	.164E2	.000E0	.357E1	.000E0	.000E0
9	.607E0	.425E1	.479E2	.401E2	.271E2	.279E2	.284E2	.270E2	.220E2	.222E2	.270E2	.423E1	.270E2	.561E1	.000E0	.407E1	.000E0	.464E1
1.1	.364E0	.154E1	.127E2	.127E2	.176E2	.145E2	.143E2	.152E2	.152E2	.140E2	.153E2	.101E1	.463E1	.713E1	.000E0	.125E1	.000E0	.178E1
1.3	.000E0	.154E1	.127E2	.127E2	.176E2	.145E2	.143E2	.152E2	.152E2	.140E2	.153E2	.101E1	.463E1	.713E1	.000E0	.125E1	.000E0	.178E1
1.5	.000E0	.445E0	.631E1	.342E1	.403E1	.249E1	.422E1	.140E1	.423E1	.353E1	.555E0	.472E1	.560E0	.425E1	.000E0	.581E0	.000E0	.000E0
1.7	.243E0	.243E0	.114E1	.371E1	.745E0	.129E1	.686E0	.100E0	.100E0	.100E0	.770E0	.164E0	.000E0	.000E0	.000E0	.000E0	.000E0	.000E0
1.9	.000E0	.000E0	.240E1	.000E0	.355E0	.000E0	.384E0	.000E0	.000E0	.000E0	.000E0	.000E0	.000E0	.000E0	.000E0	.000E0	.000E0	.000E0
2.1	.000E0	.121E0	.000E0	.000E0	.000E0	.413E0	.684E0	.000E0	.000E0	.000E0	.000E0	.000E0	.000E0	.000E0	.000E0	.000E0	.000E0	.000E0
2.3	.000E0	.000E0	.000E0	.000E0	.000E0	.000E0	.000E0	.000E0	.000E0	.000E0	.000E0	.000E0	.000E0	.000E0	.000E0	.000E0	.000E0	.000E0
2.5	.000E0	.000E0	.000E0	.000E0	.000E0	.000E0	.000E0	.000E0	.000E0	.000E0	.000E0	.000E0	.000E0	.000E0	.000E0	.000E0	.000E0	.000E0
2.7	.000E0	.000E0	.000E0	.000E0	.000E0	.000E0	.000E0	.000E0	.000E0	.000E0	.000E0	.000E0	.000E0	.000E0	.000E0	.000E0	.000E0	.000E0
2.9	.000E0	.000E0	.000E0	.000E0	.000E0	.000E0	.000E0	.000E0	.000E0	.000E0	.000E0	.000E0	.000E0	.000E0	.000E0	.000E0	.000E0	.000E0
3.1	.000E0	.000E0	.000E0	.000E0	.000E0	.000E0	.000E0	.000E0	.000E0	.000E0	.000E0	.000E0	.000E0	.000E0	.000E0	.000E0	.000E0	.000E0
3.3	.000E0	.000E0	.000E0	.000E0	.000E0	.000E0	.000E0	.000E0	.000E0	.000E0	.000E0	.000E0	.000E0	.000E0	.000E0	.000E0	.000E0	.000E0
3.5	.000E0	.000E0	.000E0	.000E0	.000E0	.000E0	.000E0	.000E0	.000E0	.000E0	.000E0	.000E0	.000E0	.000E0	.000E0	.000E0	.000E0	.000E0
3.7	.000E0	.000E0	.000E0	.000E0	.000E0	.000E0	.000E0	.000E0	.000E0	.000E0	.000E0	.000E0	.000E0	.000E0	.000E0	.000E0	.000E0	.000E0
3.9	.000E0	.000E0	.000E0	.000E0	.000E0	.000E0	.000E0	.000E0	.000E0	.000E0	.000E0	.000E0	.000E0	.000E0	.000E0	.000E0	.000E0	.000E0
1	.695E0	.213E1	.531E2	.474E2	.350E2	.265E2	.414E2	.475E2	.349E2	.770E2	.740E2	.204E3	.603E2	.000E0	.000E0	.165E3	.141E3	.000E0
3	.493E0	.251E1	.233E2	.204E2	.177E2	.180E2	.212E2	.221E2	.244E2	.244E2	.247E2	.267E2	.463E2	.547E2	.000E0	.194E2	.000E0	.000E0
5	.430E0	.202E1	.149E2	.145E2	.136E2	.120E2	.123E2	.133E2	.148E2	.147E2	.224E2	.200E2	.240E2	.413E1	.147E2	.125E2	.000E0	.442E1
7	.444E0	.155E1	.121E2	.994E1	.735E1	.735E1	.747E1	.747E1	.751E1	.751E1	.664E1	.116E2	.157E2	.214E2	.000E0	.360E1	.000E0	.000E0
9	.454E0	.113E1	.472E1	.542E1	.515E1	.401E1	.424E1	.444E1	.557E1	.531E1	.664E1	.414E1	.447E1	.241E1	.854E1	.291E1	.356E0	.446E1
1.1	.476E0	.643E0	.442E1	.487E1	.255E1	.310E1	.330E1	.301E1	.431E1	.284E1	.284E1	.109E1	.400E1	.475E1	.217E1	.126E1	.000E0	.142E1
1.3	.340E0	.634E0	.306E1	.145E1	.219E1	.156E1	.166E1	.154E1	.163E1	.259E1	.145E1	.255E1	.633E0	.760E0	.000E0	.117E1	.000E0	.000E0
1.5	.000E0	.277E0	.241E1	.147E1	.133E1	.105E1	.102E1	.110E1	.114E1	.149E1	.555E0	.254E1	.540E0	.340E1	.611E0	.582E0	.000E0	.000E0
1.7	.185E0	.193E0	.774E0	.140E1	.524E0	.647E0	.447E0	.410E0	.761E0	.450E0	.450E0	.170E1	.000E0	.000E0	.000E0	.000E0	.000E0	.000E0
1.9	.000E0	.000E0	.000E0	.000E0	.350E0	.000E0	.384E0	.000E0	.000E0	.000E0	.000E0	.000E0	.000E0	.000E0	.000E0	.000E0	.000E0	.000E0
2.1	.000E0	.000E0	.000E0	.000E0	.000E0	.000E0	.000E0	.000E0	.000E0	.000E0	.000E0	.000E0	.000E0	.000E0	.000E0	.000E0	.000E0	.000E0
2.3	.000E0	.000E0	.000E0	.000E0	.000E0	.000E0	.000E0	.000E0	.000E0	.000E0	.000E0	.000E0	.000E0	.000E0	.000E0	.000E0	.000E0	.000E0
2.5	.000E0	.000E0	.000E0	.000E0	.000E0	.000E0	.000E0	.000E0	.000E0	.000E0	.000E0	.000E0	.000E0	.000E0	.000E0	.000E0	.000E0	.000E0
2.7	.000E0	.000E0	.000E0	.000E0	.000E0	.000E0	.000E0	.000E0	.000E0	.000E0	.000E0	.000E0	.000E0	.000E0	.000E0	.000E0	.000E0	.000E0
2.9	.000E0	.000E0	.000E0	.000E0	.000E0	.000E0	.000E0	.000E0	.000E0	.000E0	.000E0	.000E0	.000E0	.000E0	.000E0	.000E0	.000E0	.000E0
3.1	.000E0	.000E0	.000E0	.000E0	.000E0	.000E0	.000E0	.000E0	.000E0	.000E0	.000E0	.000E0	.000E0	.000E0	.000E0	.000E0	.000E0	.000E0
3.3	.000E0	.000E0	.000E0	.000E0	.000E0	.000E0	.000E0	.000E0	.000E0	.000E0	.000E0	.000E0	.000E0	.000E0	.000E0	.000E0	.000E0	.000E0
3.5	.000E0	.000E0	.000E0	.000E0	.000E0	.000E0	.000E0	.000E0	.000E0	.000E0	.000E0	.000E0	.000E0	.000E0	.000E0	.000E0	.000E0	.000E0
3.7	.000E0	.000E0	.000E0	.000E0	.000E0	.000E0	.000E0	.000E0	.000E0	.000E0	.000E0	.000E0	.000E0	.000E0	.000E0	.000E0	.000E0	.000E0
3.9	.000E0	.000E0	.000E0	.000E0	.000E0	.000E0	.000E0	.000E0	.000E0	.000E0	.000E0	.000E0	.000E0	.000E0	.000E0	.000E0	.000E0	.000E0

ERRORS (.95 < M < 1.1)

Our results for incident protons are in fair agreement with the measurements of Binkley³⁰ et al. who performed a similar experiment using a broad band neutron beam. Because of the spread in neutron momenta in their beam, their x_F distributions are probably less reliable than ours.

B. General Trends of the Data

In this section, I will discuss the mass dependence of three features of the data. These are the "slope" parameters of the x_F distributions, the average transverse momenta and the dependence of production cross sections on the atomic mass (A) of the target material. For figure 5-31, I have fit the data to the form

$$\int \frac{d\sigma}{dx_F} = A(1 - x_F)^N$$

and plotted N for the usual mass bins. The π^+ and π^- results are the same within errors for all of the mass bins. The proton result differs from that of the pions. It is interesting to note that, for the entire mass range, $N_p = N_\pi + 2$ is correct within statistics even though some of the mass bins are dominated by resonances and other mass bins seem to contain nonresonant μ -pairs.

Figure 5-32 shows the average P_\perp for each mass bin. Unlike the x_F distributions, the value of $\langle P_\perp \rangle$ is independent of incident particle. It increases smoothly with mass, again showing no difference between resonant and

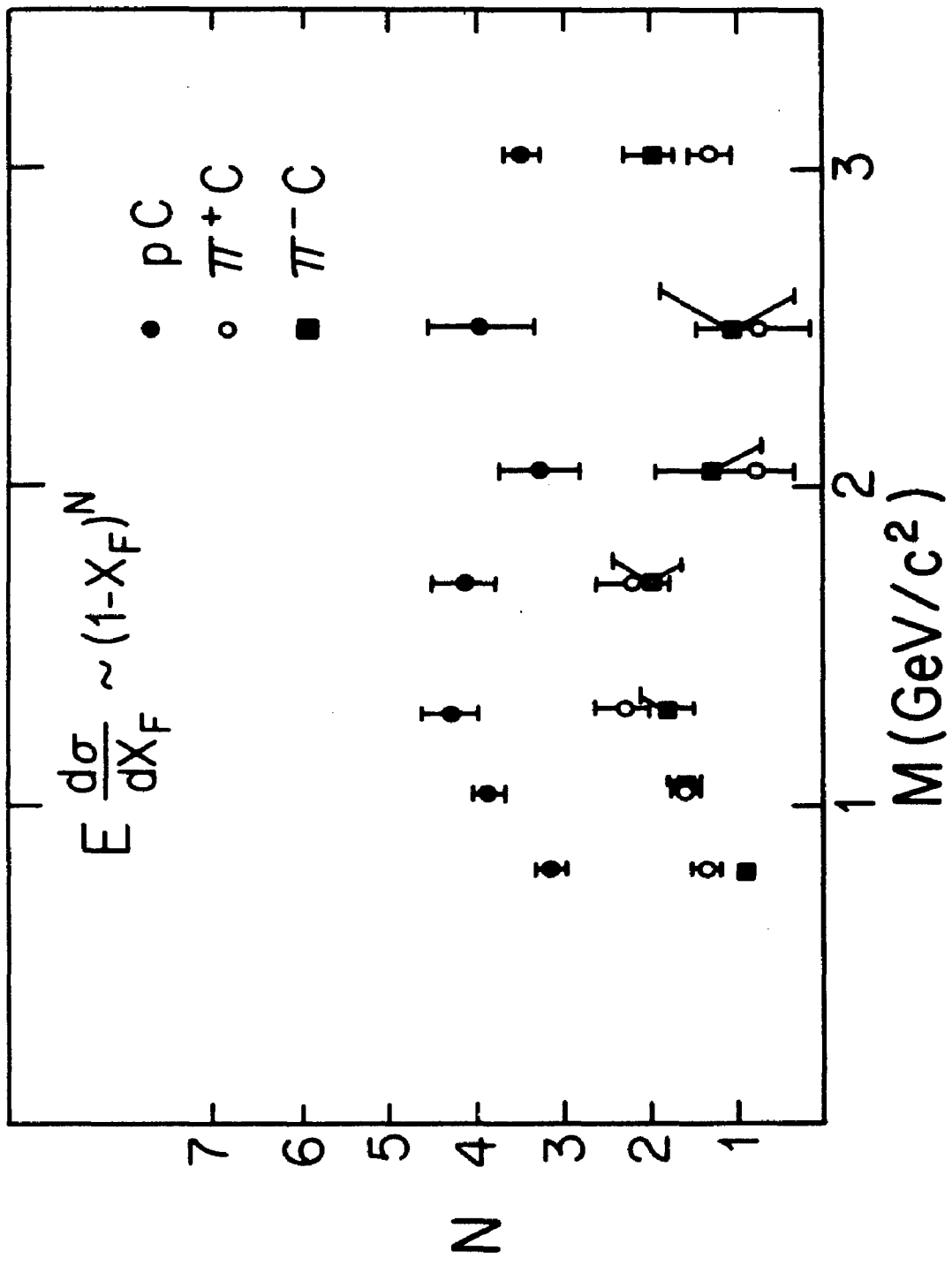


FIGURE 5-31. PLOTS OF X_F DISTRIBUTION "SLOPE" PARAMETER N VERSUS MASS FOR π^+ , π^- AND PROTONS INCIDENT ON CARBON.

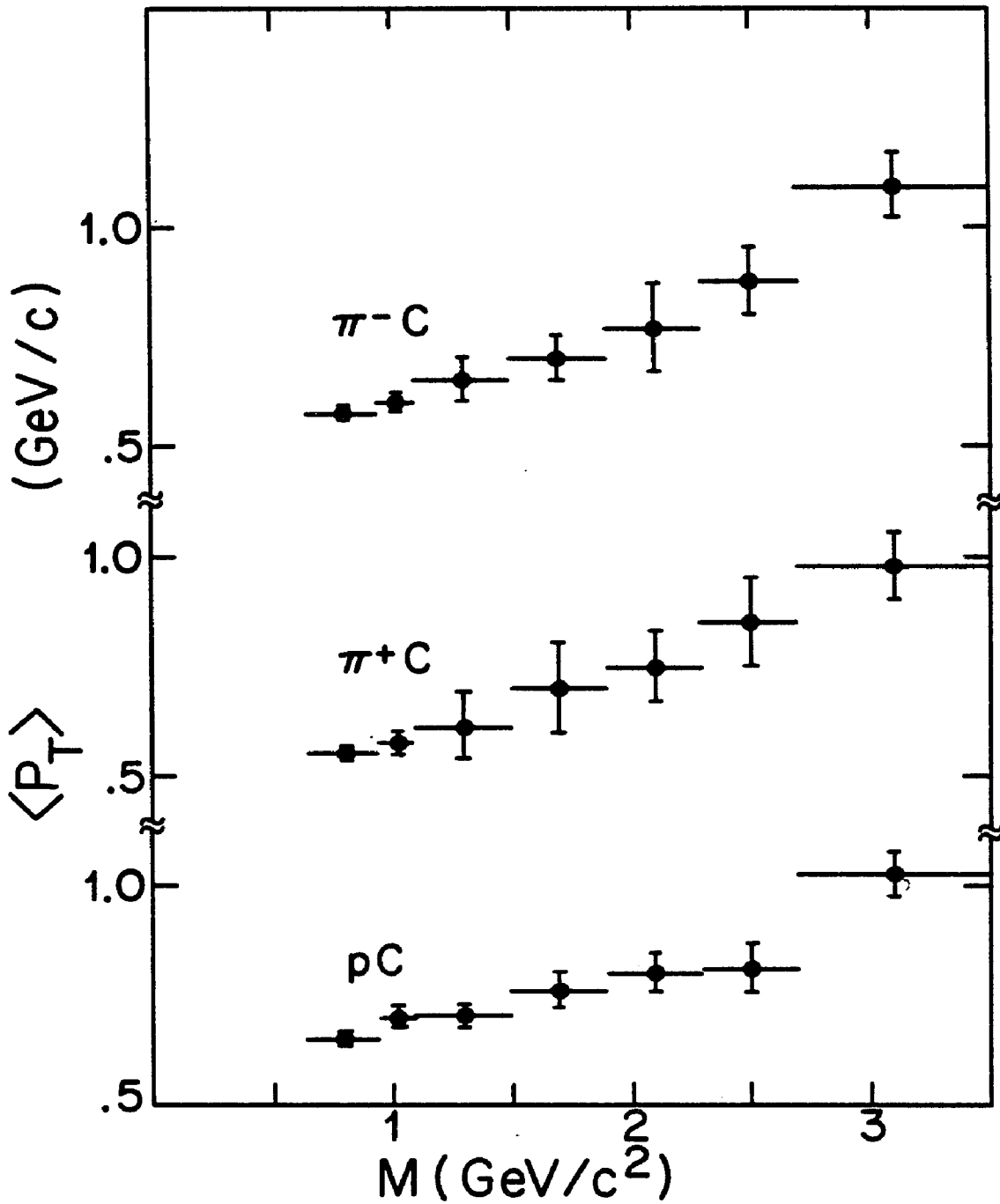


FIGURE 5-32. PLOTS OF $\langle P_T \rangle$ VERSUS MASS FOR π^+ , π^- AND PROTONS INCIDENT ON CARBON.

nonresonant μ -pairs.

We calculated the A dependence of μ -pair production using the cross sections on the carbon and tin targets. These cross sections were assumed to be proportional to A^α and α was calculated as a function of mass. Figure 5-33 shows α for p and π^+ induced events. For both incident particles, α starts at about 2/3 at low mass, increasing smoothly to about 0.9 in the J mass region.

A surprising result here is the smooth variation of N , $\langle P_\perp \rangle$ and α over the mass range $0.65 < m < 3.5 \text{ GeV}/c^2$. Also surprising is the constant ratio of $(1-x_F)^2$ between $E \frac{d\sigma}{dx_F}$ for pion induced reactions and for proton induced reactions even though one might expect μ -pair production mechanisms to differ between mass bins dominated by vector mesons and mass bins dominated by continuum. The data suggest that the mechanisms producing low mass vector mesons, high mass vector mesons and continuum muon pairs are similar in some way.

C. J Production

The x_F distributions $(E \frac{d\sigma}{dx_F})$ for J production are shown in figures 5-15 and 5-16. The P_\perp distributions $(E \frac{d^2\sigma}{dP_\perp^2})$ are shown in figures 5-29 and 5-30. The shapes of these distributions follow the same pattern as in other mass bins. Since no dramatic difference is seen between J production

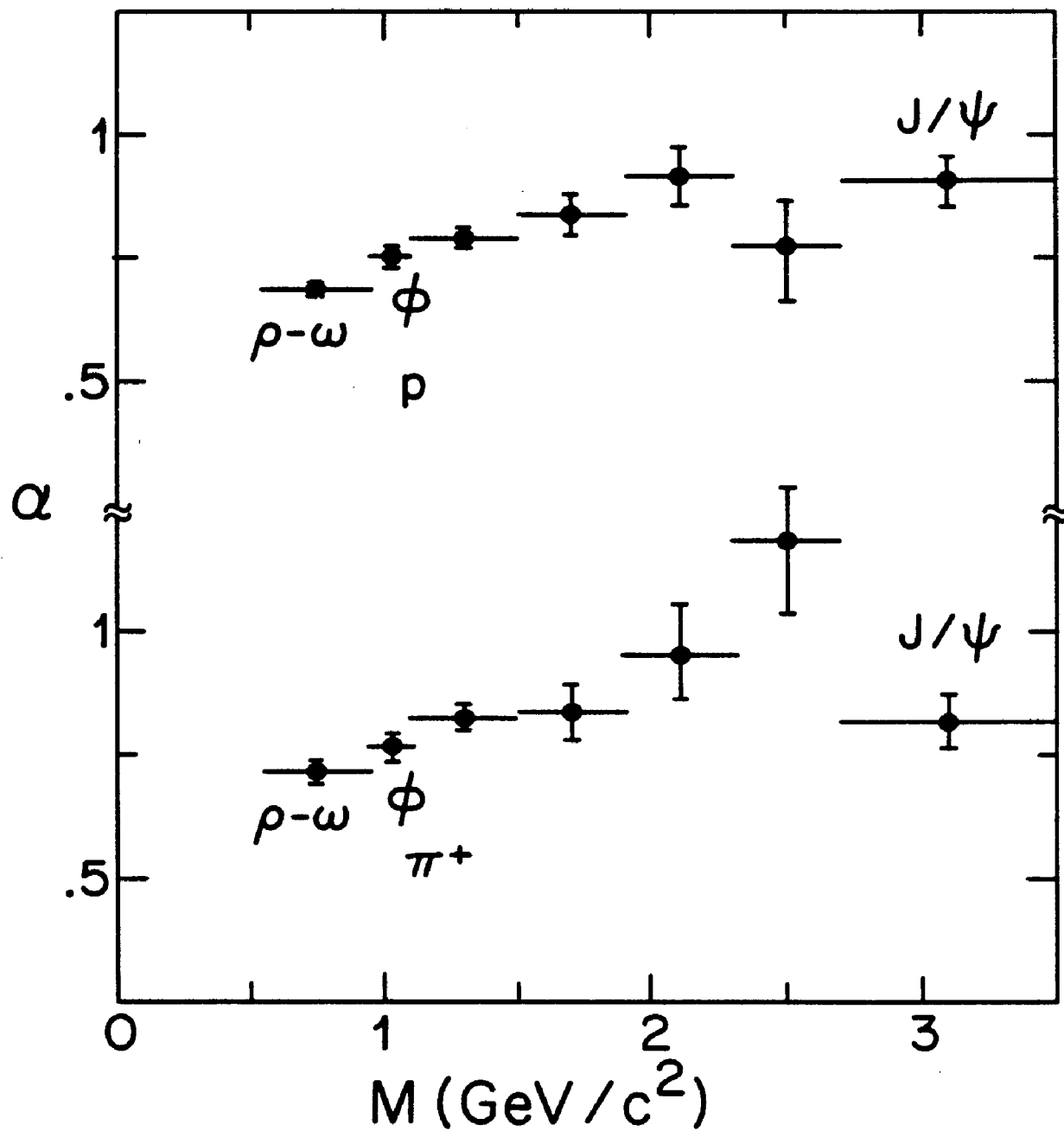


FIGURE 5-33. ATOMIC NUMBER DEPENDENCE OF MUON PAIR PRODUCTION CROSS SECTION VERSUS MASS.

and production of muon pairs in other mass regions (see figures 5-31 and 5-32), the x_F and P_{\perp} distributions are probably not very useful in determining the specific mechanism by which J's are produced. They may, however, be useful in ruling out some production mechanisms that are not similar to those of lower mass muon pairs.

By fitting $\frac{d\sigma}{dx_F}$, the total cross section per nucleus for J production and decay to μ -pairs for $x_F > 0$ was determined to be

<u>Reaction</u>	<u>$B\sigma (x_F > 0)$</u>	<u>Events</u>
$\pi^- + C$	$120 \pm 9 \text{ nb}$	372
$\pi^+ + C$	$104 \pm 12 \text{ nb}$	438
$p + C$	$71 \pm 3 \text{ nb}$	1007

where the errors quoted are statistical only. These values are model independent because of the large acceptance of our detector.

Figure 5-34 shows the first significant measurement of the helicity angle (θ^*) distribution for J decay, along with that for the ρ - ω mass bin. Because statistical power is needed, the plot represents a combination of data from all beam particles and from both targets. The acceptance of the spectrometer is also shown. For the ρ - ω plot, data for x_F

> 0.3 were used, while for the J, $x_F > 0.1$ was required. The raw data were corrected for spectrometer acceptance, which depended on x_F and on $\cos \theta^*$. This was necessary since the acceptance was a strong function of x_F at large values of $\cos \theta^*$. The data were fit to the form $1 + P \cos^2(\theta^*)$. For the ρ - ω , P was found to be 0.02 ± 0.07 , which is in excellent agreement with the expected value for unpolarized production. For the J, P was found to be -0.28 ± 0.22 . This translates to a 35 percent confidence level for $P = 0$, a 0.01 percent confidence level for $P = 1$ and a 0.6 percent confidence level for $P = -1$. The following table presents the fit values of P for pions and protons separately.

<u>BEAM PARTICLE</u>	<u>P</u>	<u>χ^2/DEG. OF FREEDOM</u>
p	-0.34 ± 0.26	0.89
π^\pm	-0.15 ± 0.34	1.49
combined	-0.28 ± 0.22	1.02

Because other experiments measuring J production by protons accept events only near $x_F = 0$ (and because this is the first experiment to accurately measure J production by pions), we must extrapolate our results for proton induced production to $x_F = 0$ in order to make a comparison. The

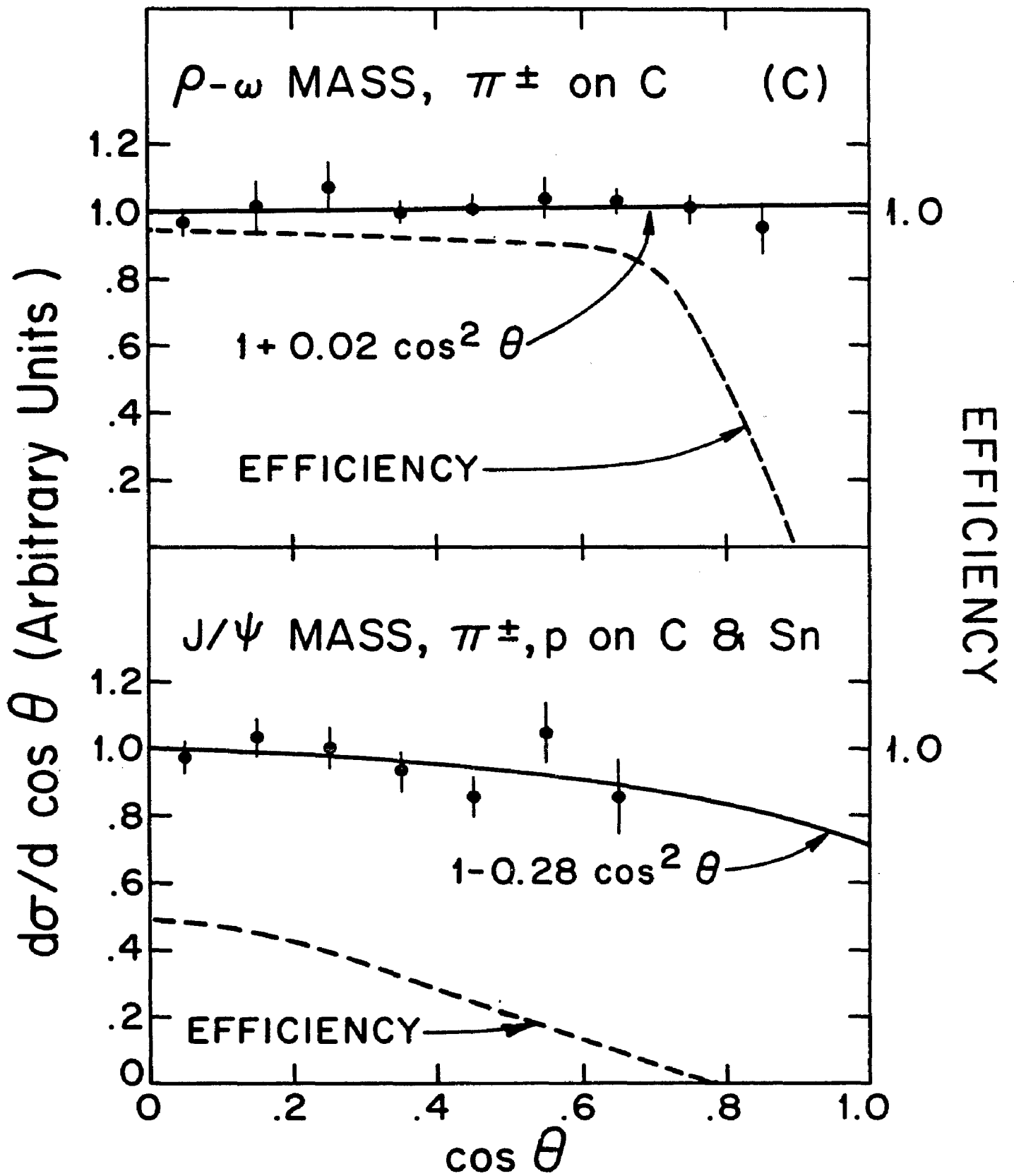


FIGURE 5-34. ANGULAR DISTRIBUTION OF J DECAY TO $\mu^+ \mu^-$ IN THE HELICITY FRAME.

dependence of $\left. \frac{d\sigma}{dx_F} \right|_{x_F=0}$ on \sqrt{s} is shown in figure 5-35. A point from our 150 GeV/c test run³¹ is plotted in the figure. The x_F and P_{\perp} distributions measured in the test run (figure 5-36) are in good agreement with the data reported above. A sharp increase in the cross section is evident up to $\sqrt{s} = 15$ GeV. Above that point, J production increases slowly with energy.

D. Additional Muons in Association with the J

Since some have predicted that the J is produced predominately by OZI allowed mechanisms (see chapter I section A), where a second J or a pair of charmed particles is produced also, it is interesting to look for additional muons in association with the J. A background source of third muons is pion or kaon decay. To calculate this background we used the number of three muon events at low mass. Some cuts were applied to remove other forms of background: 1) The three muon tracks had to be associated with three different hits in the P hodoscope. 2) Muons with momenta greater than 100 GeV/c were not considered. 3) The three muons were required to come from a single vertex in the target (χ^2 cut). These cuts removed only a small fraction of the good events (~5 percent). The following table displays the measured results.

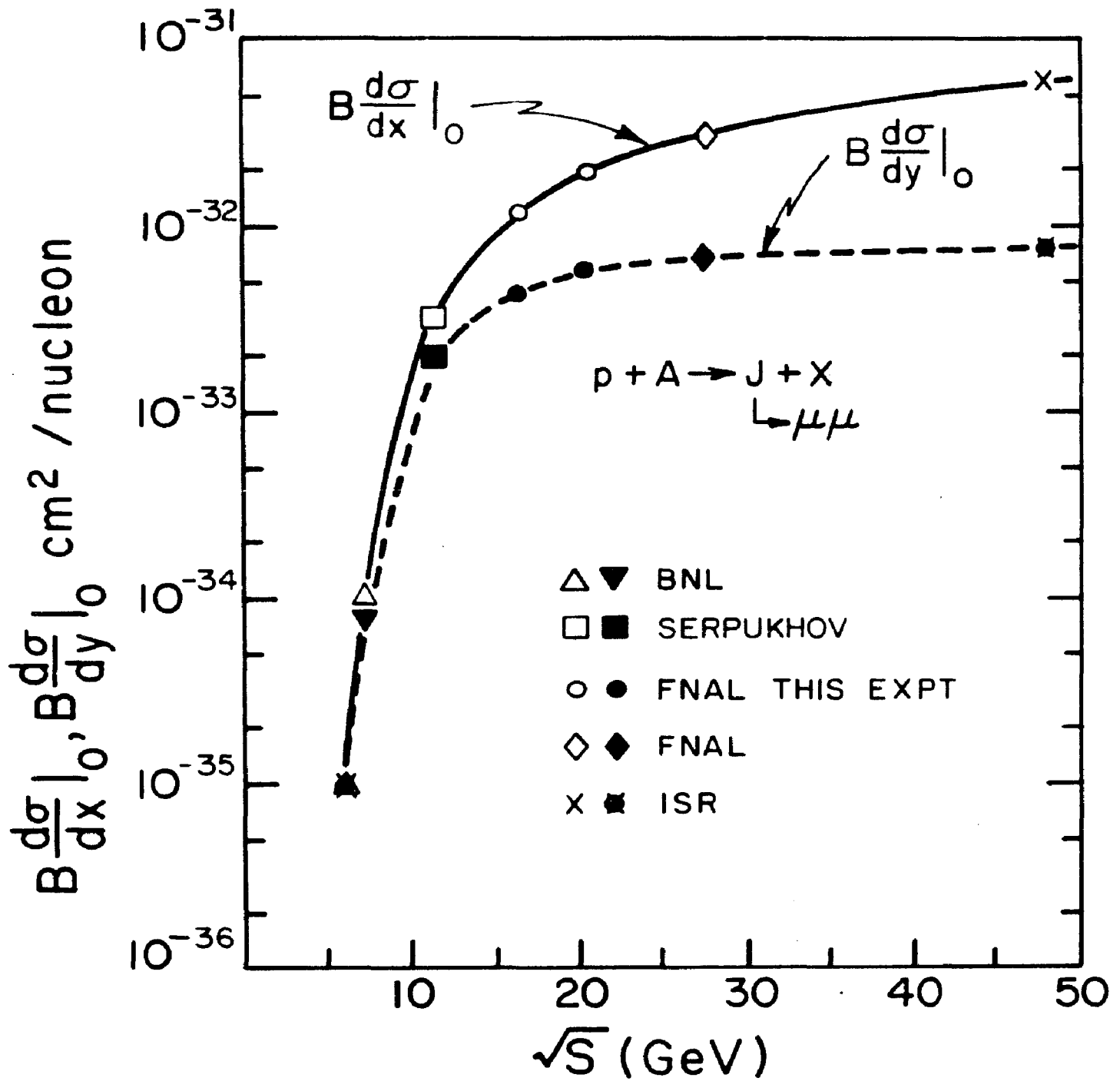


FIGURE 5-35. DEPENDENCE OF J PRODUCTION ON \sqrt{S} .

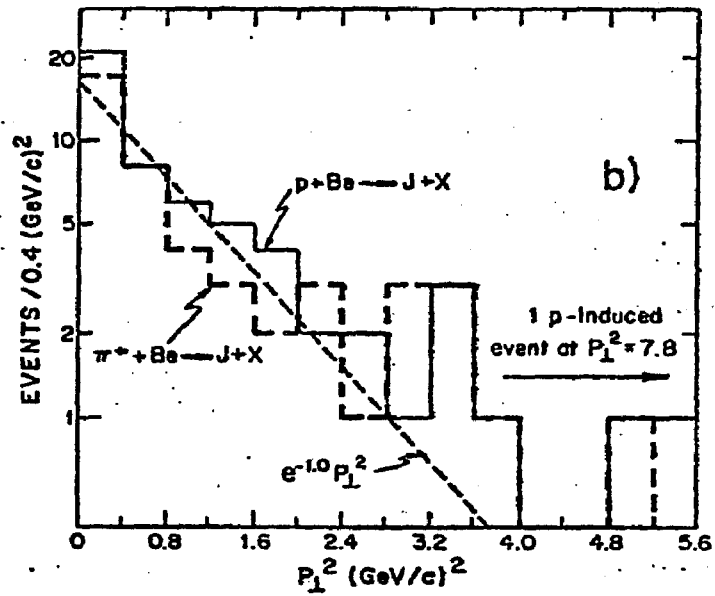
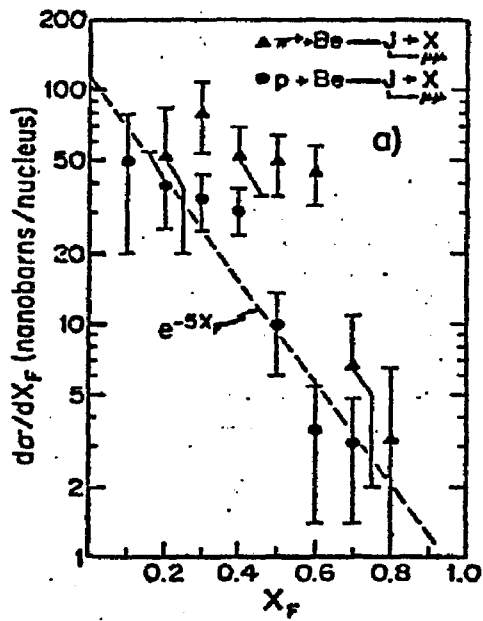


FIGURE 5-36. J PRODUCTION DATA FROM 150 GeV/c TEST RUN. (A) $\frac{d\sigma}{dX_F}$ (B) $\frac{d\sigma}{dP_T^2}$

Range of M_{μ^-} (GeV/c ²)	Beam	Observed data Events				Predictions from π and K decay Events	
		$\mu^+\mu^-$	3μ	4μ	R	3μ	R
0.21-2.3	p	740 000	803	5	1.59 ± 0.12	1053 ± 263	1.60 ± 0.15
	π^+	162 000	419	1	1.63 ± 0.16	300 ± 75	1.75 ± 0.15
	π^-	146 000	278	2	0.91 ± 0.11	320 ± 80	0.80 ± 0.10
2.7-3.5 (J/ψ)	p	1195	2	0	...	1.3	...
	π^+	471	0	0	...	1.2	...
	π^-	434	0	0	...	0.8	...

The data are shown for two mass regions, $0.21 < m < 2.3$ GeV/c² and $2.7 < m < 3.5$ GeV/c². The events from the first mass region are used to test the assumption that the chief source of background is from pion or kaon decay and to calculate this background. The measured number of $\mu^+\mu^-$ events, three-muon events and four-muon events are shown in the first three columns of the table. In the fourth column, the measured ratio (R) of $\mu^+\mu^+\mu^-$ events to $\mu^-\mu^-\mu^+$ events is given. For the low mass bin, columns five and six show the number of three-muon events and the charge ratio R as calculated assuming that all three muon events come from dimuons accompanied by pion or kaon decay. These calculations are in good agreement with the data.

For the high mass bin, column five gives the number of background events expected from meson decay as calculated from the measured number of three muon events in the low mass bin. This small background accounts for all the three muon events observed in the J mass region. There is no evidence that the J is produced in association with charmed

particles or additional J's.

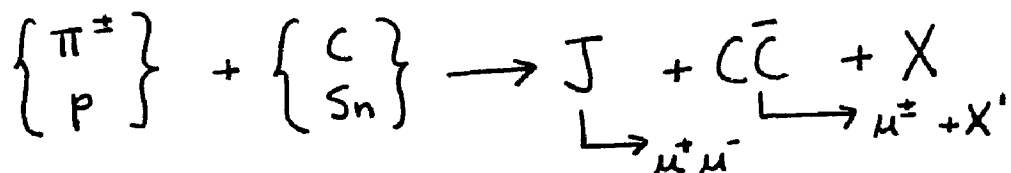
For the reaction



it was assumed that the x_F 's and P_{\perp} 's of the two J's were uncorrelated and that each was produced with the x_F and P_{\perp} distributions measured for production of single J's. Using these assumptions, we obtain the 90 percent confidence level limits shown below.

$\frac{\sigma_{JJ}}{\sigma_J}$	<u>Incident Particle</u>
.072	p
.052	π^+
.079	π^-
.021	combined

To find the fraction of J's produced in association with charmed particles in the reaction below, more complicated assumptions were used.



First, it was assumed that the charmed particle and the J

were produced with correlated rapidities. The distribution of rapidity differences³² used was $e^{-2|y_c - y_T|}$. Second, the charmed particle with mass $1.87 \text{ GeV}/c^2$ was assumed to decay to $\mu \nu X$ where X was either a K meson or a collection of hadrons with mass of one GeV/c^2 . The lower detection efficiency was used. The 90 percent confidence level limits are

$\frac{\sigma_{JCC}}{\sigma_J}$	<u>Incident Particle</u>
.040	p
.028	π^+
.041	π^-
.010	combined

The limits given above are insensitive to the model used due to the large acceptance of the spectrometer. Because of the masses of the particles involved, however, OZI allowed mechanisms may become more important near $x_F = 0$ where we have little data. Similar results to those shown above have been reported by Binkley³³ et al. for incident neutrons.

Our data are in strong disagreement with the the predictions of Siverson and Goldman. They allow two possibilities: either the OZI rule does not apply to J

production or, as suggested by Lipkin³⁴, the OZI violating mechanisms for J production are stronger than the allowed mechanisms despite OZI suppression.

Since the OZI rule is used to explain the width of the J and other new particles, it is important that it be understood. This result puts an additional constraint on any theory explaining OZI suppression.

E. ψ' Production

Figure 5-37 shows $\frac{d\sigma}{dm}$ in the ψ' mass region for proton induced events. The solid curve is a Monte Carlo generated J line shape. The dashed line is a fit to the continuum in the two to four GeV/c^2 mass region which agrees well with our value of $\frac{d\sigma}{dm}$ at $4.7 \text{ GeV}/c^2$. In the $3.7 \text{ GeV}/c^2$ area there is a significant excess above the continuum and high mass tail of the J. After subtracting, we find the following ψ' production cross section for $x_F > 0.1$.

$$\frac{B\sigma(\psi'(3.7))}{B\sigma(J)} = 0.007 \pm 0.004 \text{ (p-C)}$$

$$\frac{B\sigma(\psi'(3.7))}{B\sigma(J)} = 0.018 \pm 0.007 \text{ (\pi}^+ \text{-C)}$$

For the π^- induced data, there is significantly larger continuum, making the subtraction more difficult. We

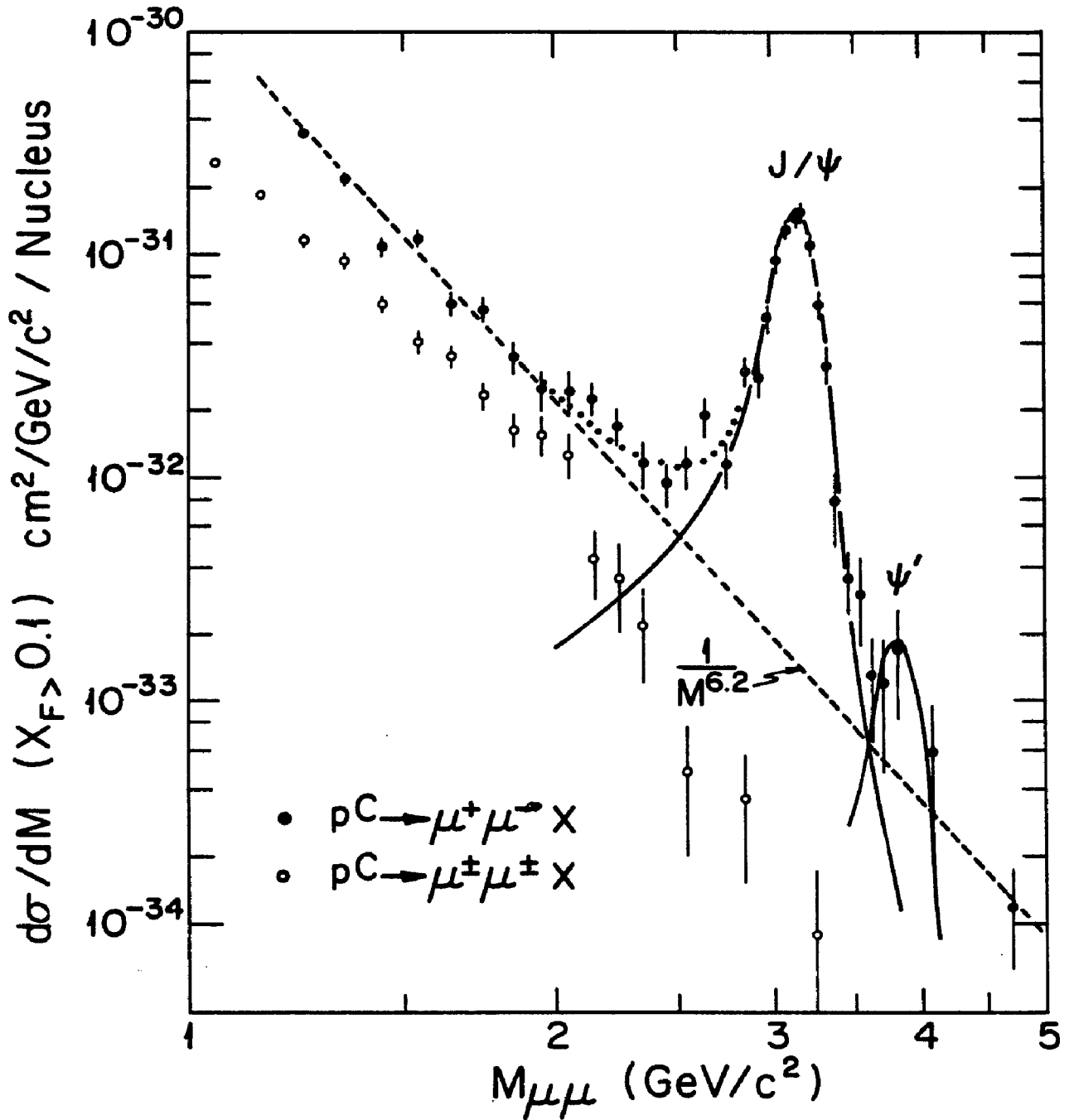


FIGURE 5-37. $\frac{d\sigma}{dm}$ ($x_F > 0.01$) FOR P - C INTERACTIONS. THE SOLID CURVES ARE MONTE CARLO ESTIMATES OF THE LINE SHAPES FOR THE J AND ψ' . THE DASHED CURVE IS A FIT TO THE MUON PAIR CONTINUUM IN THE MASS REGION 2.0 TO 2.7 GeV/c^2 . THE DOTTED CURVE IS THE SUM OF THE OTHER TWO CURVES.

therefore have no result for the π^- beam.

The ψ' is produced much less copiously than the J. Since they have the same quantum numbers, the production mechanism for the two resonances should be similar. One mechanism, discussed in chapter one, that would increase J production relative to ψ' production is the two gluon fusion mechanism which requires $C = +1$ states which decay to the J. There are no known $C = +1$ states which decay to the ψ' . Of course, since the ψ' is a radial excitation of the J, other mechanisms may also be consistent with the lower production cross section. The ψ' cross section is larger than that expected from the Drell-Yan production mechanism by about a factor of 15. This implies that it is produced hadronically.

F. The Drell-Yan Model

Figure 5-1 shows the mass spectra for the three incident particle types on a carbon target along with the range of predictions of the Drell-Yan model for incident protons. This range was determined by using sets of structure functions^{35,36,37} by three different authors. The calculation includes the effect of color, which is to reduce the cross section by a factor of three. The data are well above the model; however, the model is not expected to work well in this mass-range because the conditions allowing use

of the impulse approximation are not satisfied. As stated in chapter I section B, the impulse approximation should be valid for quarks with momenta in the center of mass greater than 1 GeV/c. By using the relations

$$m^2 = x_A x_B s$$

and

$$x_F = x_A - x_E$$

the kinematic region for which the impulse approximation applies can be determined. If we take a 2 GeV/c quark momentum cut off, the model should not begin to apply to our data ($x_F \approx .3$, $s = 450 \text{ GeV}^2$) until we reach the 3 to 4 GeV/c² mass range. In figure 5-1b, our two highest mass data points are plotted along with the points of two other experiments^{38,39}, which are scaled according to the Drell-Yan formula using linear A dependence and our measured x_F distribution. Here the data and calculations are in agreement.

Figure 5-38 shows the ratios of $\frac{d\sigma}{dm}$ ($x_F > 0.15$) for p versus π^+ , p versus π^- and π^+ versus π^- in the usual mass bins. These are compared to the Drell-Yan model calculations. The most interesting of these is the π^+/π^- ratio, which is predicted by the model to be significantly less than one at high masses. In fact, it approaches one-fourth for very large masses. This is due to

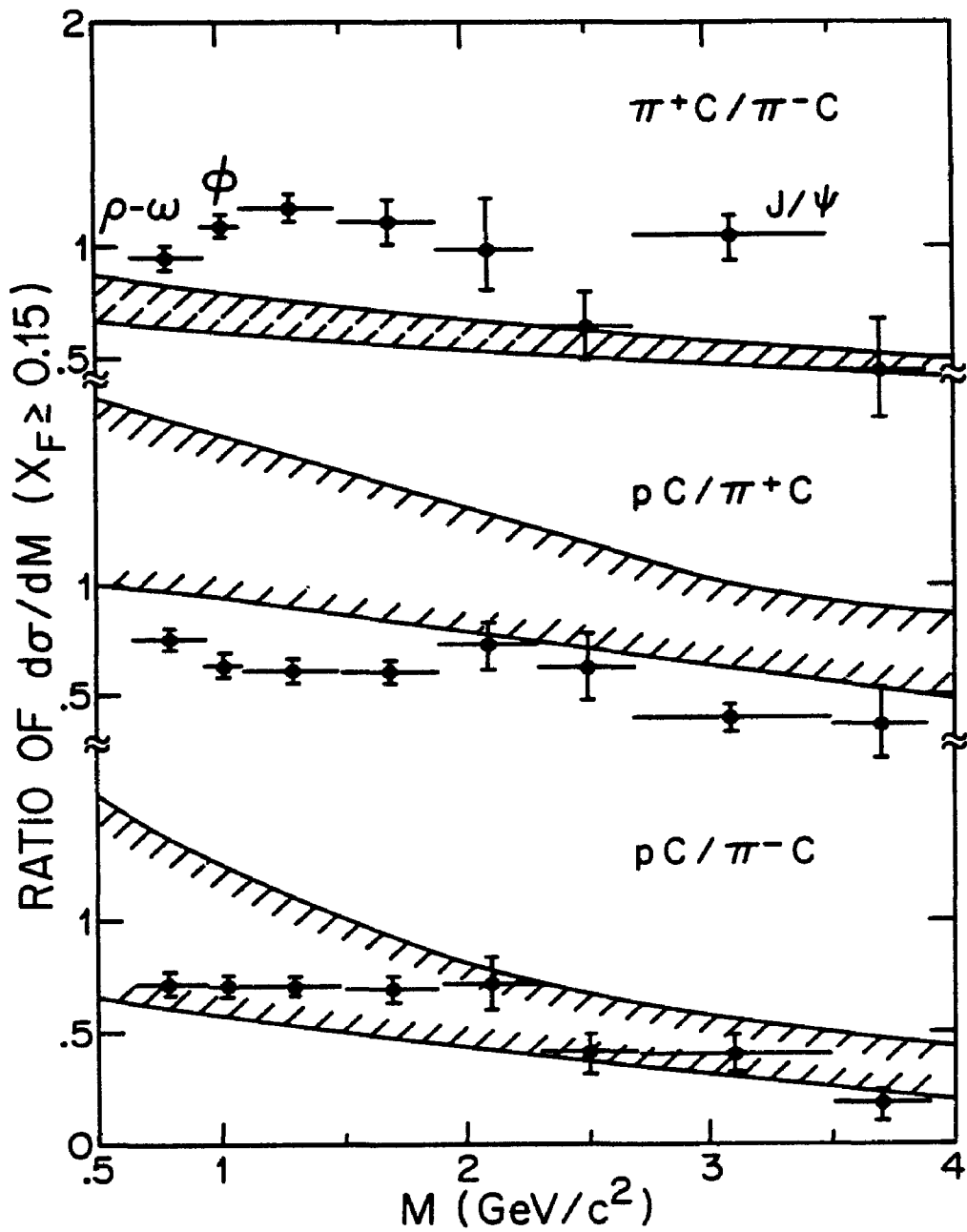


FIGURE 5-38. MASS DEPENDENCE OF RATIOS OF MUON PAIR PRODUCTION CROSS SECTIONS ($x_F > 0.15$) FOR DIFFERING INCIDENT PARTICLES. THE CROSSHATCHED AREAS ARE THE RANGE OF RESULTS FROM DRELL-YAN MODEL CALCULATIONS.

the charges of the valence antiquarks in pions (see chapter I section E). The data show a significant deviation from one in the highest mass nonresonant bins and are in good agreement with the Drell-Yan model. In the bins dominated by the well known resonances ρ, ω, ϕ and J , the ratio is equal to one, within errors, as required for strong production. This evidence supports electromagnetic production at the highest masses.

It is important that the Drell-Yan model be tested further for two reasons. First, the structure of nucleons and mesons can be studied with this model. Second, Drell-Yan particle production is important in design and selection of future accelerators and of experiments at those accelerators. For instance, W^+ and Z^0 production rates at p - p colliding beams machines are best predicted⁴⁰ by the Drell-Yan model.

The two best checks of the model are made by testing its scaling prediction and by measuring the difference between π^+ and π^- induced production of massive lepton pairs as discussed above. Our group expects to make a precise measurement of the π^+ / π^- ratio in the near future at Fermilab.

REFERENCES

1. J. J. Aubert et al., Phys. Rev. Letters 33, 1404 (1974).
2. J. E. Augustin et al., Phys. Rev. Letters 33, 1406 (1974).
3. B. Knapp et al., Phys. Rev. Letters 34, 1040 (1975).
4. B. Knapp et al., Phys. Rev. Letters 34, 1044 (1975).
5. Mary K. Gaillard, Benjamin W. Lee and Jonathan L. Rosner,
FERMILAB-PUB-74/86-THY, August 1974.
6. G. Goldhaber et al., Phys. Rev. Letters 37, 255 (1976).
7. L. Peruzzi et al., Phys. Rev. Letters 37, 570 (1976).
8. B. Knapp et al., Phys. Rev. Letters 37, 882 (1976).
9. Dennis Sivers and Terry Goldman, Rutherford Laboratory
Pub. RL-75-147-T134, September 1975.
10. Dennis Sivers, Phys. Rev. D 11, 3253 (1975).
11. S. Okubo, Phys. Letters 5, 165 (1963).
12. G. Zweig, unpublished report (1964).
13. J. Iizuka, Prog. Theor. Phys. Suppl. 37-38, 21 (1966).
14. C. G. Callan et al., Phys. Rev. Letters 34, 52 (1975).
15. M. B. Einhorn and S. D. Ellis, Phys. Rev. Letters 34,
1190 (1975); Phys. Rev. D 12, 2007 (1975).

16. C. E. Carlson and R. Suaya, William and Mary Pub. WM-PP-10, February (1976).
17. G. S. Abrams et al., Phys. Rev. Letters 33, 1453 (1974).
18. Sidney D. Drell and Tung-Mow Yan, Phys. Rev. Letters 25, 316 (1970).
19. Glynn R. Farrar, Nuclear Physics B 77, 429 (1974).
20. G. Altarelli, N. Cabibo, L. Maiani and R. Petronzio, Nuclear Physics B 92, 413 (1975).
21. John C. Collins and Davison E. Soper, Princeton University Preprint.
22. J. H. Cristenson, G. S. Hicks, L. M. Lederman, P. J. Limon and B. G. Pope, Phys. Rev. D 8, 2016 (1973).
23. B. Aubert et al., FERMILAB-Conf-75/31-EXP, April 1975.
24. K. B. Burns et al., Nucl. Instr. and Meth. 106, 171 (1973).
25. Thomas A. Nunamaker and David B. Turner, Nucl. Instr. and Meth. 113, 445 (1973).
26. Stephen H. Pordes, Harvard University Thesis, February 1976.
27. Dennis Theriot, FERMILAB-TM-229, March 1970.
28. B. Rossi, High Energy Particles, Prentice Hall (1952), p. 61.
29. F. C. Winkelmann et al., Phys. Letters 56B, 101 (1975).

30. M. Binkley et al., Phys. Rev. Letters 37, 571 (1976);
M. Binkley et al., Phys. Rev. Letters 37, 574 (1976).
31. K. J. Anderson et al., Phys. Rev. Letters 60B, 309 (1976).
32. R. M. Barnett and D. Silverman, Phys. Rev. D 12, 2037 (1975).
33. M. Binkley et al., Phys. Rev. Letters 37, 578 (1976).
34. H. J. Lipkin, Phys. Letters 60B, 371 (1976).
35. R. D. Field and R. P. Feynmann, CALTECH Preprint, CALT-68-565.
36. D. C. Hom et al., Phys. Rev. Letters 37, 1374 (1976).
37. L. Kluberg et al., Phys. Rev. Letters 37, 1451 (1976).
38. C. Quigg, Rev. Mod. Phys. 49, 297 (1977).

ACKNOWLEDGEMENTS

The success of the experiment is due to the hard work of each of my collaborators: Kelby J. Anderson, Greg G. Henry, Kirk T. McDonald, James E. Pilcher, Eli I. Rosenberg, Gary H. Sanders, A. J. Stewart Smith and Jon J. Thaler. They were cheerful and willing to perform their share of the menial tasks. Jim Pilcher deserves special mention for proposing and designing the experiment. We received assistance at various stages of the experiment from Gary Hogan, Jim Mueller, Cathy Newman and Rob Pisarski.

I thank the physicists of the Chicago-Harvard-Illinois-Oxford collaboration who built a good deal of the equipment we used. Tony Loomis, Steve Pordes and Andris Skuja were particularly helpful during the early stages of running and data analysis.

The Fermilab neutrino area staff competently assisted us throughout the setup and run of the experiment. Our equipment was mechanically designed by Ken Wright and was constructed by the staff of the Princeton Elementary Particles Laboratory. Most of this construction was performed by Walt Bell, Walt Davidson and Dick Raberman.

I am especially indebted to Mary Woo who shared in the preparation of this thesis. Allan Paul did an excellent job of drafting the figures. In the short time which was available, Pierre Piroue wrote a very useful critique of this document.

My advisor, Stew Smith, directed me throughout the experiment. He had a firm understanding of what jobs needed to be done and

taught me how to do them. He promptly read several drafts of this thesis making numerous helpful suggestions. Because of Stew, my work on the experiment was both enjoyable and very educational.